Title
The components for a quantum computer based on surface state electrons on liquid helium

Author
Naberhuis, Brian Patrick

Publication Date
2007

UNIVERSITY OF CALIFORNIA, SAN DIEGO

The components for a quantum computer based on surface state electrons on liquid helium

A dissertation submitted in partial satisfaction of the
requirements for the degree
Doctor of Philosophy

in

Physics

by

Brian Patrick Naberhuis

Committee in charge:

Professor John Goodkind, Chair
Professor Dimitri Basov
Professor David Meyer
Professor Lu Sham
Professor Edward Yu

2007

The dissertation of Brian Patrick Naberhuis is approved, and it is acceptable in quality and form for publication on microfilm:

Chair

University of California, San Diego

2007

To my grandfathers,
both passed before their time.
One for teaching me how to think,
One for teaching me how to relax,
And both for teaching me how to live.

TABLE OF CONTENTS

LIST OF FIGURES

LIST OF TABLES

ACKNOWLEDGEMENTS

The thing nobody ever tells you before you start graduate school is that a Ph.D. is never the work of a single individual working alone—at the very least, you depend upon the work of the people around you to support your efforts, and upon your adviser for guidance and insight into the subtle problems encountered along the way. But it takes even more than that. It also takes a strong network of friends and family simply to keep a Ph.D. candidate *sane*. In short, I owe thanks to a very large number of people.

I owe a very large debt of gratitude to the three post-docs who worked on this project along side me: Subramanyam Pilla, Oleksander Syschenko, and Xinchang Zhang. Without their patience and instruction, this project would not have even started, let alone gotten as far as it did. Outside of our small research group, I must acknowledge the help of the staff of the UCSD Physics Department Electronics Shop: Allen White, Clem Demmitt, George Kassabian, and Mike Rezin; and the help of the Nano3 staff at CalIT^2: Bernd Fruhberger, Ryan Anderson, Larry Grissom, and Maribel Montero. Without their insight and sense of humor, most of this work would have taken far longer. While I came to UCSD as an experienced machinist, I would like to leave a heart-felt thank you to the memory of Andy Pommer. Every machinist has their own bag of tricks, and I am grateful for Andy's instruction in more advanced machining techniques and his efforts to keep the physics machine shop clean and operational.

As for the keeping sane part, I must thank all of the people at the Ryushinkan Aikido dojo in San Diego. The three-times weekly classes have been the bulk of my exercise for the past six years. I'm especially grateful to Alan Okada and Teresa McGee for their continued support, friendship and mentorship. We've learned a lot from each other over the past few years. Additional thank yous are owed to my game-playing friends, too numerous to name individually. It's nice to have the mental challenge of playing games to offset the challenge and occasional drudgery of experimental physics. I would also like to thank my parents for their continuing love and support. Whenever I had a particularly hard day, I would call them up and talk

to them for a while. It always put me in a better mood.

Beyond that, there are three individuals who deserve more than I can ever repay; two of them have been my teachers for the past six years. Martin Katz is my sensei in Aikido. His classes are half stand-up comedy, half deep and profound philosophy, and one hundred percent a workout. He teaches a sense of compassion and caring for those around us which strikes a resonant chord within me about how life should be led. My other teacher is John Goodkind, a man who truly lives up to his last name. He has patiently guided me along this path, pausing with me when we ran into problems, helping me find solutions to move this work forward. His knowledge of practical physics still astounds me to this day. It is the teachings of these two men which has molded much of my current way of thinking, and I would like to think that we have become good friends over the past few years as well.

Finally, I have to thank my fiancee, Kathryn Smith. We've been together now for the most wonderful year and a half of my life, and I look forward to the years and adventures to come. We've come to where we are along different paths, but we share a common world view and a quiet sense of compassion for our fellow man that's difficult to find in this day and age. You have propped me up and helped me lift the weight of this burden, and I know that we will support each other in a similar fashion as we move into the future. I love you.

VITA

1999	Bachelor of Science, Physics, College of Creative Studies, University of California Santa Barbara
1999	Bachelor of Science, Computer Science, College of Creative Studies, University of California Santa Barbara
1999–2001	Teaching assistant, Department of Physics, University of California San Diego
2001–2007	Research assistant, Department of Physics, University of California San Diego
2006–2007	Laboratory Instructor, Department of Physics, University of California San Diego
2003	Candidate of Philosophy, University of California San Diego
2007	Doctor of Philosophy, University of California San Diego

PUBLICATIONS

K.M.S. Bajaj, J. Liu, B. Naberhuis, and G. Ahlers, "Square Patterns in Rayleigh Bénard Convection with Rotation about a Vertical Axis," *Physical Review Letters*, **81**, 806 (1998).

S. Pilla, B. Naberhuis, and J. Goodkind, "A porous silicon diode as a source of low-energy electrons at milli-Kelvin temperatures," *Journal of Applied Physics*, **98**, 024508 (2005).

S. Pilla, X.C. Zhang, B. Naberhuis, A. Syschenko, and J.M. Goodkind, "High Aspect Ratio Micro-columns to Manipulate Single Electrons on a Liquid Helium Surface for Quantum Logic Bits," *IEEE Transactions on Nanotechnology*, **5**, 568 (2006).

ABSTRACTS

Bajaj, K.M.S., Liu, J., Naberhuis, B., and Ahlers, G., "Square Patterns in Rayleigh-Bénard Convection with Rotation," *1997 American Physical Society: Division of Fluid Dynamics Meeting*

Bajaj, K.M.S., Liu, J., Naberhuis, B. and Ahlers, G., “Rayleigh-Bénard Convection with rotation at small Prandtl numbers,” *1998 March Meeting of the American Physical Society*

Pilla, S., Naberhuis, B., and Goodkind, J.M., “An electron source and a single electron detector for quantum computing,” *2002 March Meeting of the American Physical Society*

Pilla, S., Zhang, X.C., Naberhuis, B., and Goodkind, J.M., “Bolometric Single Electron Detectors and Qubit Structure for Quantum Computing Architecture Based on Electrons on a Dielectric Film,” *2003 March Meeting of the American Physical Society*

Pilla, S., Naberhuis, B., Syschenko, A., Zhang, X.C., and Goodkind, J.M., “Progress on the realization of qubits using electrons on liquid helium,” *2004 March Meeting of the American Physical Society*

Pilla, S., Naberhuis, B., and Goodkind, J.M., “A porous silicon diode as a source of low energy (< 0.1 eV) free electrons and its applications”, *2005 March Meeting of the American Physical Society*

ABSTRACT OF THE DISSERTATION

The components for a quantum computer based on surface state electrons on liquid helium

by

Brian Patrick Naberhuis
Doctor of Philosophy in Physics

University of California San Diego, 2007

Professor John Goodkind, Chair

It has been proposed in literature that a quantum computer can be made utilizing the electronic states of electrons bound to the surface of liquid helium.[47] One can model a single electron on the surface as a 1d hydrogenic atom, providing a set of quantum electronic states which are easily tunable, with an untuned energy gap of 0.488 meV (∼120 GHz) between the ground state and the first excited state, and it is these two energy levels that are proposed as the 0 and 1 state of a qubit. To that end, three microfabricated devices are needed: a low temperature electron source of low energy electrons, a detector capable of detecting single electrons, and a microstructure capable of trapping and Stark shifting the energy levels of individual electrons in proximity close enough to perform multiple qubit operations.

This dissertation contains a description of the devices microfabricated for these purposes. An electron source based on porous silicon was fabricated, tested, and proven to provide low energy electrons. Other more conventional techniques based on a thoriated tungsten filament were also explored. For electron detection, we have fabricated a transition edge superconducting microbolometer. Tests have shown it is capable of detecting a few eV of energy. For the microstructure, we fabricated a series of columns 200 nm in diameter, 1.5 μm in height, separated by 500 nm. For later tests, a microelectrode exposed through a 10 μm diameter hole in a ground plane was used. Initial experiments describing bolometer designs and electron confinement are discussed, as well as proposed microfabrication redesign to continue this work.

Numerical time series computations of both single (NOT, PHASE) and two qubit (SWAP, $\sqrt{\text{SWAP}}$, CNOT) gates are also presented.

Chapter 1

Background and Theory

1.1 Introduction

In 1900, two events occurred that led directly to much of the math and physics that were done during the 20th century. The first was Max Plank's suggestion that the ultraviolet catastrophe could be solved completely by postulating a correspondence between the energy of a wave and its frequency.[46] The second was David Hilbert's list of interesting math problems for the 20th century. On his list, at number 10, was this:

> Given a diophantine equation with any number of unknown quantities and with rational integral numerical coefficients: *to devise a process according to which it can be determined by a finite number of operations whether the equation is solvable in rational integers.*[24][1]

Plank's suggestion led directly to work by Albert Einstein on the photoelectric effect, and eventually to Erwin Schrödinger's work on his wave equation and quantum mechanics in general. Hilbert's question required a formalized view of an algorithm, which was later accomplished by Alonzo Church and Alan Turing.

---

[1] Translated by Dr. Maby Winton Newson and re-published in *Bulletin of the American Mathematical Society* 8 (1902), pp. 437-479.

1.2 Computation

1.2.1 Classical Computation

The original Church-Turing thesis states that any algorithm that can be computed can be done on a Turing Machine, and as a result, simulated on a Universal Turing Machine.[9, 8, 68] The power of the Universal Turing Machine spawned the modern computer industry; in the late 1930s and early 1940s, a number of different machines based on the so-called von Neumann[71] architecture came into existence. The primary question, at first, was what can we compute, given one of these machines.

It rapidly became apparent that while solutions could be posed for many problems, some of those solutions were not calculable for a suitably large problem simply because of the time required to run the algorithm on a computer, or possibly due to excessively large memory requirements. In the 1950s, many researchers were aware of the problem of "brute force" solutions.[64] From their discussions, the field of complexity theory was born, along with the various different hierarchies and complexity classes for computations.

People also began researching different computing paradigms, and a plethora of new algorithmic computation machines came into existence. The digital-based machines were soon shown to be computationally equivalent to Turing Machines. However, two types of machine stood out from the rest as potentially being faster: analog computation and probabilistic computation.

On the surface, it appears that analog computation should provide for a computational machine more powerful than a computer based on a finite alphabet and set of states. After all, real numbers are uncountably infinite and integers are countable — likewise, analog computers have a theoretically uncountably infinite number of states, while digital computers have a countably infinite number of states. In actuality, the noise present in the system limits the behavior of every known analog computer back to the constraints of Turing machine computation classes, and it is well known that an analog machine can be simulated on a Turing machine with a slight overhead.[70]

Probabilistic computing represented a more significant challenge to the supposed efficiency of Turing Machines. Work on these machines exists as far back as the mid 1950s, and there are many useful algorithms to solve problems considered intractable under the classical Turing paradigm.[25] But these algorithms are (as the name implies) implicitly dependent on random number generators, and must be run multiple times to insure statistically accurate results. Even then, the answer is only guaranteed to within some probability distribution.

1.2.2 Thermodynamics and Computation

In the 1930s and 40s, Claude Shannon was concerned about issues of computation and communication, from pointing out that boolean logic was the proper tool for constructing algorithms[56] to research on cryptography during World War 2. Perhaps even more important than the introduction of Boolean logic to computation theory is his work on the mathematical definition of information.[57, 58] In his articles on the subject, Shannon makes the connection between noise in communication channels and Markoff chains, and eventually formulates informational entropy with a mathematical form very similar to Gibb's formulation of entropy.[50] There is quite a debate about if information-theoretic entropy is the same as thermodynamic entropy for deep natural reasons or if it is just a coincidence,[4, 36] but the solutions to many classic thermodynamic problems, such as Maxwell's Demon, depend upon their equivalance.[4].

As early as the 1950s, von Neumann pondered the energetic requirements of computation, and believed that a computer operating at a temperature T must dissipate at least $k_B T \ln 2$ energy per elementary bit operation, as predicted by Shannon's communications theory.[35] Sadly, von Neumann's death prevented him from pursuing this idea. In 1956, Brillouin suggested that the entropy in communication channels increases only when a state is measured, because this was the precise moment when the past became irrelevant in determining the state of the system.[4] Based on this argument, Landauer showed in 1961 that the entropy of a computation increases only when some irreversible step occurs, and that for the von Neumann architecture, this increase is just as von Neumann argued.[32] But Landauer also argued that there was no reason why a fully reversible computation would require any increase in entropy at all.

The idea of a fully reversible computer was first explored by Charles Bennett, first at Argonne National Labs and later on with IBM Research. In 1973, he published work describing a logical process which would not only calculate the desired result, but would also return the system to its original state, thereby not requiring any dissipation of energy.[2] He did not propose a system, though, and worked entirely within the framework of Turing machines.

In 1982, Edward Fredkin and Tomasso Toffoli published a paper proposing that a fully reversible model of computation as being more in-line with modern physics, since much of physics is time-reversible.[20] In this paper, they propose a frictionless billiard ball computer based on a complete set of reversible gates proposed originally by Toffoli.[67]

Later the same year, Richard Feynman suggested that the simple fact that the simulation of many-body quantum mechanics was computationally difficult suggested that our understanding of computation was not complete.[18] This led, in part, to David Deutsch's restatement of the Church-Turing thesis,

> Every finitely realizable physical system can be perfectly simulated by a universal model computing machine operating by finite means.[11]

and his subsequent development of Quantum Turing Machines. He later proposed, along with Richard Jozsa, a problem which was clearly easier to compute on a quantum computer than on a classical one.[12] Work on quantum algorithms has yielded a handful of solutions, most notably: the quantum Fourier Transform[11, 62, 10, 41], the quantum search algorithm[22, 41], and a novel solution for factoring large numbers.[63, 41]

1.3 Problems for Quantum Computation

1.3.1 Quantum versus Classical

Quantum computers (QC) are inherently different beasts than classical computers. In classical computers the only concern about a bit is if it is in the 1 or 0 state. It can be measured as often as one likes, and large amounts of energy ($\sim 1000k_BT$) are spent maintaining the state of a bit during its computational lifetime. Similarly, active memory in classical computers also expend lots of energy remembering the state of the system.

In QCs, we simply don't have the luxury of expending lots of energy maintaining the state of the system. Any attempt to control the state in this way destroys the very quantum information we are interested in exploiting to perform our computation. In QCs, both the energy state and phase of a qubit are important. Energy states can be mixed, and the phase is used in entangled systems to preform the destructive and constructive interference that is used to take advantage of the admixture of states available. From there, it gets harder. In perfect isolation from the outside world, a quantum system will not decohere; its phase rotation and state are predictable from one moment to the next. But such perfect isolation does not exist in nature; experiments always couple to the outside world, and issues of decoherence and state fidelity need to be addressed. Extensive research into error correcting codes has been done for classical communication theory (as communication channels are often noisy),[28] and much of this has been extended and revised to deal with quantum information. Quantum error correcting codes (QECs) provide the finesse solution for QCs to preserve state that classical computers solve by using brute force.[41]

As quantum mechanics is time reversible, QCs are also time reversible, and we have to accept that traditional boolean logic gates cannot be used if we wish to take advantage of quantum mechanics: AND, OR, NAND and such are all irreversible functions; given the output, one cannot tell the input state of the function. The work of Fredkin and Toffolli on reversible computers indicated a suitable set of gates; however, their scheme relied on three-bit gates. In 1995, David DiVincenzo demonstrated using Lie algebra that two-qubit gates could replace all three-qubit gates in the QC case.[13]

1.3.2 Requirements for a Quantum Computer

DiVincenzo outlined the physical requirements for a QC in a paper published in 2000.[14] He listed the physical requirements as:

1. A scalable physical system with well characterized qubits.
2. The ability to initialize the state of the computer (say, all the qubits in the ground state).
3. A decoherence time much longer than the fundamental gate operation time.
4. A "universal" set of gates that can be implemented with a set of qubits.
5. The ability to measure the state of the qubits independently of one another.

Built into this discussion is the assumption that, given these capabilities, QECs can be implemented in a system. With QECs, a calculation can be continued past the decoherence time of the qubits.

1.3.3 Different computing paradigms for Quantum Computing

The paradigm that is most popular for thinking about quantum computers today is the gate model, and with good reason: it is most similar to classical computing, and as such, is easier to think in. However, there are other theoretical models for doing computation with a quantum computer that deserve a mention. Michael Nielsen wrote a novel proposition that does its computing using only a set of non-destructive projective measurements over different combinations of qubits beginning with the entire system in its ground state.[40]. Robert Raussendorf has proposed a system where the computer is first placed in a maximally entangled state, and then the computation is performed by a series of measurements.[49]

1.4 Different quantum computing proposals

Proposals exist for implementing QCs using a variety of systems. A small cross section of these projects include NMR,[31] controlled doping of silicon wafers,[29] excitons in quantum dots,[5, 26] ion traps,[48] and a variety of Josephson Junction circuits.[38, 1, 66]

To date, quantum logic gates have been demonstrated in each of the above systems, except for the controlled doping in silicon wafers system, with varying degrees of fidelity. The highest fidelity systems on record are NMR ($\sim$ 99%)[7] and ion trap systems ($\sim$ 97%).[34]

Execution of quantum algorithms has been reported on two quantum systems. Ion trap QCs have demonstrated the Deutsche-Jozsa algorithm,[23] and NMR has demonstrated Shor's factoring algorithm by factoring the number 15.[69]

Unfortunately, the NMR program on QC has probably run its course: as more qubits are added to the molecules used as computers, the signal to noise ratio decreases exponentially.[41] Ion trap computation efforts are having trouble dealing with increasingly complicated electrode geometries,[72] required because of difficulties in maintaining motional states for large numbers of ions,[41] necessitating arrays of ion traps and the corresponding QECs and inter-array operations to perform more meaningful computations.[42]

1.5 Electrons on Helium

Superfluid helium has three properties that make it suitable for potentially making a quantum computer using electrons bound to its surface: 1. the work function to force an electron into the bulk liquid state is about three orders of magnitude larger than the binding energy due to the polarization field, 2. the dielectric constant of helium is small, and 3. the liquid-vapor interface is smooth, and the saturated vapor pressure decreases exponentially with temperature. This particular combination of properties also gives electrons on liquid helium a very high mobility — the highest measured for 2d electron systems,[61] and makes the system a good choice for studying

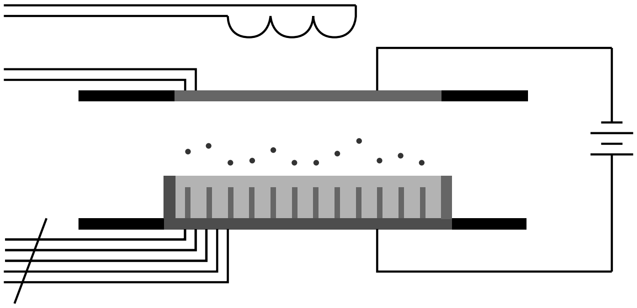

Figure 1.1: A schematic of a computer based on electrons on helium. The electrons are localized over electrodes, which can also be used to Stark shift them. The detector above the system is a microwire bolometer. The electron source is behind the detector, and has access to the sample area via a hole in the detector wafer. The sample is inside a waveguide so microwave radiation can be applied. A magnet surrounds the sample so the T_c of the detector can be controlled. The level of helium above the electrodes is controlled by a wall grown around the posts, making use of the characteristics of superfluid helium films.

1-d tunneling.[54]

Interest in this system as a model for quantum computing is more recent. Platzman and Dykman[47] suggested that electrons could be trapped over electrodes beneath a layer of liquid helium, and that these electrodes could be used to Stark shift the electrons into and out of resonance with respect to both an applied microwave field and each other. Individual operations on qubits are accomplished using the microwave field, and binary operations are accomplished using the coulomb interaction between different electrons. A simple schematic of the system as used for quantum computation is in Figure 1.1.

1.5.1 One electron

There are three primary parts of the one electron Hamiltonian for quantum computation: $H^{(0)}$, which describes the dielectric response of the helium and the subsequent energy levels of the bound electron states; $H^{(C)}$, which describes the interaction of a single electron with a nanoelectrode under the surface of the liquid helium; and $H^{(MW)}$, which describes the interaction of a single electron with a microwave field.

$\mathbf{H}^{(0)}$

A single electron floating above a liquid helium surface is bound to the surface by a combination of the attraction to the polarization field of the helium and the repulsion of the electron from the bulk of the liquid helium. In fact, since the binding energy is four orders of magnitude smaller than the repulsion, we can consider the repulsion to be effectively infinite, so our potential becomes:

$$V_D(z) = \begin{cases} \infty & z \leq 0 \\ -\dfrac{\Lambda}{4\pi\epsilon_0}\dfrac{e^2}{z} & z > 0 \end{cases} \tag{1.1}$$

where $\Lambda \equiv (\epsilon - 1)/4(\epsilon + 1) = 0.00693$, and $\epsilon = 1.057$ is the dielectric constant of helium.

Due to the smoothness of the film, and the very small vapor pressure at low temperatures, the $x - y$ plane is isotropic, which allows for a separable Hamiltonian:

$$H^{(0)} = -\frac{\hbar^2}{2m_e}\nabla^2 + V_D(z) \tag{1.2}$$

which separates into

$$H_z^{(0)} = -\frac{\hbar^2}{2m_e}\partial_z^2 + V_D(z) \tag{1.3}$$

in the direction normal to the surface of the helium, and

$$H_r^{(0)} = -\frac{\hbar^2}{2m_e}\left(\partial_r^2 + \frac{1}{r}\partial_r\right) \tag{1.4}$$

in the plane of the surface of the helium. If we consider equation (1.3) only, we find the solutions normal to the surface are similar to the radial solutions of the hydrogen atom:

$$E_n^{(0)} = \frac{R}{n^2} \tag{1.5}$$

are the energy levels, and

$$\begin{aligned}
\left|\Psi_1^{(0)}(z)\right\rangle &= \frac{2}{\sqrt{a_0}}\left(\frac{z}{a_0}\right)e^{-z/a_0} \\
\left|\Psi_2^{(0)}(z)\right\rangle &= \frac{1}{\sqrt{2a_0}}\left[\left(\frac{z}{a_0}\right)-\frac{1}{2}\left(\frac{z}{a_0}\right)^2\right]e^{-z/2a_0} \\
\left|\Psi_3^{(0)}(z)\right\rangle &= \frac{2}{3\sqrt{3a_0}}\left[\left(\frac{z}{a_0}\right)-\frac{2}{3}\left(\frac{z}{a_0}\right)^2+\frac{2}{27}\left(\frac{z}{a_0}\right)^3\right]e^{-z/3a_0} \\
\left|\Psi_4^{(0)}(z)\right\rangle &= \frac{1}{4\sqrt{a_0}}\left[\left(\frac{z}{a_0}\right)-\frac{3}{4}\left(\frac{z}{a_0}\right)^2+\frac{1}{8}\left(\frac{z}{a_0}\right)^3-\frac{1}{192}\left(\frac{z}{a_0}\right)^4\right]e^{-z/4a_0}
\end{aligned}$$

are the first few eigenfunctions, where the Rydberg energy is defined as

$$R \equiv -\frac{\hbar^2}{2m_e a_0^2} = -0.651\,\text{meV} \tag{1.6}$$

and a_0 is the effective Bohr radius of our 1d hydrogen atom:

$$a_0 \equiv \frac{4\pi\epsilon_0\hbar^2}{\Lambda m_e e^2} = 7.62\,\text{nm} \tag{1.7}$$

The important parameter for quantum computing to take from here is the energy level splitting between the ground state and the first excited state:

$$E_2^{(0)} - E_1^{(0)} = 0.488\,\text{meV} = 118\,\text{GHz} \tag{1.8}$$

There is a derivation of the wave functions for $H_z^{(0)}$ in Appendix A. The ground state and first excited state are shown, along with the potential, in Figure 1.2. It should be noted that the above is an idealization of the system, and ignores ambiguities in defining the density of the superfluid film of helium close to the surface.[39] But this ideal model differs from data fits by only a few percent,[54] and is good enough for our purposes.

$\mathbf{H}^{(C)}$

The primary control mechanism that we use in this system is the voltage on our gate electrode. Changing this voltage yields an electric field at the helium surface that has both normal and in plane components.

$$\mathbf{E}_{\text{App}}(\mathbf{r}, z) = E_z(\mathbf{r}, z)\hat{\mathbf{z}} + E_r(\mathbf{r}, z)\hat{\mathbf{r}} \tag{1.9}$$

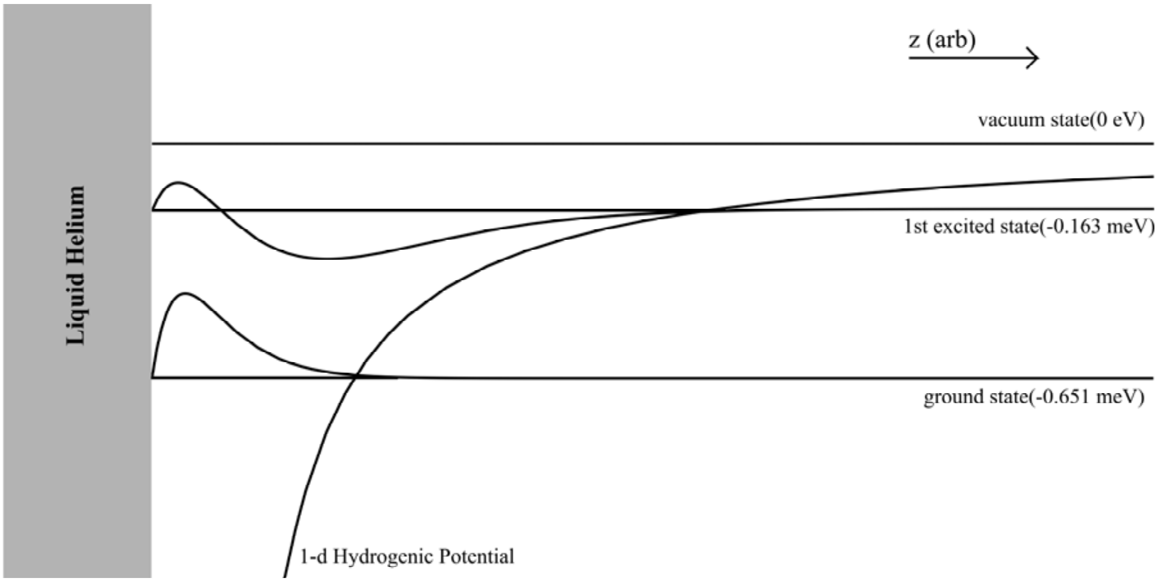

Figure 1.2: Base potential for Electrons on Helium system. The ground state and the first excited state are shown.

The variation in $\mathbf{E}_{\text{App}}$ as a function of z is small over $\langle\Psi_2| z |\Psi_2\rangle - \langle\Psi_1| z |\Psi_1\rangle = 4.5a_0 = 34.3$ nm at the surface of the helium film, about half a micron away from the electrode.

The total effect of this electric field is two-fold: 1. it breaks the translation symmetry of the electron in the plane of the helium, and binds the electron to orbit around the post, and 2. it provides a way to control what the energy level splitting between the electron's ground state and first excited state, due to the Stark effect.

The Hamiltonian for this "control" field is:

$$H^{(C)} = -eE_z(t)z \tag{1.10}$$

Treating this as a perturbative Hamiltonian yields both a correction to the energy levels,

$$\begin{aligned} \left\langle \Psi_1^{(0)} \middle| H^{(C)} \middle| \Psi_1^{(0)} \right\rangle &= -z_{11}eE_z(t) \\ \left\langle \Psi_2^{(0)} \middle| H^{(C)} \middle| \Psi_2^{(0)} \right\rangle &= -z_{22}eE_z(t) \end{aligned}$$

where $z_{ij} = \langle\Psi_i^{(0)}|\, z\, |\Psi_j^{(0)}\rangle$, and corrected wave functions:

$$\begin{aligned}
\left|\Psi_1^{(C)}\right\rangle &= \left|\Psi_1^{(0)}\right\rangle + \frac{eE_z(t)z_{21}^{(0)}}{E_2^{(0)} - E_1^{(0)}}\left|\Psi_2^{(0)}\right\rangle + \frac{eE_z(t)z_{31}^{(0)}}{E_3^{(0)} - E_1^{(0)}}\left|\Psi_3^{(0)}\right\rangle + \cdots \\
&= \left|\Psi_1^{(0)}\right\rangle + 8.72 \times 10^{-6} E_z(t)\left|\Psi_2^{(0)}\right\rangle + 3.21 \times 10^{-6} E_z(t)\left|\Psi_3^{(0)}\right\rangle + \cdots \\
\left|\Psi_2^{(C)}\right\rangle &= \left|\Psi_2^{(0)}\right\rangle + \frac{eE_z(t)z_{12}^{(0)}}{E_1^{(0)} - E_2^{(0)}}\left|\Psi_1^{(0)}\right\rangle + \frac{eE_z(t)z_{32}^{(0)}}{E_3^{(0)} - E_2^{(0)}}\left|\Psi_3^{(0)}\right\rangle + \cdots \\
&= \left|\Psi_2^{(0)}\right\rangle - 8.72 \times 10^{-6} E_z(t)\left|\Psi_1^{(0)}\right\rangle + 1.56 \times 10^{-4} E_z(t)\left|\Psi_3^{(0)}\right\rangle + \cdots .
\end{aligned}$$

We can avoid the problems of having a time dependant term in the wave function by treating $E_z(t)$ as a slowly-varying constant.

$\mathbf{H}^{(MW)}$

In order to move the electrons from the ground state to the first excited state, we apply a microwave field,

$$E_z^{(MW)}(z) = -eE_{MW}\sin(\Omega t) \tag{1.11}$$

The net effect of this microwave field is that it will cause the state of an electron to oscillate between the ground state and the first excited state if $\hbar\Omega = E_2^{(C)} - E_1^{(C)}$, with an oscillation frequency of

$$W_{12} = \frac{eE_{MW}}{\hbar}\left\langle\Psi_1^{(C)}\right| z \left|\Psi_2^{(C)}\right\rangle \tag{1.12}$$

on the resonance, with a bandwidth that is determined by the decay modes of the electron excited state, and the bandwidth of the microwave field.

$\mathbf{H}^{(ip)}$

Fortunately, the in-plane Hamiltonian is still separable from the perpendicular Hamiltonian, and we can approximate this in-plane Hamiltonian as a harmonic oscillator[15]:

$$U_r(r) = \frac{1}{2}m\omega_{\parallel}^2 r^2. \tag{1.13}$$

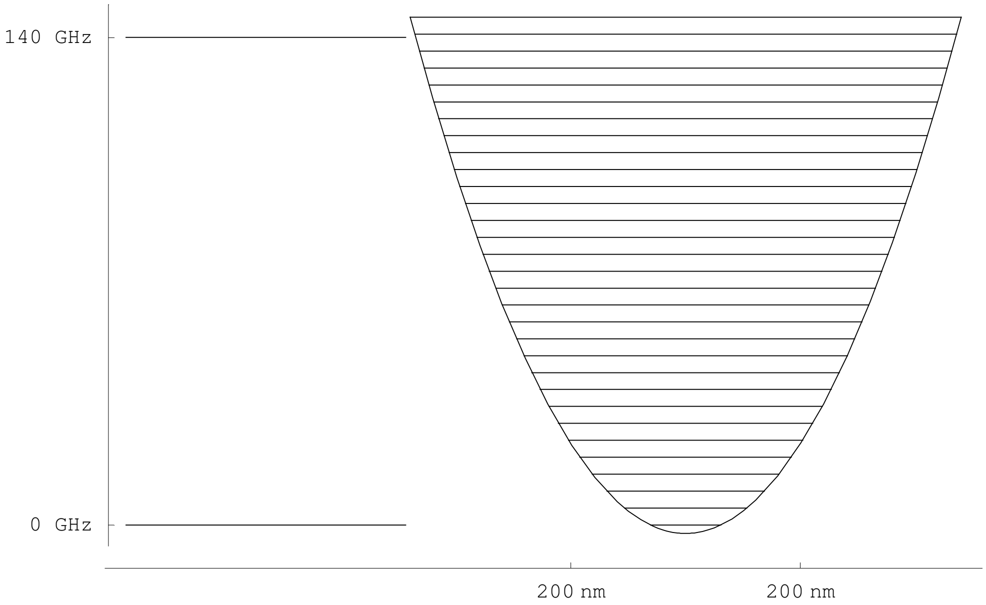

Figure 1.3: Harmonic Oscillator energy levels versus hydrogenic potential energy levels for the simple post model. In this diagram, the radius of the post is 100 nm, and the film is taken to be 500 nm thick above the post. The applied potential on the post is 400 μV . The frequency of the harmonic oscillator for these values is $\sim 40\,\mu$eV (about 460 mK). The left side of the plot shows the associated level splitting of the $|0\rangle$ and $|1\rangle$ states.

The details for finding $\omega_{\|}$ depend on the style of electrode being used. A more thorough discussion can be found in the electrode details discussed in Chapter 3. For the post electrodes, the form of $\omega_{\|}$ is:

$$\omega_{\|}^2 = \frac{e^2}{2\pi\epsilon_0 m_e}\frac{a}{\left(z^2 - a^2\right)^2} + \frac{Vea}{m_e z^3} \tag{1.14}$$

where a is the radius of the post, z is the distance from the post, and V is the applied voltage on the post. An example of the radial potential and energy level splittings versus the hydrogenic energy levels is presented in Figure 1.3.

As long as the energy level splitting of the perpendicular wave functions is incommensurate with the in-plane energy level splittings, there should be no direct interactions between these two states, although there are phonon and ripplon mediated decay modes which could put the system into the radially excited modes.[15]

The end result is that our wave functions pick up two new quantum numbers associated with the harmonic oscillator potential: one describing the total energy stored in the harmonic oscillator, and one describing the degeneracy of the state due to cylindrical symmetry.

1.5.2 Multiple Electrons

Since we are using single electrons for our qubits, we need a mechanism that allows them to communicate with each other which is controllable.

Coulomb Interaction

Since our qubits are inherently charged objects – electrons – our interaction is the Coulomb Interaction:

$$H^{(CI)} = \frac{e^2}{4\pi\epsilon_0}\frac{1}{\sqrt{d_{12}^2 + (z_1 - z_2)^2}} \tag{1.15}$$

where d_{12} is the inter-qubit spacing and z_1 and z_2 are $z^{(C)}$ for the two different qubits, respectively.

For any microfabricated array of electrodes, the inter electron spacing is going to be large compared to the distance between the electrons and the helium film. Thus, we can approximate this Hamiltonian to

$$H^{(CI)} = -\frac{e^2}{8\pi\epsilon_0}\frac{|z_1 - z_2|^2}{d_{12}^3} \tag{1.16}$$

1.5.3 Decay and Dephasing Mechanisms[2]

The decay mechanisms for this particular quantum computing system can be roughly divided into two different categories: surface displacements of the liquid helium due to phonons and ripplons, and electronic interactions between the electrons on the surface and the bulk helium or electrodes. In either case, the decay modes we have to worry about are not usually just excited state to ground state for the vertical electronic eigenstates, but a mixed decay state where some of the energy in

---

[2] This section is based almost entirely upon Reference [15], except where otherwise noted.

the vertical state is left in one of the radial modes. In general, the quantum number of the closest eigenstate can be written as

$$\nu_c \equiv \left\lfloor \frac{E_2^{(C)} - E_1^{(C)}}{\hbar\omega_\parallel} \right\rfloor . \tag{1.17}$$

For calculating decay parameters, we apply Fermi's Golden Rule to the Hamiltonian using the wave functions of both the interacting quasi-particle excitations (as necessary) and the electrons on the surface (including the radial and angular modes). Dephasing parameters are calculated by noting that the surface modulations affect the ground and excited electronic modes differently, as the displacement of the surface is less noticeable in the excited state. This is analogous to energy level broadening in solids due to Raman scattering. In specificity, we can derive an expression for the dephasing rate by considering the thermal average of the difference in energy levels of the qubit computation states, where the thermal average is taken over the appropriate excitation mode. In effect, we can write

$$\Gamma_\phi \simeq \delta\varphi_{21}^2 \tag{1.18}$$

where

$$\delta\varphi_{21}^2 = \frac{1}{\hbar^2} \int_0^t dt_1 \int_0^t dt_2 \left\langle \delta\hat{E}_{12}(t_1) \delta\hat{E}_{12}(t_2) \right\rangle \tag{1.19}$$

and $\delta\hat{E}_{12}(t) = \langle 2;0,0|\, H_i(t)\, |2;0,0\rangle - \langle 1;0,0|\, H_i(t)\, |1;0,0\rangle$ is the expected "noise" on the energy states and $\langle f(t) \rangle$ denotes a thermal average over the appropriate quasi-particle excitation. For the purposes of this discussion, we simplify the notation for the eigenstates of a qubit from $|\Psi_n^{(C)}\rangle\, |\nu, m_\nu\rangle$ to $|n; \nu, m_\nu\rangle$. Because the thermal average of the energy fluctuations should be constant in time, we can further simplify Γ_ϕ:

$$\Gamma_\phi \simeq \frac{1}{\hbar^2} \int_0^\infty dt \left\langle \delta\hat{E}_{12}(t) \delta\hat{E}_{12}(0) \right\rangle . \tag{1.20}$$

The decay and dephasing parameters below are calculated for $\omega_\parallel / 2\pi = 20\,\mathrm{GHz}$, which is a reasonable in-plane harmonic oscillator frequency if we consider the additional confinement due to either nearby electrons or due to additional electrodes used solely to enhance the in-plane confinement. It is assumed that the dominant dephasing mechanisms are due to electrode coupling or ripplons, and other dephasing mechanisms are not calculated.

Surface displacements

Before we can discuss the effects of surface displacements on the electrons, we need a good model describing the way the surface shape and electrons interact. It is easiest to change our coordinates of interest from $(\mathbf{r}, z)$ to $(\mathbf{r}, z-\xi(\mathbf{r}))$, and then write our perturbation Hamiltonian in orders of $\xi(\mathbf{r})$. [60]

We can also write our Hamiltonian in terms of a Fourier series $\xi_(\mathbf{r}) = \sum_{\mathbf{q}} e^{i\mathbf{q}\cdot\mathbf{r}}\xi_{\mathbf{q}}$, so to first and second order, it looks like

$$H_{sd}^{(1)} = \sum_{\mathbf{q}} \xi_{\mathbf{q}} e^{i\mathbf{q}\cdot\mathbf{r}} \hat{V}_{\mathbf{q}} \tag{1.21}$$

and

$$H_{sd}^{(2)} = \sum_{\mathbf{q_1},\mathbf{q_2}} \xi_{\mathbf{q_1}}\xi_{\mathbf{q_2}} e^{i(\mathbf{q_1}+\mathbf{q_2})\cdot\mathbf{r}} \hat{V}_{\mathbf{q_1}\mathbf{q_2}}. \tag{1.22}$$

For $\hat{V}_{\mathbf{q}}$, we need terms that describe the direct kinematic coupling between the electrons and the surface displacements (due to the fact that the wave functions are defined to be 0 at the helium surface), the change in the electric field coupling due to the change in coordinate system, and the change in the polarization energy due to the surface curvature.[15, 53]

$$\hat{V}_{\mathbf{q}} = \frac{1}{2m}\left|\hbar\mathbf{q} + \hat{\mathbf{p}}_{\mathbf{r}}\right|^2 \partial_z + eE_\perp + \hat{V}_{\mathbf{q}}^{(pol)} \tag{1.23}$$

where $\hat{\mathbf{p}}_{\mathbf{r}} = -i\hbar\partial_{\mathbf{r}}$ is the radial momentum operator on the electron and

$$\hat{V}_{\mathbf{q}}^{(pol)} = \frac{\Lambda}{z^2}\left[1 - qzK_1(qz)\right] \tag{1.24}$$

describes the change in the polarization energy due to surface curvature.[3]

$\hat{V}_{\mathbf{q_1}\mathbf{q_2}}$ requires a kinematic term that does not reduce to the one dimensional case, and an additional term in the surface curvature term:

$$\hat{V}_{\mathbf{q_1}\mathbf{q_2}} = \frac{\mathbf{q_1}\cdot\mathbf{q_2}\hbar^2}{2m}\partial_z^2 + \hat{V}_{\mathbf{q_1}\mathbf{q_2}}^{(pol)}, \tag{1.25}$$

where

$$\hat{V}_{\mathbf{q_1}\mathbf{q_2}}^{(pol)} = -\frac{\Lambda}{z^3}\left[1 - \frac{q_1^2 z^2}{2}K_2(q_1 z) - \frac{q_2^2 z^2}{2}K_2(q_2 z) + \frac{\left|\mathbf{q_1}+\mathbf{q_2}\right|^2 z^2}{2}K_2(\left|\mathbf{q_1}+\mathbf{q_2}\right| z)\right] \tag{1.26}$$

---

[3] $K_n(x)$ are the modified Bessel functions of the second kind.

Ripplons

The surface modulation due to a single ripplon can be written as

$$\xi_{\mathbf{q}} = \sqrt{\frac{\hbar q}{2\rho\omega_q S}}(b_{\mathbf{q}} + b^{\dagger}_{-\mathbf{q}}), \tag{1.27}$$

where S is the surface area of the system, ρ is the density of the liquid helium, $\omega_q = (\sigma q^3/\rho)^{1/2}$ is the ripplon frequency, and $b_{\mathbf{q}}$ and its complex conjugate are the creation / annihilation operators for ripplons with wave number $\mathbf{q}$.

As for the cutoff wave number, Monarkha and Shikin suggest that it should be taken at $qa_0 \leq 1$,[39] while Dykman, Platzman, and Seddighrad suggest that the limiting distance should be the thickness of the helium liquid/vapor interface.[15] Both are on the order of a few angstroms, indicating a cutoff of $q_{max} \simeq 10^{-9}\, m^{-1}$.

1 Ripplon

The matrix elements for this decay mode can be written as

$$\langle 0|_r \langle 2; 0, 0|_e \, \xi_{\mathbf{q}} e^{i\mathbf{q}\cdot\mathbf{r}} \hat{V}_{\mathbf{q}} \, |1; \nu_c, m_{\nu_c}\rangle_e \, |{-\mathbf{q}}\rangle_r \, . \tag{1.28}$$

This requires the evaluation of the integral $\langle 0, 0|_e \, e^{i\mathbf{q}\cdot\mathbf{r}} \, |\nu_c, m_{\nu_c}\rangle_e$, which is exponentially small if

$$|\mathbf{q}| \gg \sqrt{\frac{2m\nu_c\omega_\parallel}{\hbar}}. \tag{1.29}$$

This statement is equivalent to the conservation of momentum and energy in the ripplon absorption/emission modes, and requires the ripplon to have enough momentum to force the system into the ν_c excited state. Combining this with our definition of ν_c, equation (1.17), we find that if

$$\omega_\parallel \simeq \omega_{\mathbf{q}} \gg \sqrt{\frac{\sigma}{\rho}} \left[2m \frac{E_2^{(C)} - E_1^{(C)}}{\hbar^2} \right]^{3/4}, \tag{1.30}$$

then this decay mode is exponentially disallowed. The inequality is already met for the post electrodes as presented above using the image charge of the electron inside the post with 0 applied voltage, let alone for larger confinements.

2 Ripplons

Two ripplon decay is different from the one ripplon case, because if the system simultaneously emits a pair of ripplons with opposite momentum states, the exponentially small integral from the 1 ripplon case is no longer small. Again, we are only interested in the decay from $|2;0,0\rangle_{\mathrm{e}}$ to $|1;\nu_c,m_{\nu_c}\rangle_{\mathrm{e}}$, as it is the largest amplitude decay term.

This time, we are interested in calculating the matrix elements

$$\langle\xi_{\mathbf{q_1}}\xi_{\mathbf{q_2}}\rangle \left\langle 2\right|_{e_z} \hat{V}_{\mathbf{q_1 q_2}} \left|1\right\rangle_{e_z} \left\langle 0,0\right|_{e_r} e^{i(\mathbf{q_1}+\mathbf{q_2})\cdot\mathbf{r}} \left|\nu_c,m_{\nu_c}\right\rangle_{e_r}. \tag{1.31}$$

The kinematic portion of the decay can be calculated as

$$\Gamma_{2r}^{(K)} = \frac{K_{12}^2 R^2 m_e \omega_\| q_{\mathrm{res}}^{7/2}}{24\pi\hbar\rho^{1/2}\sigma^{3/2}}, \quad K_{12} = \frac{\langle 1|\, p_z^2/2m_e \,|0\rangle}{R}, \tag{1.32}$$

with $q_{\mathrm{res}} = \delta E/2\hbar$, where $\delta E = E_2 - E_1 - \nu_c\hbar\omega_\|$. If we take $\delta E = \hbar\omega_\|/4$, $q_{res} \simeq 4.6\times 10^8\,\mathrm{m}^{-1}$, then $\Gamma_{2r}^{(K)} = 7.6\times10^2 - 3.8\times10^3\,\mathrm{s}^{-1}$ for a pressing field $E_\perp = 0 - 30000\,\mathrm{V/m}$.

The polarization portion of the decay can be calculated as

$$\Gamma_{2r}^{(\mathrm{pol})} = \frac{U_{12}^2 R^2 m_e \omega_\|}{24\pi\hbar\rho^{1/2}\sigma^{1/2}a_0^4 q_{res}^{1/2}} \tag{1.33}$$

with

$$U_{12} = 2a_0^3 \langle 1|\, z^{-3}\left[2 - q_{\mathrm{res}}^2 z^2 K_2(q_{\mathrm{res}}z)\right] |0\rangle\,. \tag{1.34}$$

Numerical values for $\Gamma_{2r}^{(\mathrm{pol})}$ are roughly an order of magnitude smaller than values for $\Gamma_{2r}^{(K)}$ for similar values for δE. This coefficient does not grow as quickly for increasing values of δE.

Aside from the $\Gamma_{2r}^{(K)}$ and $\Gamma_{2r}^{(\mathrm{pol})}$, there is a term due to the interference between the kinematic and polarization terms. This term is much smaller than either $\Gamma_{2r}^{(K)}$ or $\Gamma_{2r}^{(\mathrm{pol})}$, and will not be discussed.

Scattering of ripplons as a dephasing mechanism is easier to understand in the 2 ripplon picture: a ripplon is absorbed and then re-emitted. The Hamiltonian we need to consider for this two ripplon scattering can be written as

$$H_i^{(2r)} = \sum_{j=1,2}\sum_{\mathbf{q},\mathbf{q}'} v_{\mathbf{q}\mathbf{q}'j} b_{\mathbf{q}}^\dagger b_{\mathbf{q}'} \left|j;0,0\right\rangle \left\langle j;0,0\right| \tag{1.35}$$

For this coupling, the dephasing rate takes the form

$$\Gamma_\phi = \frac{\pi}{\hbar^2} \sum_{\mathbf{q}\mathbf{q}'} \left| v^2_{\mathbf{q}\mathbf{q}'2} - v^2_{\mathbf{q}\mathbf{q}'1} \right| \bar{n}(\omega_q) \left[\bar{n}(\omega_{\mathbf{q}'}) + 1 \right] \delta(\omega_{\mathbf{q}} - \omega_{\mathbf{q}'}), \tag{1.36}$$

where $\bar{n}(\omega) = [\exp(\hbar\omega/k_B T) - 1]^{-1}$ is the expected thermal population of the ripplon modes,

$$\begin{aligned} v_{\mathbf{q}\mathbf{q}'j} \simeq & \frac{\hbar}{S\rho} \sqrt{\frac{qq'}{\omega_q \omega_{q'}}} [\, \langle j;0,0 | \, \hat{V}_{-\mathbf{q}\mathbf{q}'} \, | j;0,0 \rangle \, e^{-(\mathbf{q}-\mathbf{q}')^2 \hbar/4m_e\omega_\parallel} \\ & - \sum_{\nu>0,m_\nu} \left(\mathcal{V}^{j\nu m_\nu}_{\mathbf{q}\mathbf{q}'} + \mathcal{V}^{j\nu m_\nu}_{-\mathbf{q}'-\mathbf{q}} \right) (\hbar\nu\omega_\parallel)^{-1}] \end{aligned} \tag{1.37}$$

are the coupling constants, and

$$\mathcal{V}^{j\nu m_\nu}_{\mathbf{q}\mathbf{q}'} = \langle j;0,0 | \, \hat{V}_{-q} e^{-i\mathbf{q}\mathbf{r}} \, | j;\nu,m_\nu \rangle \, \langle j;\nu,m_\nu | \, \hat{V}_{q'} e^{i\mathbf{q}'\mathbf{r}} \, | j;0,0 \rangle \tag{1.38}$$

are the second order effects due to the first order ripplon couplings.

The delta function in Γ_ϕ requires $q = q'$, so the integrals need to be calculated in terms of the angle between $\mathbf{q}$ and $\mathbf{q}'$. If we assume the ripplons are all thermal, then the majority of the scattering represented in the second order kinematic term, and that portion of the integral can be calculated by the method of steepest descent to obtain

$$\Gamma^{(2K)}_\phi = \frac{\rho}{27} \sqrt{\frac{\pi m_e \omega_\parallel}{2\hbar}} \left(\frac{k_B T}{\hbar\sigma} \right)^3 R^2 \tilde{K}^2_{12} \tag{1.39}$$

where $\tilde{K}_{12} = (\langle 2 | \, p_z^2/2m_e \, | 2 \rangle - \langle 1 | \, p_z^2/2m_e \, | 1 \rangle)/R$. As $E_\perp$ increases, $\tilde{K}_{12}$ decreases. For $T = 10\,\mathrm{mK}$, and $E_\perp = 0$, we find $\Gamma^{(2K)}_\phi = 0.7 \times 10^2\,\mathrm{s}^{-1}$. In addition, by noting that the wave vectors of thermal ripplons $q_T = (\rho/\sigma)^{1/3} (k_B T/\hbar)^{2/3} < 1/a_0$, we can expand the two ripplon polarization term in terms of $q_T a_0$. To lowest order in that expansion, the two ripplon polarization term is the same as $\Gamma^{(2K)}_\phi$, except that $\tilde{K}_{12}$ is replaced by $\tilde{U}_{12} = (\langle 2 | \, \Lambda/2z \, | 2 \rangle - \langle 1 | \, \Lambda/2z \, | 1 \rangle)/R$. Numerically, they are of comperable order to the kinematic couplings.

The last term to calculate is the expected dephasing due to the first order ripplon couplings. The first thing to note is that the kinematic terms drop out of $v_{\mathbf{q}\mathbf{q}'j}$ because there are no terms diagonal in $|2\rangle$, $|1\rangle$. As a result, the major contribution comes from the polarization term. Since the polarization does not couple to the position of the qubit, the sum over ν, m_ν can be directly calculated, and if we assume thermal ripplons, the integral comes out to

$$\Gamma_\phi^{(\mathrm{pol})} \sim \rho\sqrt{\frac{m_e\omega_\parallel}{\hbar}}\left(\frac{k_BT}{\hbar\sigma}\right)^2 R^2k_{12}^2 \tag{1.40}$$

For similar conditions to those above, $\Gamma_\phi^{(\mathrm{pol})} \sim 10^2\,\mathrm{s}^{-1}$.

The net result is that the dephasing rate due to ripplons varies as T^3, and at 10 mK, the dephasing rate is on the order of $10^2\,\mathrm{s}^{-1}$.

Surface modulation by phonons

Bulk-mode phonons lead to a decay mode due to surface modulation similar to that of ripplons. The primary differences between this mode and the ripplon modes are 1. phonons have three dimensional wave vectors, and 2. they have a different dispersion law. For the component of the wave vector $\mathbf{Q}$ normal to the surface, Q_z, it would be unreasonable to consider short wavelength phonons for the same reasons as to why short wavelength ripplons are unreasonable. Therefore, we will consider only $Q_z \ll 10^9\,\mathrm{m}^{-1}$.

The displacement of helium due to phonons is

$$u_{\mathbf{Q}} = \sqrt{\frac{\hbar}{2\rho V v_s Q}}(c_{\mathbf{Q}} - c_{-\mathbf{Q}}^\dagger), \tag{1.41}$$

where V is the volume of the liquid helium, and $c_{\mathbf{Q}}$ and $c_{\mathbf{Q}}^\dagger$ are the typical creation and annihilation operators for phonons. For phonons travelling primarily in the direction normal to the surface, we can write the decay rate as:

$$\Gamma_{\mathrm{ph}}^{(s)} = \frac{1}{8\pi^2\rho v_s\delta E}\sum_{m_\nu=0}^{\nu_c}\int d\mathbf{q}\left|\langle 2;0,0|\, e^{i\mathbf{qr}}\hat{V}_{\mathbf{q}}\,|1;\nu_c,m_\nu\rangle\right|^2, \tag{1.42}$$

where $\mathbf{q}$ is the wave number along the surface.

The decay due to kinematic coupling to the phonons calculates to

$$\Gamma_{\mathrm{ph}}^{(\mathrm{s;k})} = (E_2^{(C)} - E_1^{(C)})^2 z_{12}^2 \frac{\nu_c^2 m_e^3\omega_\parallel^3}{4\pi\rho v_w\hbar^3\delta E}. \tag{1.43}$$

For $\omega_\parallel/2\pi = 21.1\,\mathrm{GHz}$, $\delta E \simeq \hbar\omega_\parallel$ and $E_\perp = 0$, the numerical value of $\Gamma_{\mathrm{ph}}^{(\mathrm{s;k})} = 7.8\times10^2\,\mathrm{s}^{-1}$ ($\nu_c = 5$ in this case). The value goes up to $1.5\times10^4\,\mathrm{s}^{-1}$ for $E_\perp = 30\,\mathrm{kV/m}$, as the value of ν_c rises to 12. This is probably an overestimate since the liquid-vapor boundary is not infinitely sharp, as assumed here.

The contribution to the decay due to the polarization terms is

$$\Gamma_{\mathrm{ph}}^{(\mathrm{s;pol})} = \frac{4R^2 a_0^2 m_e^3 \omega_\parallel^3}{\nu_c! \pi \rho v_s \delta E \hbar^3} \int_0^\infty dx e^{-x} x^{\nu_c+2} v^2(x), \tag{1.44}$$

where

$$v^2(x) = \left| \langle 1| \frac{m_e \omega_\parallel}{2x\hbar z^2} \left[1 - z\sqrt{\frac{2x\hbar}{m_e\omega_\parallel}} K_1 \left(z\sqrt{\frac{2x\hbar}{m_e\omega_\parallel}} \right) \right] |2\rangle \right|^2 .$$

The integral term must be calculated numerically. The numerical value of $\Gamma_{\mathrm{ph}}^{(\mathrm{s;pol})}$ ranges from $\sim 7 \times 10^2\,\mathrm{s}^{-1}$ to $\sim 7 \times 10^3\ \mathrm{s}^{-1}$ for $E_\perp = 0$ to $300\,\mathrm{kV/m}$, using the same parameters as for calculating $\Gamma_{\mathrm{ph}}^{(\mathrm{s;k})}$. There is also a term due to interference effects between the polarization and kinematic terms, but it is of the same order of magnitude as these terms.

In addition, Dykman, Platzman and Seddighrad calculate a decay mode due to modulation of the dielectric constant by phonons. This calculation requires the unphysical assumption of a liquid helium bath depth much greater than typical phonon wavelengths, and will not be discussed here, except to note that the decay rate they calculate is similar to that of the surface displacement modes.

Electronic-related decay and dephasing

Other decay and dephasing mechanisms do not couple to the surface level of the liquid helium. Instead, these modes couple to the electric field, causing decay or dephasing directly. These modes include direct coupling to radiation and coupling to Johnson noise in the electrode itself.

Radiation

The expected decay rate of an electric dipole[15, 19] is

$$W_{12} = \frac{E_2^{(C)} - E_1^{(C)}}{3\pi\epsilon_0 \hbar^4 c^3} \left| \langle 1| \mathbf{d_{12}} |2\rangle \right|^2 . \tag{1.45}$$

For this system, $\mathbf{d_{12}} \approx -ez_{12}$ yields an expected radiative decay time $W_{12} \approx 2\,\mathrm{s}^{-1}$, slow enough that other decay modes are more prevalent.

Johnson Noise

Johnson noise influences the system by introducing a fluctuation in the electric field, leading to fluctuations in the dipole energy terms which, if large enough, can cause direct decay to the ground state, much as the radiative term.

The effect of Johnson Noise on the electrode is a fluctuating voltage on the electrode of the form $\delta V_j = (4k_b T \mathcal{R} B)^{1/2}$, where T is the temperature of the dominant resistance, $\mathcal{R}$, and B is the bandwidth of the channel.

The overall effect of δV_j can be seen as a dipolar coupling to a qubit; however, because of the essential noise nature of δV_j, we can combine the bandwidth issue into the thermal issues by considering an autocorrelation function:

$$Q(\omega) = \int_0^\infty dt e^{i\omega t} \left\langle \delta\hat{\mathcal{E}}_\perp(t)\delta\hat{\mathcal{E}}_\perp(0)\right\rangle, \delta\hat{\mathcal{E}}_\perp(t) = \frac{\delta V_j a}{\eta^2}, \tag{1.46}$$

where a is the diameter of a post electrode and η is the distance from the electrode (assuming post geometry). In terms of Q, we can write both a term for the decay and the dephasing:

$$\Gamma_{12}^{(\mathrm{el})} = \frac{e^2 z_{12}^2}{\hbar^2} \mathrm{Re}\, Q(\Omega_{12}), \tag{1.47}$$

$$\Gamma_{\phi}^{(\mathrm{el})} = \frac{e^2 (z_{22} - z_{11})^2}{\hbar^2} \mathrm{Re}\, Q(0), \tag{1.48}$$

where $\Omega_{12} = (E_2^{(C)} - E_1^{(C)})/\hbar$ is the energy level splitting. Using this picture, the expected decay and dephasing take the form:

$$\Gamma_{12}^{(\mathrm{el})} = \frac{2(E_2^{(C)} - E_1^{(C)})\mathcal{R}_{\mathrm{el}} e^2 z_{12}^2 a^2}{\hbar^2 \eta^4}, \tag{1.49}$$

$$\Gamma_{\phi}^{(\mathrm{el})} = \frac{2k_B T_e x t \mathcal{R}_{\mathrm{ext}} e^2 (z_{22} - z_{11})^2 a^2}{\hbar^2 \eta^4}. \tag{1.50}$$

A reasonable value for the electrode resistance is $\mathcal{R}_{\mathrm{el}} = 0.1\,\Omega$, and for the post electrode, $a = 0.1\,\mu$m, and $h = 0.5\,\mu$m. Using these values as estimates, the decay rate is on the order of $\sim 5 \times 10^2\,\mathrm{s}^{-1}$. For calculating the dephasing rate, a reasonable set of values is $\mathcal{R}_{\mathrm{ext}} = 25\,\Omega$ and $T_{\mathrm{ext}} = 1\,\mathrm{K}$. Using these values, we find $\Gamma_\phi^{(\mathrm{el})} \sim 2.5 \times 10^5\,\mathrm{s}^{-1}$. The primary effect on the system due to Johnson noise is dephasing, not decay.

Summary of Decay Modes: The Big Picture

The dominant decay mode is due to surface modulation by either ripplons or phonons, and has a typical decay rate of $\sim 10^4$-$10^5\,\mathrm{s}^{-1}$. The dominant source of dephasing is due to coupling to Johnson noise in the electrode, with a typical time scale of $\sim 10^5\,\mathrm{s}^-1$. Both dephasing and decay rates indicate that individual gate operations should take place in a time much less than $\sim 10\,\mu$s, and that computations requiring large numbers of gate operations will require error correction.

Chapter 2

Gate Operations

2.1 Introduction

This chapter details operation of both single and two qubit gates. A set of gates sufficient for universal quantum computing is presented. These calculations are illustrative in nature, based on our model Hamiltonian as presented in Chapter 1, where only the operative terms in the Hamiltonian have been retained. Decoherence and decay mechanisms are not considered here, and it is assumed that changes in parameters can occur immediately. Only nearest neighbor interactions are considered, as nearby groundplanes change the nature of the Coloumb interaction from dipolar to quadropolar, which is an essentially nonresonant interaction for our system.

2.2 Qubit Hamiltonian

The qubit Hamiltonian can be written as an interaction Hamiltonian with the base Hamiltonian provided by a combintation of $H^{(0)}$ and $H^{(C)}(E_i^{(0)})$ for a set Stark shift for each individual qubit i, and the eigenfunctions from $|\Psi_i^{(C)}(E_i^{(C)})\rangle$. $H^{(C)}(E^{(\text{pert})}(t))$, $H^{(MW)}$, and $H^{(CI)}$ are modeled as perturbative interactions, where only the additional Stark shift potential is used in the perturbative interaction.

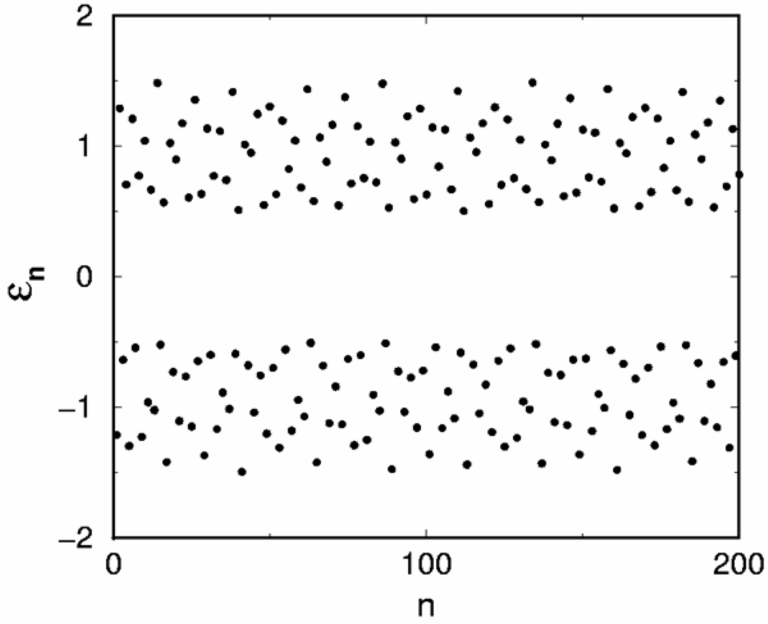

Figure 2.1: Base Stark shift states for computer operation. The pseudorandom numbers are generated by calculating $E_n^{(0)} = \left[(-1)^n - \sum_{k=2}^{n}(-1)^{\lfloor n/k \rfloor}\delta^{k/2}\right]\Delta$. These base Stark shifts are taken with respect to the microwave resonance Stark shift.

2.2.1 Base Computer State and Operation

In the base computer state, each qubit is Stark shifted into a different energy state to prevent spontaneous interactions. In addition, odd numbered qubits are Stark shifted such that they are on the opposite side of the microwave frequency from the even numbered qubits. This allows qubits to be brought into resonance with the microwave field without having the same energy splitting as their neighbors, effectively preventing first-order interactions. The addition of a pseudorandom term improves this dampening of local excitations by impeding second-order interactions as well. Dykman et. al. have proposed that such a state can be constructed by using a pseudorandom number generation technique so each qubit has a precisely known base Stark shift and fits the above criteria.[16] Figure 2.1 shows such a state.

The available control parameters are the set of individual qubit control fields, $E_j(t)$, and the presence or absence of a global microwave field.

2.3 Computation Parameters

For these computations, the energy level splitting of a qubit is modeled as

$$\langle 2|_i H^{(0)} + H^{(C)}\left(E_i(t)\right)|2\rangle_i - \langle 1|_i H^{(0)} + H^{(C)}\left(E_i(t)\right)|1\rangle_i = \hbar\omega_{21}^{(i)}(t), \tag{2.1}$$

where $|n\rangle = |\Psi_n^{(0)}\rangle$. This model is used for each simulation, except for the Phase gate simulation, as discussed below.

Single qubits are modeled under the interaction representation as

$$\left|\tilde{\Psi}\right\rangle_i = A_1^{(i)}(t)\,|1\rangle_i + A_2^{(i)}(t)e^{-i\omega_{21}^{(i)}(t)t}\,|2\rangle_i\,, \tag{2.2}$$

except, again, for the Phase gate, as discussed below. Each operator must also be modified for the interaction representation as well, assuming the form

$$\tilde{U}_i = e^{-iH_i^{(0)}t/\hbar}U_i e^{iH_i^{(0)}t/\hbar}, \tag{2.3}$$

where $H_i^{(0)} = \hbar\omega_{12}^{(i)}(t)\,|2\rangle_i\,\langle 2|_i$, and any change in the energy level is assumed to occur both instantaneously and adiabatically.

Two qubit interactions are regarded as the tensor product of two individual qubits, with new constants $C_{ij}(t) = A_i^{(1)}A_j^{(2)}$.

The physical parameters for these qubits are taken from our design of the post electrode and the working parameters of our microwave system. The inter-qubit spacing, d, is taken to be $0.5\,\mu$m. The microwave frequency, Ω, is 140 GHz. The intensity of the microwave field, $E^{(\mathrm{MW})}$, is 10 V/m. Given these parameters, the expected Rabi frequency,

$$f_{\mathrm{rab}} = \frac{1}{h}2eE^{(\mathrm{MW})}\left|z_{12}\right|,$$

is about 10 MHz. The expected frequency of SWAP operations,

$$f_{\mathrm{SWAP}} = \frac{1}{h}\frac{e^2}{2\pi\epsilon_0}\frac{z_{12}^2}{d^3},$$

is about 50 MHz.

2.4 Single Qubit Gates

Single qubit gates are implemented as Stark shift operations on individual qubits, either with or without an applied microwave field. For each gate, the model interaction wave function and Hamiltonian are discussed. Both of these interactions are solveable in closed form, but are solved numerically in the interest of saving time.

2.4.1 Phase

Phase gates are implemented by applying a Stark shift to an individual qubit, changing the effective frequency of the excited state. For this calculation, we do not take the wave functions to be of the form of Equation (2.2), but instead take

$$\left|\tilde{\Psi}\right\rangle = A_1(t)\left|1\right\rangle + A_2(t)e^{-i\omega_{21}t}\left|2\right\rangle, \tag{2.4}$$

with $\omega_{21} = 130/2\pi\,\text{GHz}$ fixed. We then introduce our perturbation potential as

$$U = -eE(t)z \tag{2.5}$$

which yields two coupled differential equations for $A_1(t)$ and $A_2(t)$:

$$\begin{aligned} i\hbar\dot{A}_1(t) &= -eE(t)z_{11}A_1(t) - eE(t)z_{12}e^{-i\omega_{21}t}A_2(t) \\ i\hbar\dot{A}_2(t) &= -eE(t)z_{12}e^{i\omega_{21}t}A_1(t) - eE(t)z_{22}A_2(t). \end{aligned}$$

Figure 2.2 shows a time series computation for a Phase gate.

2.4.2 NOT

NOT gates are implemented by using Rabi oscillations caused by resonant interactions between a qubit and an applied microwave field. The target qubit is Stark shifted so it is in resonance with the active microwave field. Using the form of Equation (2.2) for our wave functions, with $\omega_{12}(t) = \omega_1 + \Gamma(t_1, t_2; t)[\Omega - \omega_1]$, and

$$U = \Gamma(t_3, t_4; t)eE^{(MW)}z\sin(\Omega t), \tag{2.6}$$

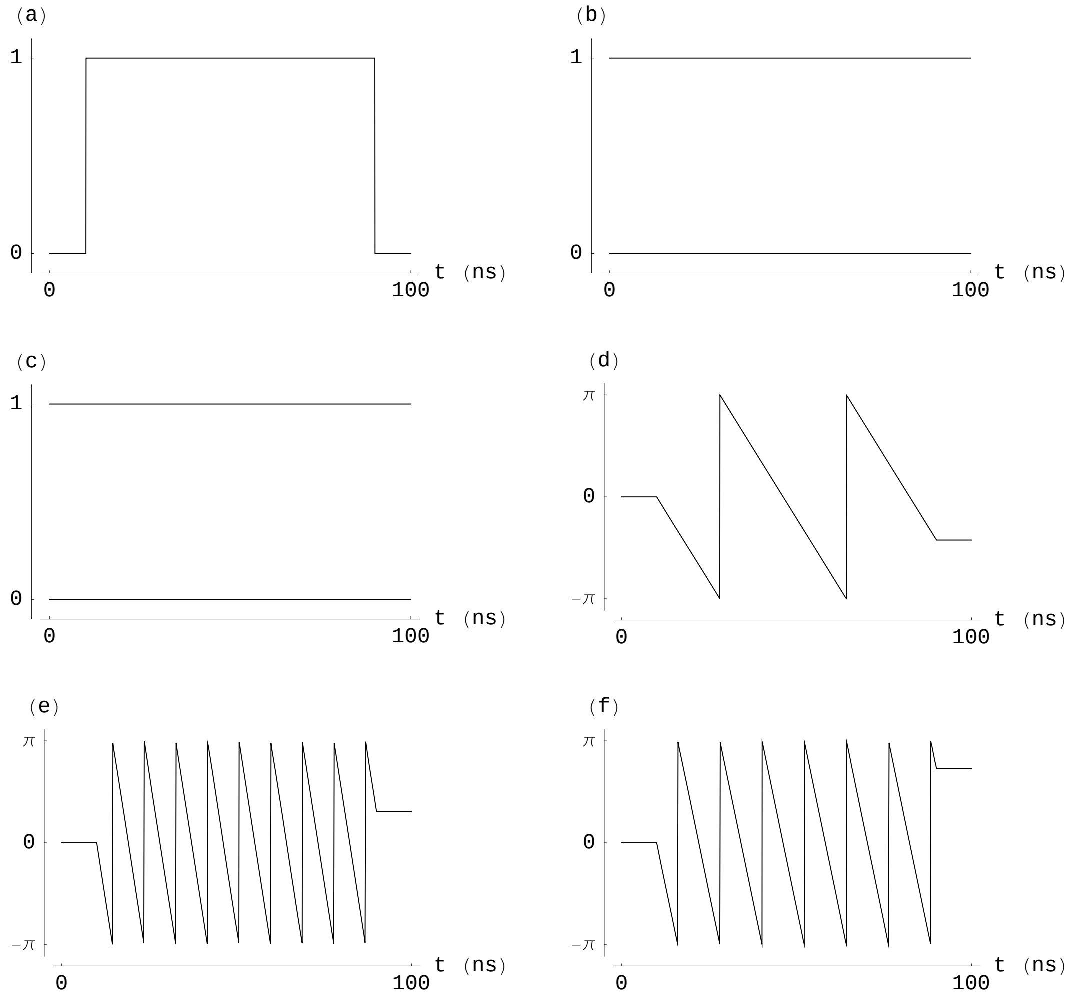

Figure 2.2: Time series computation of a Phase Gate. (a) Shape of the phase shifting pulse applied. The amplitude of the applied field is 10 V/m. (b) For one run of the simulation, the qubit is in the ground state, and stays in it. (c) For the second run, the simulation is in the excited state. (d) Phase shift for the ground state. (e) Phase shift of the excited state. (f) Phase shift difference between the ground state and the excited state.

for the potential, where $\Gamma(\tau_1, \tau_2; t)$ is a square pulse function where

$$\Gamma(\tau_1, \tau_2; t) = \begin{cases} 0 & t < \tau_1 \\ 1 & \tau_1 \leq t \leq \tau_2, \\ 0 & t > \tau_2 \end{cases}$$

ω_1 is the base energy state of the qubit, and Ω is the frequency of the applied microwave field, we can derrive a set of coupled equations for the NOT operation:

$$\begin{aligned} i\hbar\dot{A}_1(t) &= eE^{(MW)}\Gamma(t_3, t_4; t)\sin(\Omega t)\left[z_{11}A_1(t) + z_{12}e^{-i\omega_{12}(t)t}A_2(t)\right] \\ i\hbar\dot{A}_2(t) &= eE^{(MW)}\Gamma(t_3, t_4; t)\sin(\Omega t)\left[z_{12}e^{i\omega_{12}(t)t}A_1(t) + z_{22}A_2(t)\right] \end{aligned}$$

Figure 2.3 shows a time series computation of a NOT gate.

2.5 Two Qubit Gates

Two qubit gates are implemented using different aspects of $H^{(CI)}$ and $H^{(MW)}$. Only nearest neighbor interactions are considered. The wave functions used here are tensor products of the two qubit states:

$$\begin{aligned} |\Psi_i\Psi_j\rangle &= C_{11}(t)\,|11\rangle + C_{12}(t)e^{-i\omega_{12}^{(j)}(t)t}\,|12\rangle + C_{21}(t)e^{-i\omega_{12}^{(i)}(t)t}\,|21\rangle + \\ &\quad C_{22}(t)e^{-i\left(\omega_{12}^{(j)}(t)+\omega_{12}^{(i)}(t)\right)t}\,|22\rangle \end{aligned} \tag{2.7}$$

2.5.1 SWAP

SWAP gates are implemented by Stark shifting two neighboring qubits to the same energy state. This introduces a degenerecy in the eigenstates which allows the two qubits to exchange state information. By leaving the two qubits in the same Stark shift state for the proper period of time, a perfect swap can be implemented. The specific form the Coloumb interaction takes on for this swap gate is

$$U = \frac{e^2}{2\pi\epsilon_0}\frac{z_{12}^2}{d^3}\left(|12\rangle\langle 21| + |21\rangle\langle 12|\right). \tag{2.8}$$

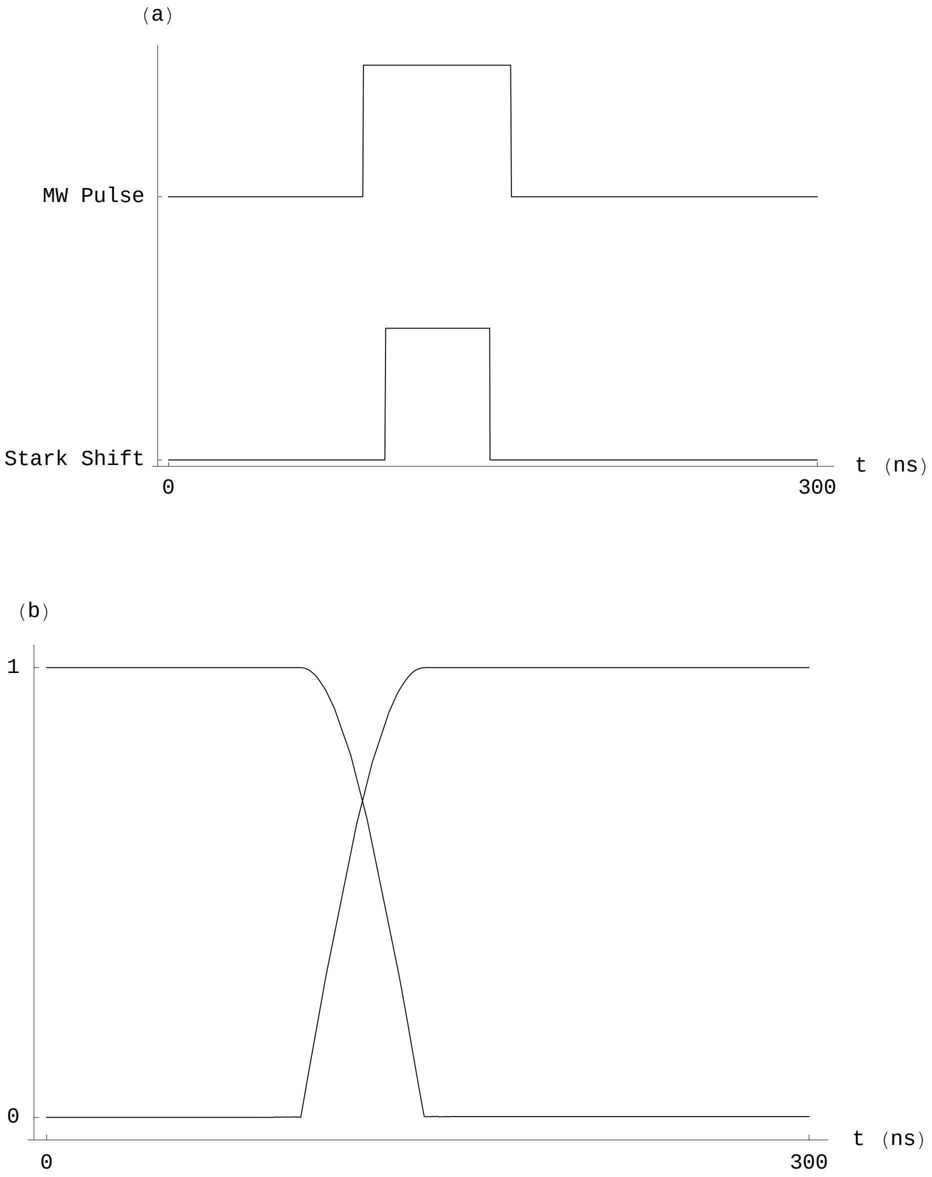

Figure 2.3: Time series computation of a NOT Gate. For this computation, $H^{(C)}$ is entirely treated as part of the base hamiltonian. (a) Shape of the pulse applications. The upper curve shows the application of a microwave field, with an amplitude of 10 V/m. The lower curve shows the applied Stark shift used to bring the qubit in resonance with the microwave field, which is applied for 1/2 the expected Rabi oscillation time. (b) Amplitude of the $|0\rangle$ and $|1\rangle$. The system starts in the $|0\rangle$ state, and ends in the $|1\rangle$ state. The phase data is very noisy as expected for this computation method, and is not presented.

The rest of the Coloumb interaction terms are not resonant in this pulse sequence, so they are not considered here.[15] With this form, the coupled differential equations to be solved are:

$$
\begin{aligned}
i\hbar\dot{C}_{11}(t) &= 0 \\
i\hbar\dot{C}_{12}(t) &= \frac{e^2}{2\pi\epsilon_0}\frac{z_{12}^2}{d^3}e^{-i\left[\omega_{12}^{(1)}(t)-\omega_{12}^{(2)}(t)\right]t}C_{21}(t) \\
i\hbar\dot{C}_{21}(t) &= \frac{e^2}{2\pi\epsilon_0}\frac{z_{12}^2}{d^3}e^{i\left[\omega_{12}^{(1)}(t)-\omega_{12}^{(2)}(t)\right]t}C_{12}(t) \\
i\hbar\dot{C}_{22}(t) &= 0.
\end{aligned}
$$

For this time series computation, $\omega_{12}^{(2)}(t)$ is held constant, and $\omega_{12}^{(1)}(t)$ is brought into the same Stark shift state for the appropriate ammount of time.

Figure 2.4 shows a time series computation for the SWAP gate.

2.5.2 $\sqrt{\mathrm{SWAP}}$

An ordinary SWAP operation is not enough for universal quantum computing—the resulting state can still be writen as the simple tensor product of single qubit states. Interestingly enough, however, half of a swap operation does force a state where a simple tensor product of single qubit states is no longer sufficient. The $\sqrt{\mathrm{SWAP}}$ is implemented simply by shifting the qubits into resonance with respect to each other for half of the time required to perform a full swap. A computation is not presented for this gate operation—it would look essentially the same as the SWAP calculation, except the pulse width would be halved.

CNOT

The CNOT gate is implemented by Stark shifting a qubit such that its interaction with an applied microwave field depends upon the state of its neighbor (the control qubit): if the control qubit is in the excited state, then our qubit is in resonance with the microwave field, and undergoes Rabi oscillations; if the control qubit is in the ground state, then our qubit is not in resonance with the microwave field,

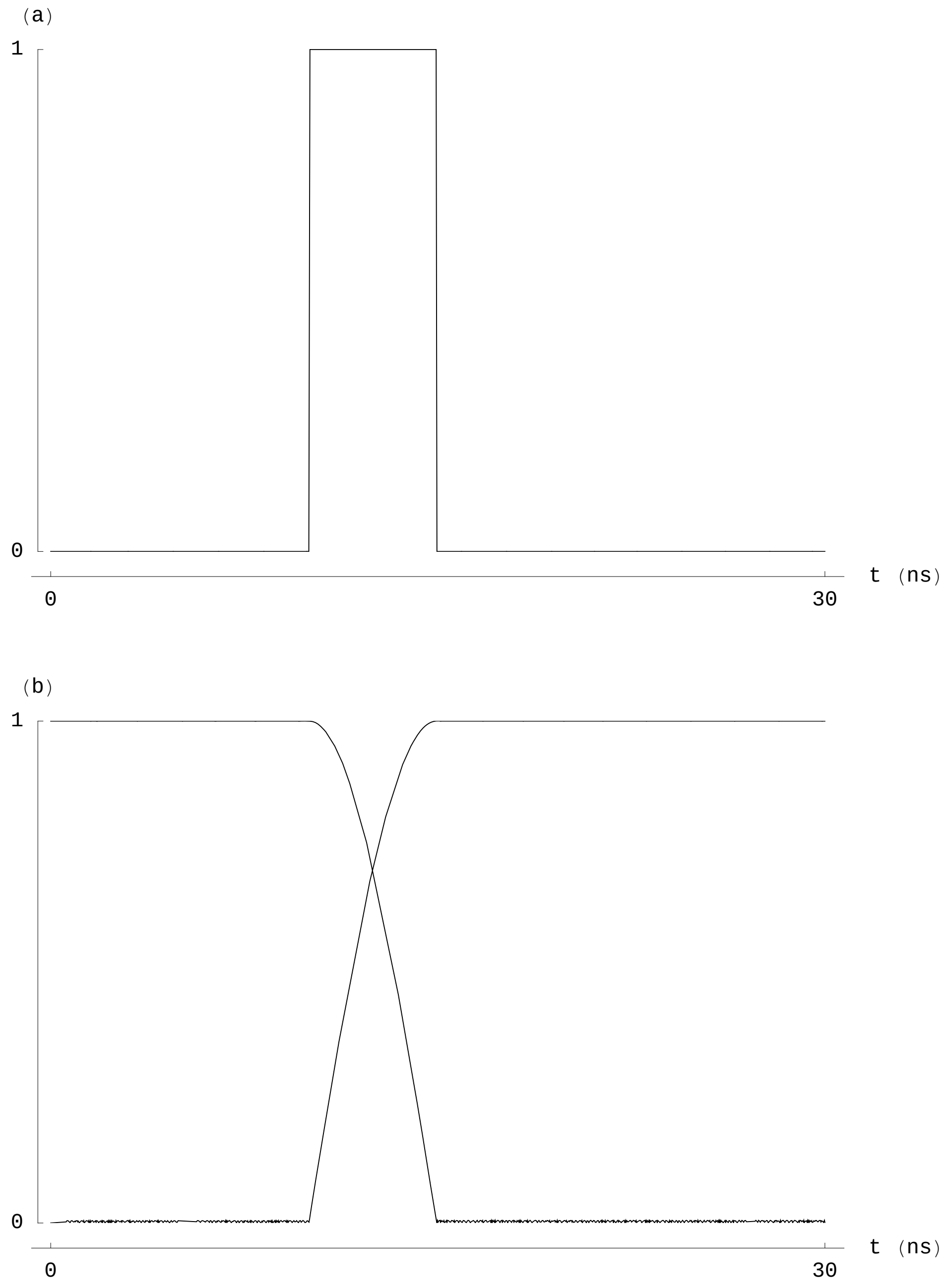

Figure 2.4: Time series computation of a SWAP Gate. For this computation, $H^{(C)}$ is entirely treated as part of the base Hamiltonian. (a) Shape of the pulsed Stark shift. The two qubits begin 20 GHz apart. One of them is then shifted the difference to bring both qubits into resonance. (b) Amplitude of the qubit states. Shown are the $|12\rangle$ and the $|21\rangle$ state. The qubit begins in the $|12\rangle$ state and is swapped to the $|21\rangle$ state. The phase data is noisy as expected for this computation method, and is not presented.

and stays in the same state. The important part of the Coloumb interaction can be written as

$$U = \frac{e^2}{16\pi\epsilon_0}\frac{|z_{22}-z_{11}|^2}{d^3}\left(|22\rangle\langle 22| - |21\rangle\langle 21| - |21\rangle\langle 21| + |11\rangle\langle 11|\right), \qquad (2.9)$$

as the rest of the Coloumb interaction is not in resonance for this operation.[15] Unlike for the NOT operation, only the resonant portion of the microwave field is considered here. Our differential equations can then be written as:

$$\begin{aligned} i\hbar\dot{C}_{11}(t) &= \frac{e^2}{16\pi\epsilon_0}\frac{|z_{22}-z_{11}|^2}{d^3}C_{11}(t) + eE^{(MW)}\Gamma(t_3,t_4;t)\sin(\Omega t) \\ &\quad \times \left(e^{-i\omega_{12}^{(1)}(t)t}C_{21}(t) + e^{-i\omega_{12}^{(2)}(t)t}C_{12}(t)\right) \end{aligned}$$

$$\begin{aligned} i\hbar\dot{C}_{12}(t) &= -\frac{e^2}{16\pi\epsilon_0}\frac{|z_{22}-z_{11}|^2}{d^3}C_{12}(t) + eE^{(MW)}\Gamma(t_3,t_4;t)\sin(\Omega t) \\ &\quad \times \left(e^{-i\omega_{12}^{(1)}(t)t}C_{22}(t) + e^{i\omega_{12}^{(2)}(t)t}C_{11}(t)\right) \end{aligned}$$

$$\begin{aligned} i\hbar\dot{C}_{21}(t) &= -\frac{e^2}{16\pi\epsilon_0}\frac{|z_{22}-z_{11}|^2}{d^3}C_{21}(t) + eE^{(MW)}\Gamma(t_3,t_4;t)\sin(\Omega t) \\ &\quad \times \left(e^{i\omega_{12}^{(1)}(t)t}C_{11}(t) + e^{-i\omega_{12}^{(2)}(t)t}C_{22}(t)\right) \end{aligned}$$

$$\begin{aligned} i\hbar\dot{C}_{22}(t) &= \frac{e^2}{16\pi\epsilon_0}\frac{|z_{22}-z_{11}|^2}{d^3}C_{22}(t) + eE^{(MW)}\Gamma(t_3,t_4;t)\sin(\Omega t) \\ &\quad \times \left(e^{i\omega_{12}^{(1)}(t)t}C_{12}(t) + e^{i\omega_{12}^{(2)}(t)t}C_{21}(t)\right) \end{aligned}$$

For computational purposes, $\omega_{12}^{(1)}(t) = 130/2\pi\,\text{GHz}$ and

$$\omega_{12}^{(2)}(t) = \Omega - \frac{1}{\hbar}\frac{e^2}{8\pi\epsilon_0}\frac{|z_{22}-z_{11}|^2}{d^3},$$

both fixed. The frequency of the CNOT operation is the same as the frequency of a NOT gate.

Figure 2.5 shows a time series computation of a CNOT gate.

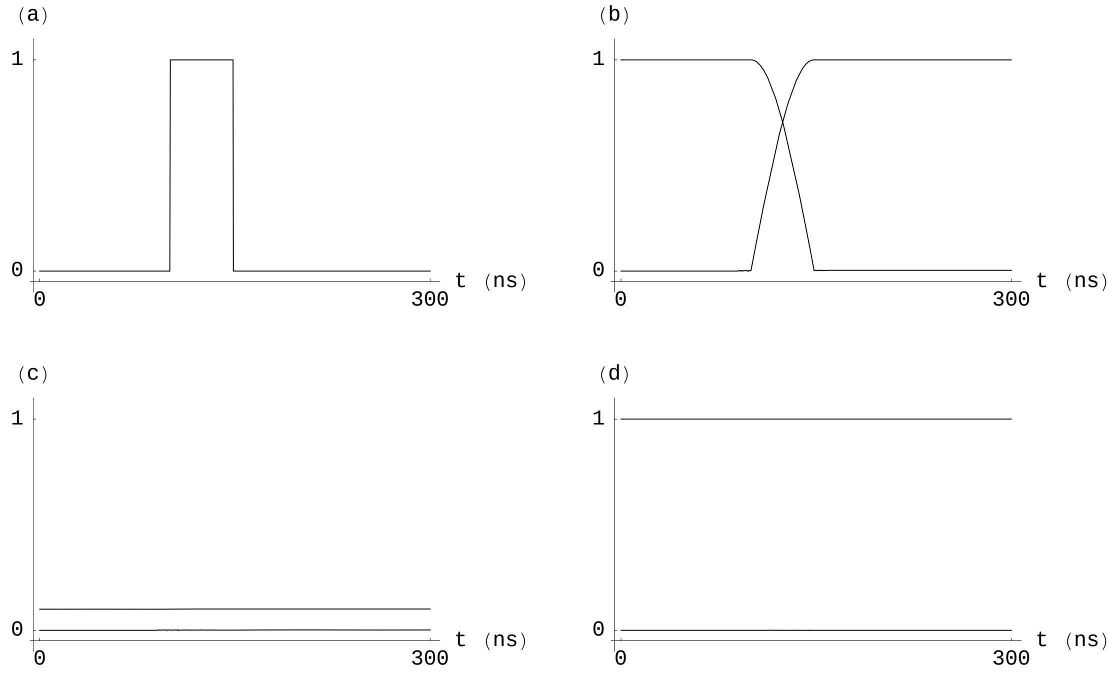

Figure 2.5: CNOT Gate time series computation. For this calculation, the Stark shift states of each qubit are held constant. (a) Shape of the microwave field pulse. (b) Amplitudes of the $|21\rangle$ and $|22\rangle$ states. The system starts in the $|21\rangle$ state, and ends in the $|22\rangle$ state. (c) Amplitudes of the $|11\rangle$ and $|12\rangle$ states. The $|12\rangle$ state has an offset of 0.1 added so the two lines do not overlap. (d) Amplitude of the $|21\rangle$ and $|22\rangle$ state where the Stark shift of the second qubit has been tuned away from the CNOT resonance. In this case, no NOT operation occurs.

Chapter 3

Microfabrication

3.1 Introduction

Three different microfabrication projects were undertaken to assemble this system: an electron source suitable for use at low temperatures, a scheme for the detection of the final state of the electrons, and a series of electrodes to trap and Stark shift electrons.

3.2 Electron Sources

Traditionally, loops of tungsten wire are used for emission of electrons in low temperature experiments; either as thermal emitters or as glow discharge devices. At low temperatures, both of these techniques inject a large amount of heat into the surrounding sample chamber, and thus require a large cycle time for re-cooling the sample before experiments can be done. With this in mind, we looked for a different electron source, and settled on porous silicon as a candidate.

3.2.1 Porous Silicon[1]

In our experiments, we first created diodes with thick ($\sim$ 3-10 μm) PS layers, but soon discovered that these devices did not work at 77 K or lower temperature.

---

[1] See [44] for details.

We switched our focus over to thinner PS layers, and manufactured devices with PS layers less than 0.5 μm thick. These devices worked down as far in temperature as our dilution refrigerator let us work, about 50 mK. For these devices, we measured the emission current and the energy distribution of the emitted electrons as a function of diode bias current and temperature.

The mechanism of electron release appeared to be discharging of stored charge on the nanocrystallites (shallow trap states) via a Poole-Frankle mechanism at temperatures lower than 77 K. As a result, the total emission of the device is controllable by pulse shape and diode bias voltage. Higher bias voltages lead to the expulsion of more electrons, as more of these traps come into play.

A sample set of data for one of our PS diodes is presented in Figure 3.1. This data is taken for diodes with no helium film covering the interior of the sample cell. The diodes did work in the presence of a helium film as well, but the emission current was heavily suppressed, as emitted electrons had to first tunnel through the helium film. In practice, it was difficult to use these diodes in the presence of a helium film. In addition, exposure of a PS diode to helium vapor at any temperature higher than 4 K resulted in complete device failure until the diode was kept under vacuum at room temperature for an extremely long time ($\sim$ 24 hours).

Fabrication Details[2]

The fabrication of the PS diodes was done in the lab of Professor Michael Sailor at UCSD.

1. Clean a piece of n+ doped Si(100) wafer in the standard fashion.

2. Photoannodize the wafer in a 1:1 :: aqueous HF : ethanol solution under a white halogen bulb at an intensity of 8-11 mW/cm^2. The anodizing current density should be 30-35 mA/cm^2.

3. Perform Rapid Thermal Oxidation (RTO) with a turbulence-free flow of O_2 at 900 °C for 5-6 minutes.

---

[2] Standard microfabrication steps are discussed in Appendix B.

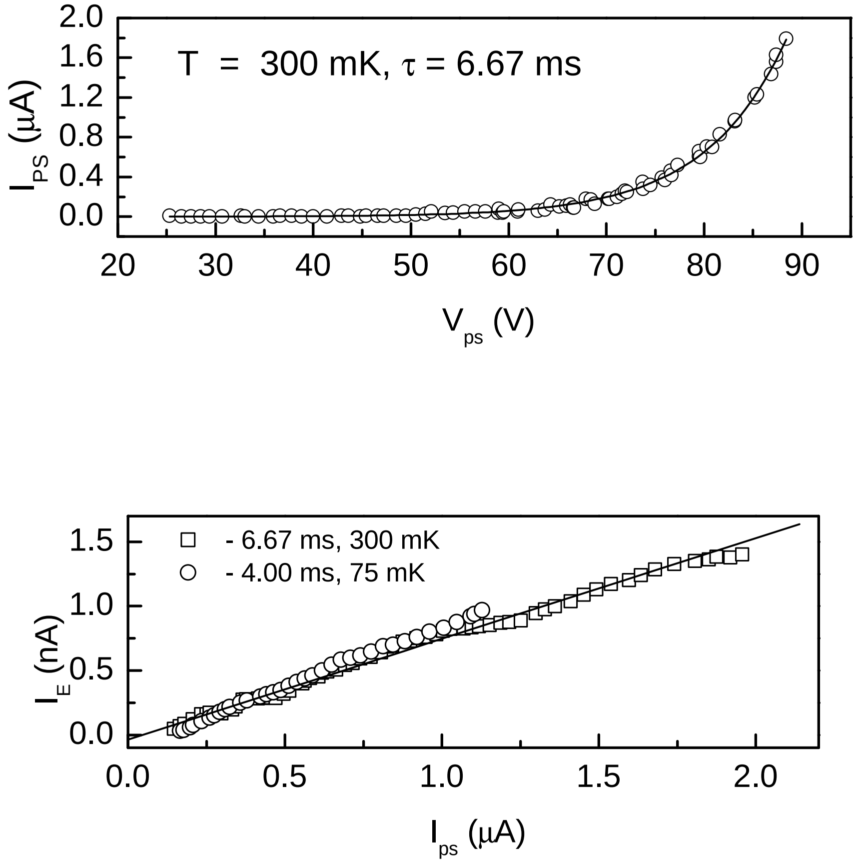

Figure 3.1: PS Diode Conductivity and Emission Data. The upper graph shows the diode current as a function of the diode voltage. The lower graph shows the emission current as a function of the diode current. In each graph, the temperature and the applied voltage pulse width are listed.[44]

4. Anneal the diode with a turbulence-free flow of N_2 at 900 °C for 30 seconds.
5. Remove the oxide formed on the back of the wafer using HF.
6. Evaporate a layer of Cr/Au onto the PS patch in the center of the wafer. The Cr/Au layer needs to be thin. In our experiments, we used 10 Å/ 70 Å. Less Au does not work: it forms islands on the Cr rather than a continuous layer.
7. Evaporate an ohmic contact on the back of the wafer using Cr/Au. The thickness of this layer was 50 Å Cr / 1000 Å Au.

3.2.2 Thoriated Tungsten Wire

Given our problems with PS diode reliability, we fabricated a back-up electron source in a more standard way by making a thoriated tungsten filament. This source is made by taking a .0015 in thick thoriated tungsten wire and crimping the ends in thin copper capillary. The crimped ends effectively cold weld the wire to the copper. The capillary is then firmly fixed in some kind of holder and epoxied in place. Using another piece of wire, the thoriated tungsten wire is then gently pulled until there is a sharp kink in the wire. When the wire is used as an emission source in the presence of an electric field, the largest gradients will be around the sharp kink, so that will be the primary point of emission.

Support Electronics

There are two potential operation modes for the thoriated tungsten filament in this apparatus: glow discharge and thermal emission. The pulse electronics for glow discharge operation are shown in Figure 3.2, and the pulse electronics for thermal emission are shown in Figure 3.3. In practice, thermal emission was not used, as the filament tended to be fragile, and broke before emission could be observed, and a broken filament is still perfectly good as a glow discharge source.

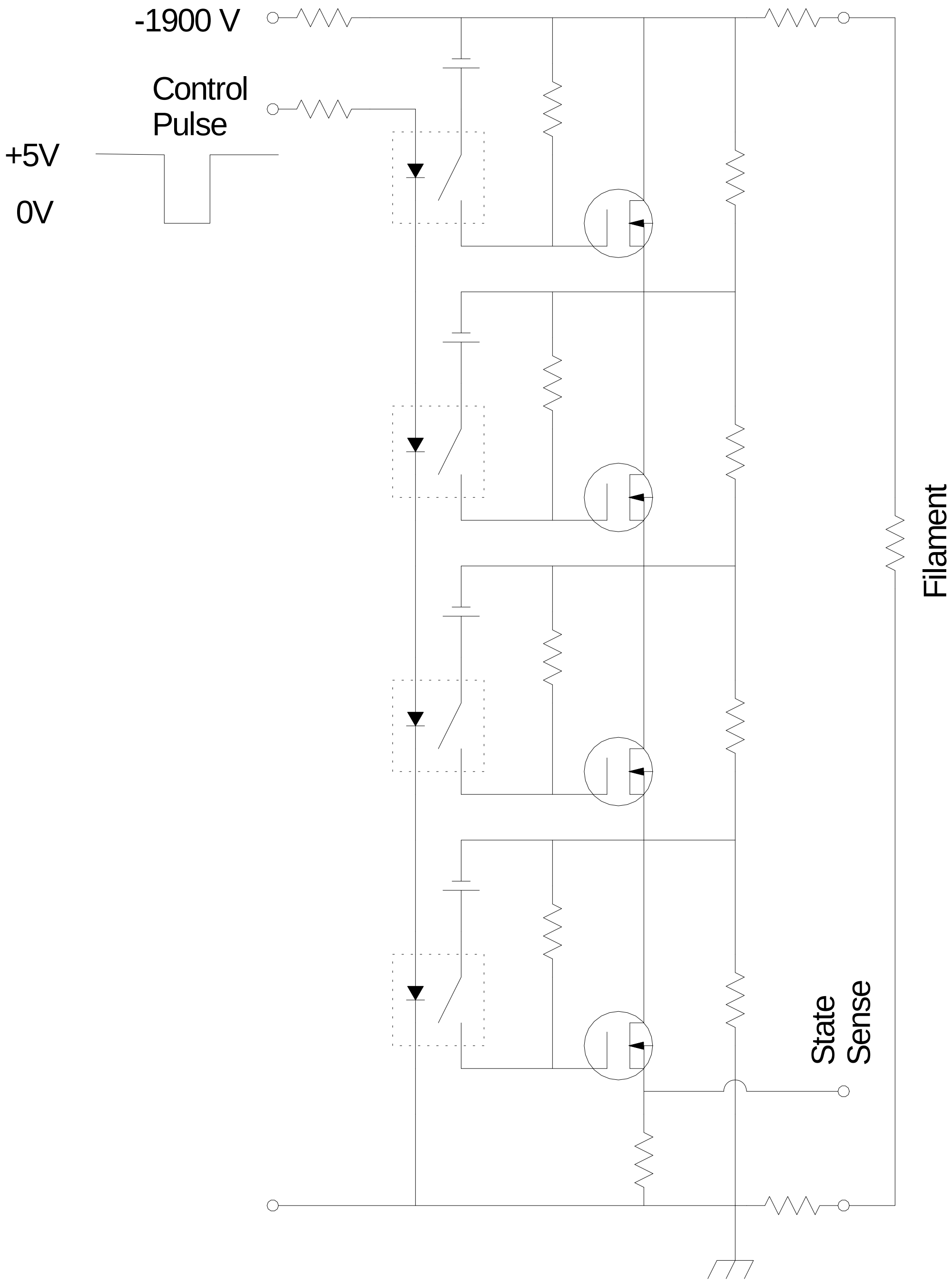

Figure 3.2: High voltage, low current switch for glow discharge filament. The voltage appears on the output when the control pulse is at ground. The control pulse is provided by a HP 33120A waveform generator.

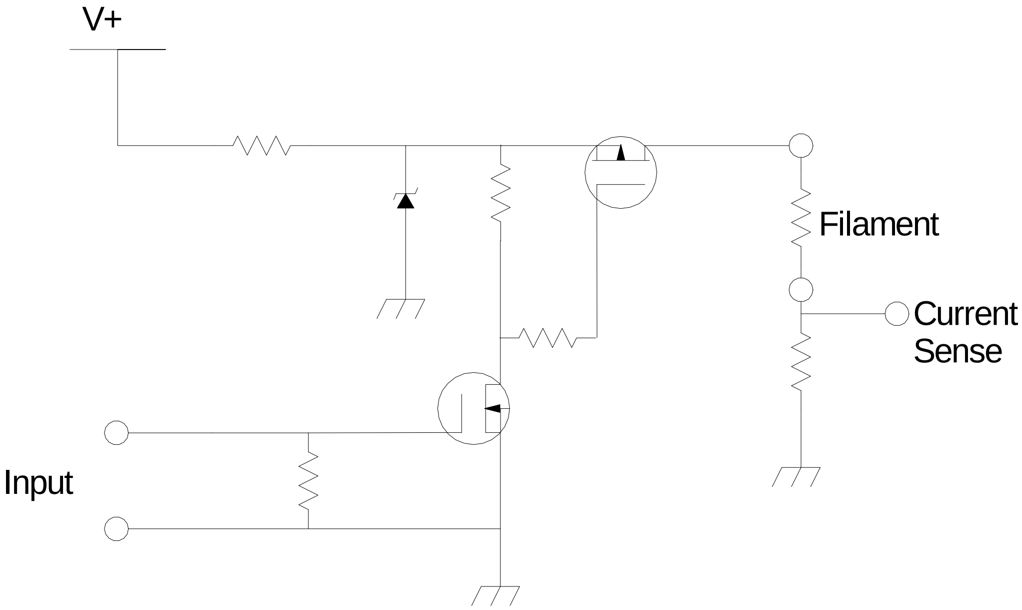

Figure 3.3: High current, low voltage switch for thermal filament. The current appears on the output when the control pulse is +5 V. The control pulse is provided by a HP 33120A waveform generator.

3.3 Electron Detection

In their original paper on electrons on helium quantum computing, Platzman and Dykman proposed using a channel plate for electron detection.[47] To our knowledge, nobody has attempted to use a channel plate under these conditions, possibly due to the superfluid helium film that would saturate the pores and thereby impede its operation. Instead, research has focused primarily on two different methods for detecting electrons: single electron transistors[43] and superconducting particle detectors.

A superconducting particle detector is not a new idea.[3] The basic concept is that any input of energy to a superconductor held near its superconducting transition—by either heating to near T_c or use of a magnetic field—will cause a part of the superconductor to go normal, and sensitive resistance measurements will register a change in resistance. The current state of the art superconducting particle detectors are photon detectors used on satellites as part of the experimental program on dark matter, and are capable of detecting photons at a few eV.[6] Their detector designs require large surface area detectors and precision optics because photons cannot be attracted to the detector. In our case, since we are looking for electrons, we can use a bias voltage on our detectors to attract the incoming electrons to hit the wafer nearby the microwire, as well as impart extra energy to the incoming electron, making the impact more energetic, and thus easier to detect. As a trade off, we acquire the equally daunting problem of needing a ground plane to shield the detector from pickup voltages from various pulses applied within the sample chamber.

3.3.1 First Revision

A picture of the first revision of detector can be seen in figure 3.4. The microwires are $1\,\mu$m wide. The opening in the ground plane is $10\,\mu$m by $40\,\mu$m. This design was produced using both aluminum (for proof of concept devices) and titanium as the superconductor. Holes in the wafer are etched using the Bosch process nearby the bolometers.

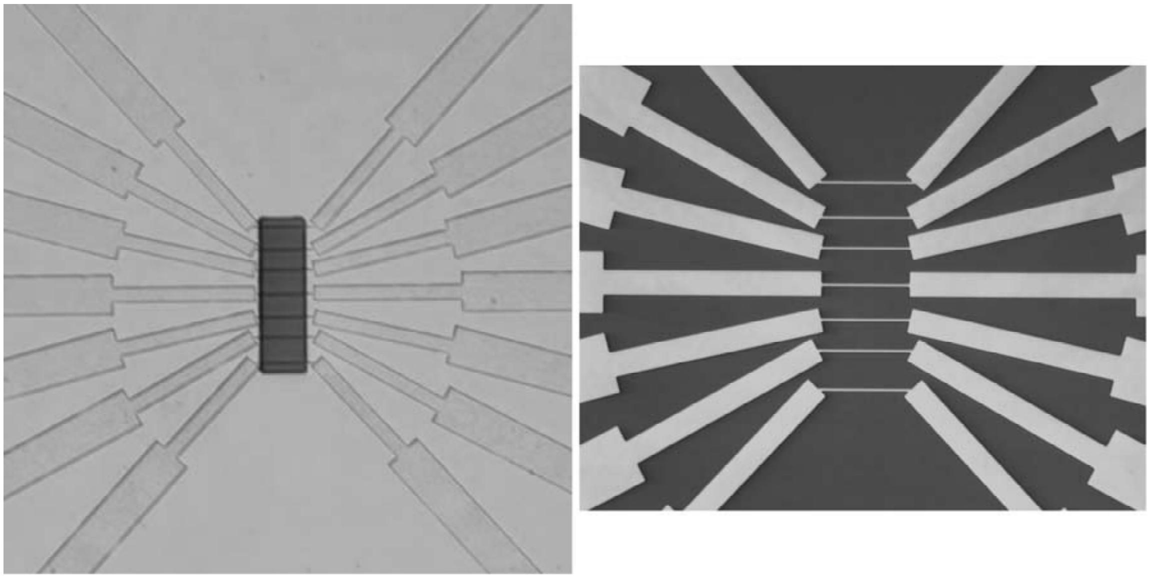

Figure 3.4: Initial Detector Design. The microwires are 10 μm by 1 μm. The hole in the ground plane is 40 μm by 10 μm. Each die has 7 detectors. A blowup of the microwires is shown on the right before the ground plane is put down.

Effective Detector Cross Section

If we consider our detector as a free-standing wire in space behind a ground plane, we can write down energy equations for the motion of an electron moving toward the hole, assuming the electron's velocity is in the vertical direction, and that far away from the hole, the detector is screened effectively by the ground plane:

$$\frac{1}{2}mv_0^2 - \frac{1}{4\pi\epsilon_0}e^2 2z = \frac{1}{2}m\dot{r}^2 + \frac{1}{2}mr_f^2\dot{\theta}_f^2 - eV \tag{3.1}$$

where v_0 is the initial electron velocity, r_f is the radius of closest approach to the wire, $\dot{\theta}$ is the angular velocity of the electron at closest approach, and V is the voltage on the detector wire itself. (See Figure 3.5.) At closest approach, $\dot{r} = 0$. In addition, since angular momentum in the system must be conserved, we can rewrite $r^2\dot{\theta} = bv_0$, where b is the initial horizontal distance from the electron to the wire, and simplify equation (3.1) to:

$$\frac{1}{2}mv_0^2 - \frac{1}{4\pi\epsilon_0}\frac{e^2}{2z} = \frac{1}{2}\frac{b^2}{r^2}mv_0^2 - eV. \tag{3.2}$$

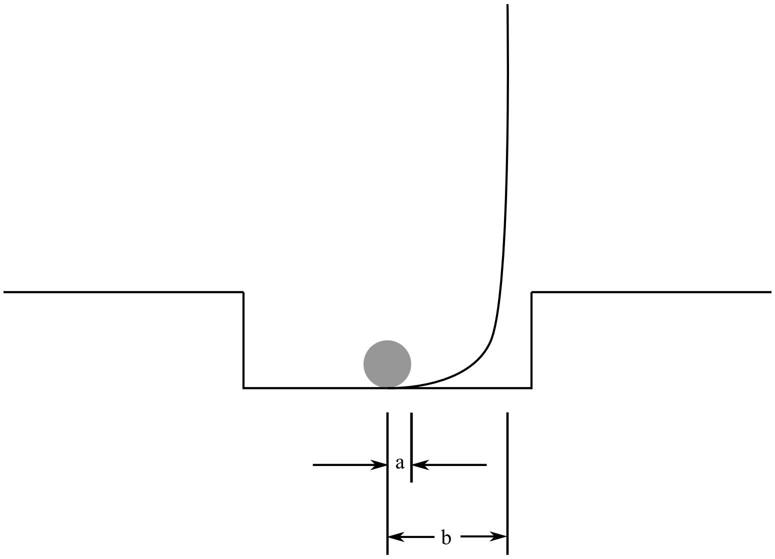

Figure 3.5: Geometry for detector cross section calculation. The detector is taken to have a radius a, and the impact parameter of the electron is b.

For a particular voltage on the wire, we can solve for b, assuming that $r \leq a$, the effective detector radius. We find that

$$\frac{b^2}{a^2} = 1 + \frac{1}{K_0}\left[\frac{1}{4\pi\epsilon_0}\frac{e^2}{2z} - eV\right], \tag{3.3}$$

where K_0 is the initial kinetic energy of the electron. If $K_0 = 1\,\mathrm{eV}$, $z = 0.5\,\mathrm{mm}$, and $V = 5\,\mathrm{V}$, we find that $b^2/a^2 \simeq 6$, indicating that to hit our wire, $b \leq 2.45a$.

All that remains is to calculate the effective detection radius. Figure 3.6 shows calculations for expected rise in temperature of $\mathrm{SiN_x}$ at 300 mK for electron impacts at different distances from a detector for 5 eV events. These curves were calculated by second order differencing[52] of Newtonian cooling to the substrate under cylindrical symmetry for a delta function energy influx. If we assume that a rise of 1 mK in the $\mathrm{SiN_x}$ is sufficient to cause our detector to go normal, then we require an electron to hit no more than 2.0 μm away from the wire, which gives us an effective detection radius of $a = 2.5\,\mu\mathrm{m}$, and an effective limit on our impact parameter to $b = 6.12\,\mu\mathrm{m}$.

Fabrication Details[3]

This fabrication was done at the clean room at UCSB.

1. Clean a 100 mm wafer in the standard fashion.
2. Deposit $2\,\mu\mathrm{m}$ of $\mathrm{SiO_2}$ by PECVD.
3. Spin, bake, expose, and develop a layer of SPR 510A as a negative photoresist. The pattern exposed is the detector leads and detector microwire.
4. Deposit the desired superconductor and a gold capping layer by e-beam evaporation.
5. Lift off the photoresist using acetone.
6. Spin, bake, expose, and develop a resist bilayer of LOL2000 and SPR955CM as a negative photoresist. The pattern exposed is the detector ground plane.

---

[3] Standard microfabrication steps are discussed in Appendix B.

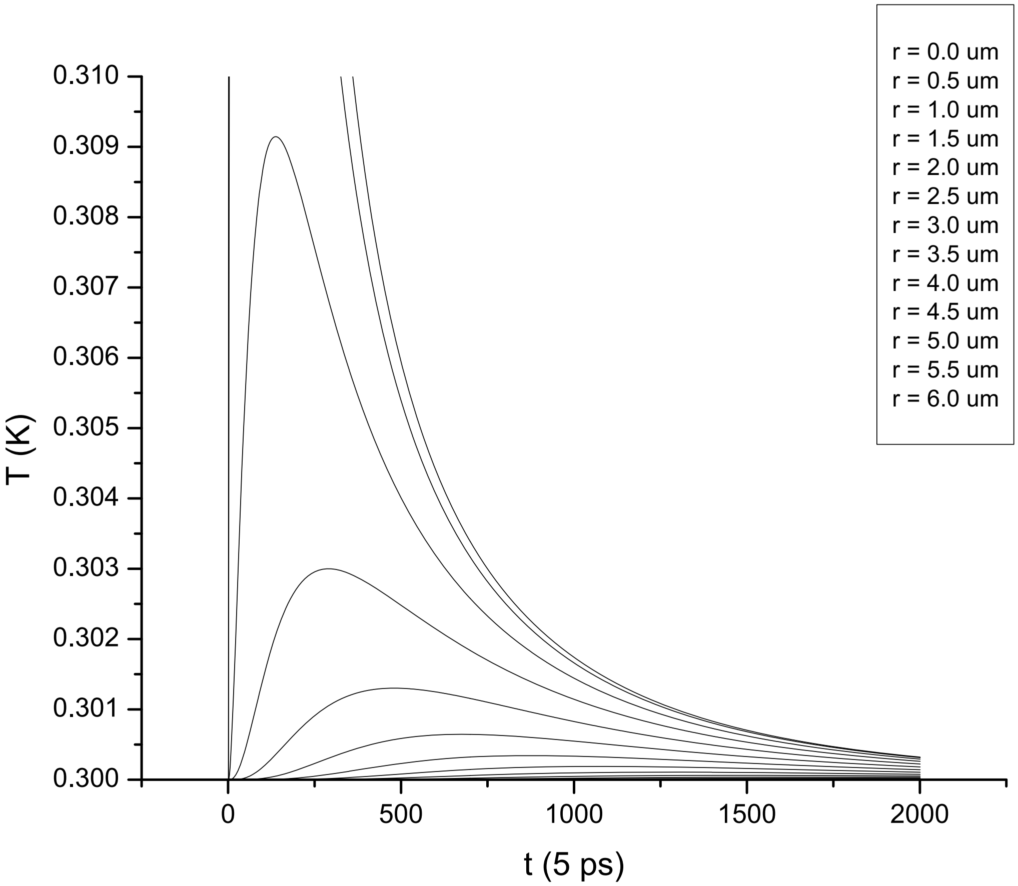

Figure 3.6: Expected temperature as a function of time for an electron impact a given distance away from a detector. The different curves represent an ever increasing distance from the impact site. For an electron impacting 2.0 μm away from a detector, the expected temperature of the $\mathrm{SiN_x}$ under the detector rises from 300 mK to 301 mK at a time of around 2 ns. These curves were obtained by second order differencing of Newton's heat transfer equation.

7. Deposit 1 μm $\mathrm{SiN_x}$ by RF sputtering.
8. Deposit a thick layer of Ti/Au for the ground plane by sputtering.
9. Lift off the photoresist using acetone.
10. Using the Bosch process in a RIE machine, etch holes through the wafer. The depth of the hole is monitored by a laser.
11. Dice the wafer.

3.3.2 Second Revision

There were basic problems with the initial detector design. Mainly, the combination of the hole in the ground plane being so small and the detector itself not covering a large area led to a small cross section for electron detection. In addition, the T_c of the detectors was high.

The first problem was solved by both increasing the size of the hole in the ground plane, to 1 mm by 1 mm, and changing the detector design from a simple wire to a meander pattern that took up 17 μm laterally (see Figure 3.7). This larger area and the ability to apply a more effective attracting electric potential increased the cross section of our detectors by more than an order of magnitude.

To address the second problem, we tried various methods of lowering the T_c of the detectors, including ion bombardment to introduce impurity scattering[55] and also by using thin layers of Ti/Au (~250-300 Å each) to use the proximity effect with normal metals to suppress the superconducting transition.[59] The ion bombardment had no effect on the transition temperature. Using the proximity effect, we managed to fabricate detector wires out of titanium/gold bilayers that had transition temperatures around 85 mK, but subsequent attempts to add ground planes to these devices made detectors that were not superconducting at 50 mK because the heating required to deposit the photoresist bilayer necessary to lay down the ground plane was enough to cause alloying between the thin Ti/Au layers.

During the initial creation of these detectors, the Bosch process was still used to cut holes through the wafer. (The holes were moved to between meanders.) Even-

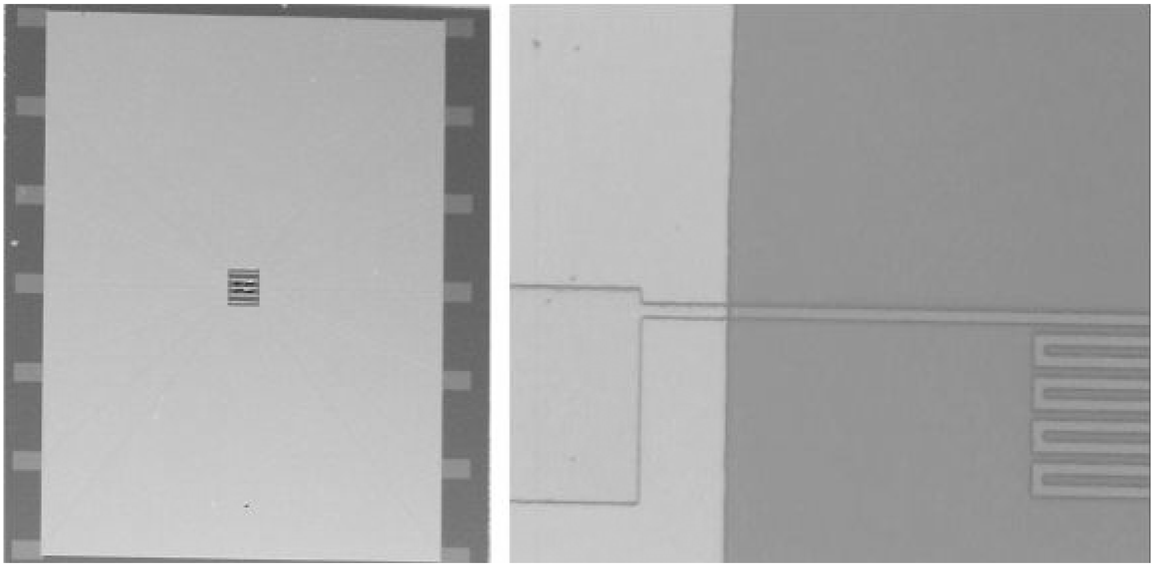

Figure 3.7: Second Detector Revision. The hole in the ground plane is 1 mm by 1 mm. The detectors are single wire meanders crossing back and forth across the hole 9 times, with a 1 μm gap between each meander, for a total detector width of 17 μm. There are 5 detectors per die in this design. The image on the right shows a zoom view of one end of the meander pattern.

tually we started using an ultrasonic grinder to drill these holes at UCSD, as the Bosch process took a considerable amount of time.

Fabrication Details

The fabrication of the second revision detector was much the same as the first revision. The only difference was the stage of completion of various dies, and switching the process used to drill the holes through the wafer.

3.3.3 Third Revision

In 2005, we moved the majority of our microfabrication efforts from UCSB to UCSD. This forced us to change the masks being used to make our detectors, as the nano3 facility does not have a stepper. This third detector design is in large part similar to the second revision. The only major functional difference is that there is only one detector per die, rather than 5. The new design also called for the $\mathrm{SiN_x}$ layer to be deposited by PECVD rather than by sputtering, as the sputtered film has a high defect density due to the highly strained nature of the film, which causes the layer to eventually crack and allow direct contact between the detector and the ground plane.

We again tried to make detectors with lower transition temperatures, first by revisiting the proximity effect design and also by using controlled phase-mixing of tungsten in an attempt to make very precise temperature transitions.[37] For both of these techniques, partially completed samples consisting of only the detector wire itself showed promise, but subsequent processing required to complete the devices destroyed the effect we were attempting to achieve. We finally wound a superconducting magnet around a heat shield to control the T_c of our detectors.

It should be noted here that the current microfabrication steps for the detector do not work: the PECVD step requires temperatures around 350 °C to be maintained for upward of one and a half hours, and during that time, even the thick Ti/Au layers alloy. Ideas for overcoming this limitation will be discussed in Chapter 6.

Fabrication Details[4]

This fabrication was done at the nano3 clean room at UCSD, and is specific to the third detector revision. The previous detector revisions were similar in microfabrication.

1. Clean a 100 mm wafer in the standard fashion.
2. Deposit a 125 nm layer of SiN_x by PECVD.
3. Spin, expose, and develop a thin layer of S1805 as a positive resist. The pattern exposed is the detector leads and the detector itself.
4. Deposit 50 nm of Ti followed by 25 nm of Au in an ebeam evaporator, without breaking vacuum.
5. Lift off the photoresist using acetone.
6. Deposit an additional 750 nm of SiN_x by PECVD.
7. Spin, expose, and develop a resist bilayer using PMGI SF-11 and S1805. The pattern exposed is the ground plane.
8. Deposit 10 nm of Ti followed by 100-150 nm of Au. Either evaporation or sputtering will do. Additionally, a 10 nm layer of Cr can be substituted for the Ti.
9. Lift off the photoresist using PG Remover.
10. On the back of the wafer, deposit 10 nm of Ti followed by 100-150 nm of Au by sputtering.
11. Spin a layer of S1805 to protect the wafer for subsequent mechanical processing.
12. Dice the wafer.
13. Glue the individual dies to a glass slide using crystalbond.

---

[4] Standard microfabrication steps are discussed in Appendix B.

14. Drill the holes by ultrasonic grinding.

15. Soak the individual dies in acetone to remove the photoresist and crystalbond.

16. For each individual die, perform an O_2 descum process to remove the HDMS used as a wetting agent for the S1805.

17. For each individual die, etch back the exposed SiN_x by RIE to expose both the detector and the leads. The Au will act as a mask to protect the SiN_x used to insulate the ground plane.

3.3.4 Support Electronics

Measurement of the detector resistance is done by using a battery current source and measuring the voltage in a four wire configuration. The entire measurement system can be floated to $\pm 5\,\mathrm{V}$. See Figure 3.8 for the details. This technique was always used to determine T_c for the detectors.

For later experiments we changed to a faster amplifier circuit to measure electron impacts by voltage bias instead of current bias.[33] This technique is traditionally done using SQuIDS for current measurement, but we adapted it to an op-amp circuit that measured the change in voltage across the circuit by capacitively coupling to the amplifier stages. This circuit is diagramed in Figure 3.9.

3.4 Electrodes

For these experiments, two types of electrodes were fabricated. The first was a series of nanoscale posts, the second was a single hole in a ground plane with an electrode underneath.

3.4.1 Nanoscale Posts[5]

Most experiments for probing the properties of electrons on helium have been done using simple geometries: a large guard ring to confine electrons radially, and a

---

[5] A more detailed discussion of the nanoscale posts can be found in ref.[45]

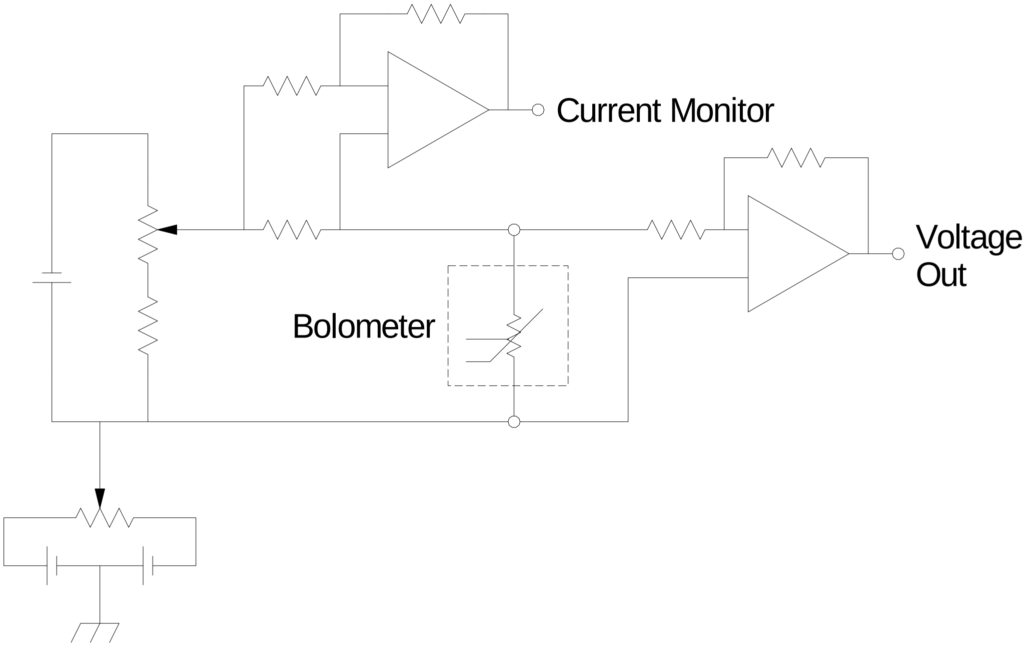

Figure 3.8: Electronics used to measure detector resistance. Typical applied current is ∼1 μA. The entire circuit can be floated in order to bias the detector positive to make detection more likely by both attracting the electrons and making them more energetic.

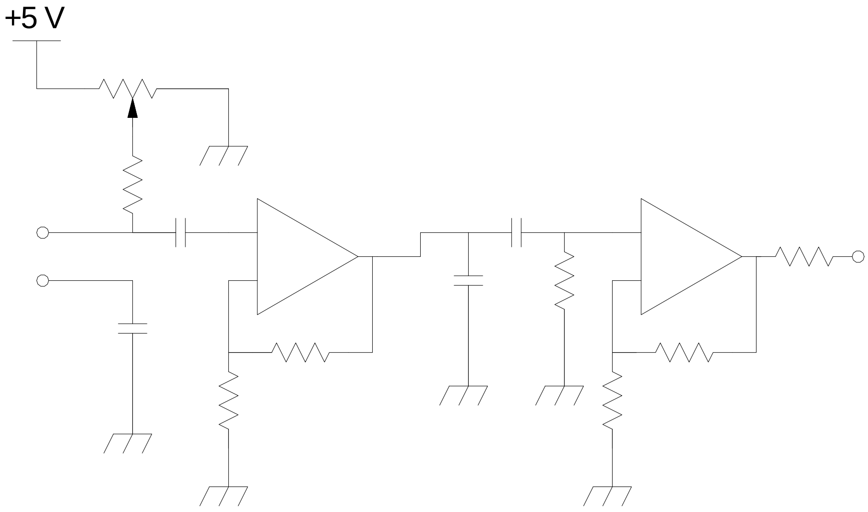

Figure 3.9: Voltage bias system for faster detector measurements. Both op-amp stages have a gain of roughly 20. There is an addition high pass filter applied between the two amplification stages with a cutoff frequency of 100 kHz. The detector is connected between the two terminals on the right, and the output is connected to an osciliscope.

small pressing field applied by capacitor plates underneath and above the helium to make sure the electrons stay bound to the surface.[54] More recently, Mike Lea and his group have been working with trenches to confine the electrons to even smaller geometries, and even make simple FETs with the electron layer as the channel.[21] In each case, though, the electrode geometry is simple, and provides for poor in-plane single electron confinement.

At the beginning of this work, we knew this would be the biggest challenge—creating a set of electrodes that would allow both for the independent addressing of individual electrons and for spatial confinement of electrons while still holding them close enough together on the surface to allow for 2 qubit operations. Hence the idea of the post electrodes.

The individual posts on these electrodes are 1.5 μm tall and 200 nm in diameter, in an array 10 long and 2 wide separated by 0.5 μm. They are made by plating gold into holes drilled in PMMA via e-beam lithography. The height of the posts is measured by measuring the change of mass of a witness piece of known area. Samples

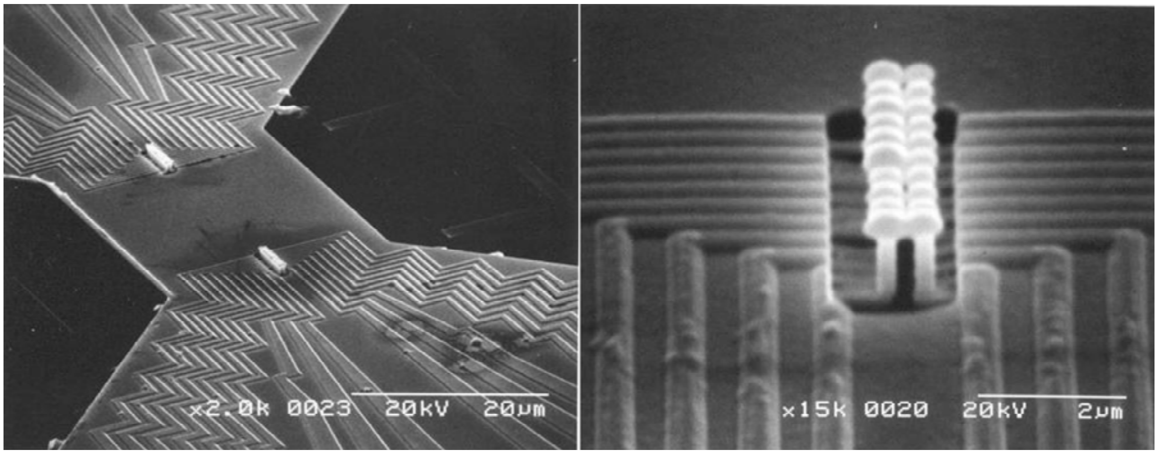

Figure 3.10: SEM images of posts. The posts appear as mushroom caps due to over plating. The right image shows a zoom view of the right-hand set of posts in the left image.

of post plating can be seen in Figure 3.10.

In addition, we wanted to know the height of the helium film above the posts. To this end, we fabricated in-plane capacitors in the unused portion of the ground plane.

Fabrication details[6]

This fabrication was done at the clean room at UCSB.

1. Clean a 100 mm wafer in the standard fashion.
2. Deposit $2\,\mu$m of SiO_2 followed by $0.5\,\mu$m of SiN_x by PECVD.
3. Spin, bake, and pattern a layer of AZ 5214 as a negative photoresist to deposit the photo leads for the post electrodes.
4. Deposit Ti/Au by e-beam evaporation for the photo leads and in-plane capacitor.
5. Liftoff the photoresist.

---

[6] Standard microfabrication steps are discussed in Appendix B.

6. Spin, bake, and pattern a layer of EPA 520A e-beam resist for depositing the fine-detail leads for the post electrodes. Alignment is done by use of alignment marks left behind by the previous photolithography step.

7. Deposit Ti/Au by e-beam evaporation for the photo leads.

8. Lift off the e-beam resist. At this point, the leads and in-plane capacitor are complete.

9. Deposit $0.4\,\mu$m of $\mathrm{SiN_x}$ by PECVD.

10. Spin, bake, and pattern a layer of Alf 2020 as a negative photoresist to deposit the ground plane.

11. Deposit Ti/Au by e-beam evaporation.

12. Liftoff the photoresist.

13. Etch back the $\mathrm{SiN_x}$ by RIE. The ground plane acts as a mask to the etch. It is desirable to slightly over-etch this process to remove any residual $\mathrm{SiN_x}$ left over the e-beam leads. Monitor the etch using a laser interferometer.

14. Spin and bake the resist (PMMA) for electroplating the posts.

15. Expose the posts. The dosage for this exposure is $1200\,\mu\mathrm{C/cm^2}$when a 50 keV e-beam writer is used. This dosage is optimized for for posts separated by $\sim 0.5\,\mu$m and yields holes about 200 nm in diameter.

16. Dice the wafer.

17. Develop the individual dies in $1 : 3 :: \mathrm{MIBK} : \mathrm{IPA}$. Due to the aspect ratio of the holes, the development was done in an ultrasonic bath, and for five minutes.

18. Plate Au into the holes onto the e-beam leads. We used a sulfate-based bath for this process; although, a cyanide bath could also be used. The height of the posts is determined by plating a witness piece at the same time and measuring the accumulated mass using a micro balance. The plating time is the control variable for either slightly over-plated or under-plated posts.

19. Redice the wafer to remove the shorting gold barrier.

20. Liftoff the PMMA using acetone, and no ultrasound.

Helium height control over posts

The in-plane capacitors turned out to be a disappointment, and unsuitable to the task of measuring helium film thickness for film thicknesses less than ∼1-2 μm, probably due to the high dielectric constant of Si, and the comparatively low dielectric constant of liquid helium. To solve this problem, a post wafer was re-coated with a 1.5 μm layer of PMMA, into which we patterned a set of walls around the post micro structure. These were deposited using the gold sulfate plating bath. The result was a trench 1.5 μm deep and 10 μm wide around the post micro structure, which would fill with superfluid helium due to capillary forces. Unfortunately, the wafer itself did not survive this process; the leads to the post micro structure were shorted to the ground plane after it was completed. A picture of the completed trench can be seen in Figure 3.11

$\omega_\parallel$, E_z for Nanoscale Post Electrodes

Since the point we are interested in the electric field at is farther away from the post than the diameter of the top, a simple approximation is to assume the electrode is spherical. Under that assumption, the potential felt by the electron due to both its image charge and the applied voltage on the surface can be written as

$$\Phi(\mathbf{x}) = \frac{e}{4\pi\epsilon_0}\frac{a}{x^2 - a^2} + \frac{Va}{|\mathbf{x}|}, \tag{3.4}$$

where $\mathbf{x}$ is the position of the electron with respect to the center of the top of the post, a is the radius of the post, and V is the voltage applied to the post. If we decompose $\mathbf{x} = r\hat{\mathbf{r}} + z\hat{\mathbf{z}}$, and note that $z^2 - a^2 \gg r$, then we can expand this to

$$\Phi\left(r, z\right) = \frac{e}{4\pi\epsilon_0}\frac{a}{z^2 - a^2}\left(1 - \frac{r^2}{a^2 - z^2}\right) + \frac{Va}{z}\left(1 - \frac{1}{2}\frac{r^2}{z^2}\right) \tag{3.5}$$

From this, we can extract E_z,

$$E_z(r = 0, z) = \frac{e}{\pi\epsilon_0}\frac{2az}{\left(z^2 - a^2\right)^2} + \frac{Va}{z^2}, \tag{3.6}$$

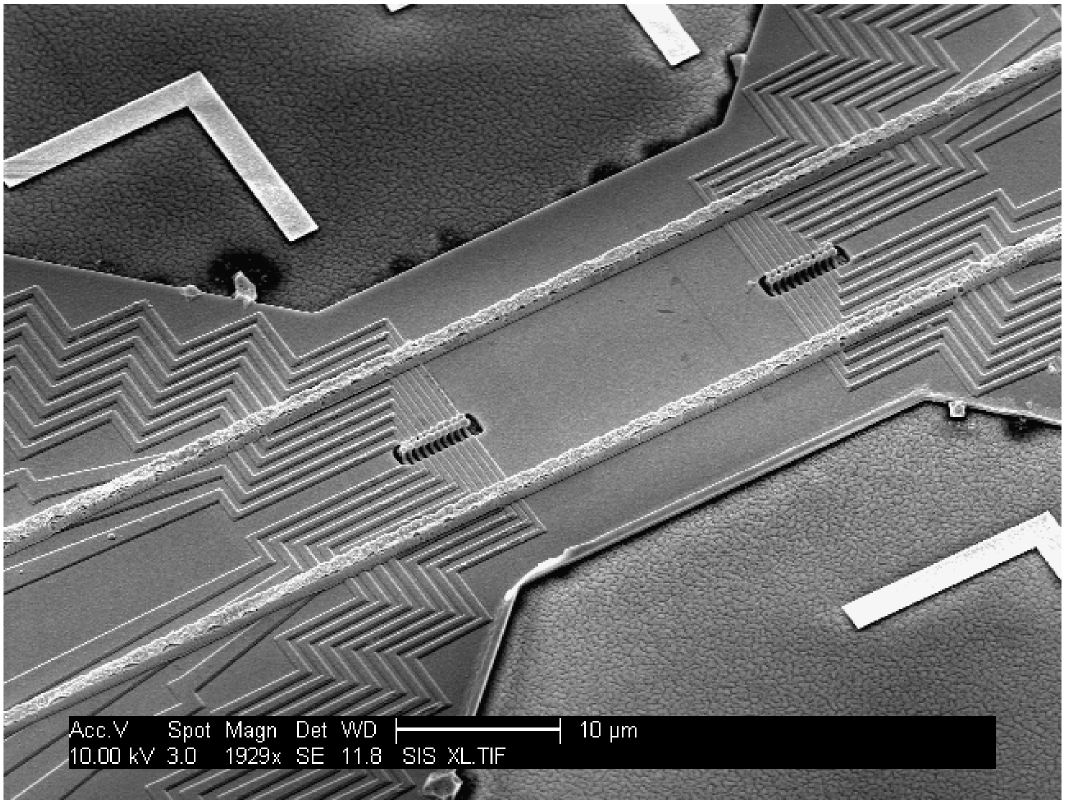

Figure 3.11: Helium film height controlling trench. The trench is 10 μm wide and 1.5 μm deep around the post micro structure.

and U_r, as

$$U_r(r,z) = \frac{e^2}{4\pi\epsilon_0}\frac{a}{\left(z^2-a^2\right)^2}r^2 + \frac{eVa}{2z^3}r^2 \tag{3.7}$$

From this, we can read out the harmonic oscillator frequency for the radial potential:

$$\omega_{\parallel}^2 = \frac{e^2}{2\pi\epsilon_0 m_e}\frac{a}{\left(z^2-a^2\right)^2} + \frac{Vea}{m_e z^3} \tag{3.8}$$

3.4.2 Helium Pool

Unfortunately, we had a problem with the nanoscale posts: specifically, they degraded in time, and we ended up with all of our electrodes shorted to the groundplanes on all of our fabricated dies over the course of two years. We set out in search of an easier electrode to fabricate for the initial experiments. Our basic requirements were:

- A place for helium to be bound by capillary forces.
- An electrode covered by a ground plane to prevent crosstalk.
- Able to take the exact place in our sample cell that the post chip would sit.
- Easy to fabricate.

We were specifically not interested in attempting to confine two separately controllable pools; just a testbed to do one-qubit experiments.

We designed a simple wafer to solve these problems: a single electrode exposed through a 10 μm hole in a ground plane. The 10 μm hole is small enough that the variation in height of a capillary film is small. In addition, solutions for the electric field for a single hole in a conducting plane are well known.[27] The basic wafer geometry can be seen in figure 3.12

Fabrication Details[7]

1. Clean a 100 mm wafer in the standard fashion.

---

[7] Standard microfabrication steps are discussed in Appendix B.

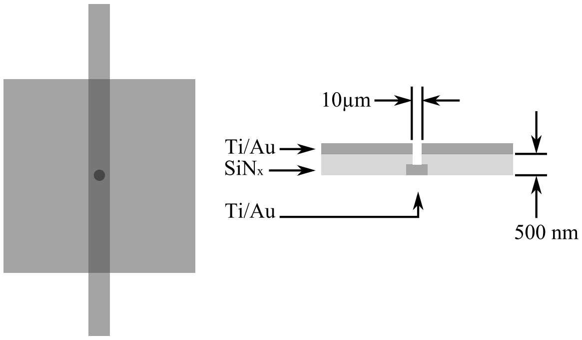

Figure 3.12: Helium Pool geometry. The electrode is exposed by a 10 μm diameter hole in the ground plane.

2. Deposit 125 nm of low stress $\mathrm{SiN_x}$ by PECVD.
3. Spin, develop and expose AZ 5214e as a negative resist. The pattern exposed is the electrode behind the ground plane.
4. Deposit 10 nm of Ti followed by 100 nm of Au by either sputtering or evaporation.
5. Lift off the photoresist using acetone.
6. Deposit 500 nm of low stress $\mathrm{SiN_x}$ by PECVD.
7. Spin, develop and expose AZ 5214e as a negative resist. The pattern exposed is the ground plane.
8. Deposit 10 nm of Ti followed by 100 nm of Au by either sputtering or evaporation.
9. Lift off the photoresist using acetone.
10. Dice the wafer.
11. For each individual die, etch back the exposed $\mathrm{SiN_x}$ by RIE to expose the electrode. The ground plane acts as a mask to prevent etching of the $\mathrm{SiN_x}$ used as an insulator between the ground plane and the electrodes.

$\omega_{\parallel}$, E_z for Helium Pool Electrode

The tangential electric field for a hole in a ground plane takes the form

$$\mathbf{E}_{\text{tan}}(\mathbf{r},0) = \frac{E_{\text{above}} - E_{\text{below}}}{\pi} \frac{\mathbf{r}}{\sqrt{a^2 - r^2}} \tag{3.9}$$

where a is the radius of the hole, E_{above} is what the electric field above the hole would be in its absence, and E_{below} is what the electric field below the hole would be in its absence.[27]

The perpendicular electric field inside the hole is simply the average of E_{above} and E_{below}.

Taking equation 3.9, we can derive an expression for the radial confinement potential. Specifically, we get:

$$U_r(\rho) = -e\frac{E_{above} - E_{below}}{\pi a}\left(\frac{1}{\sqrt{1-\rho^2}} - \frac{\rho^2}{(1-\rho^2)^{3/2}}\right) \tag{3.10}$$

where $\rho = \frac{r}{a}$. This provides a very strong confinement to the pool area. For small displacements from the center of the pool, we can take a Taylor Series for an approximate potential:

$$U_r(\rho) \simeq -e\frac{E_{above} - E_{below}}{\pi a}\left(1 + \frac{3}{2}\rho^2 + O(\rho^4)\right). \tag{3.11}$$

From this, we can read the frequency of the harmonic oscillator potential:

$$\omega_{\parallel}^2 = 3e\frac{E_{above} - E_{below}}{\pi a^3 m_e}. \tag{3.12}$$

Electron Pool Size

It is well known from earlier work that electrons will stick to a helium surface; the hard part is getting either getting them not to, or getting an extremely large density without pushing electrons through the film. The highest measured surface density of electrons is on the order of $10^8\,\text{cm}^{-1}$.[61] For this work, we want a small charge pool—eventually only one electron.

Previous calculations performed in this lab indicate that the charge density of a layer of electrons on a helium surface is virtually constant until one reaches the boundary, where it drops off quickly.[54] So, to first order, the charge pool behaves as a two dimensional conductor with uniform charge distribution. We can then calculate the expected radius of a charge pool of given charge at zero temperature easily — all we have to do is calculate the capacitance of the pool to the electrode, and back calculate the expected radius.

$$r_e = \sqrt{\frac{nh_p e}{2\pi\epsilon\epsilon_0}\frac{1}{V_g - V_p}}, \tag{3.13}$$

where n is the number of electrons in the pool, h_p is the thickness of the helium layer, ϵ is the dielectric constant of helium, V_g is the voltage applied to the electrode, and V_p is the voltage of the pool. If we want the pool to be in equilibrium with the applied voltage on the ground plane (taken to be 0 for the rest of this section), we should set $V_p = 0$.

The next step is to calculate the expected potential energy wells using finite element methods[52] and find the height and thickness of the expected potential barrier. The expected radius of the pool, to first order, is the point where the potential energy well meets the thermal energy of the electrons. Figures 3.13 and 3.14 show the computation geometry and sample computations. Estimates of the quantum tunnelling rate are then calculated using the WKB approximation, assuming electrons hit this barrier at a rate of $\Gamma = v_e/2r_p$, with $nk_bT = 1/2mv_e^2$. Sample results from this computation are shown in Figure 3.15.

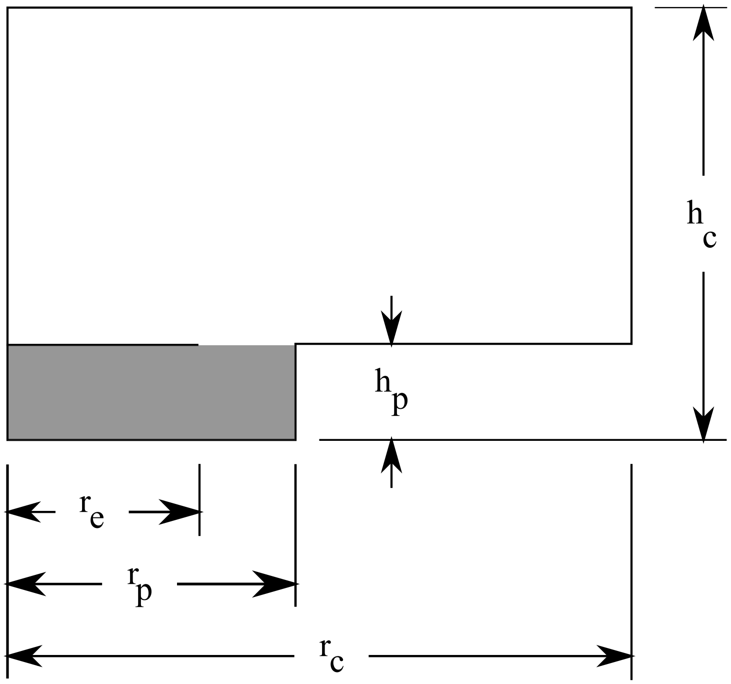

Figure 3.13: Geometry for calculating the stability of electrons on the helium pool electrode. The radius of the electron pool is r_e. The radius of the helium pool is $r_p = 5\,\mu$m. The radius of the sample area is $r_c = 1\,$mm. The thickness of the helium pool is $h_p = 500\,$nm. The height of the sample area is $h_c = 1\,$mm. A voltage V_g (typically in the range of .1 mV to 1 mV) is applied at the base of the helium pool. A pressing field V_{pr} (typically -1 V to -3 V) is applied at the top of the sample area.

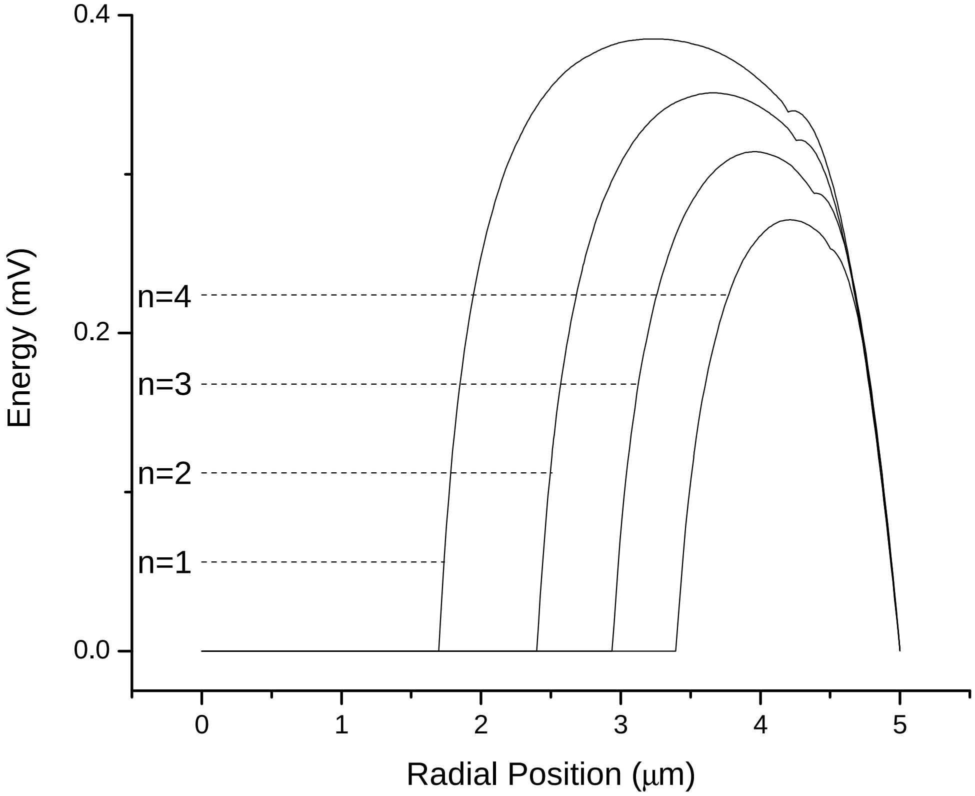

Figure 3.14: Sample finite element calculations for electron pool stability. The potential barrier is shown for various numbers of electrons in the pool with $V_g = -0.5\,\mathrm{mV}$, and $V_{pr} = -2\,\mathrm{V}$. The expected kinetic energy stored in each pool is shown as a dashed line out to the classical turning point.

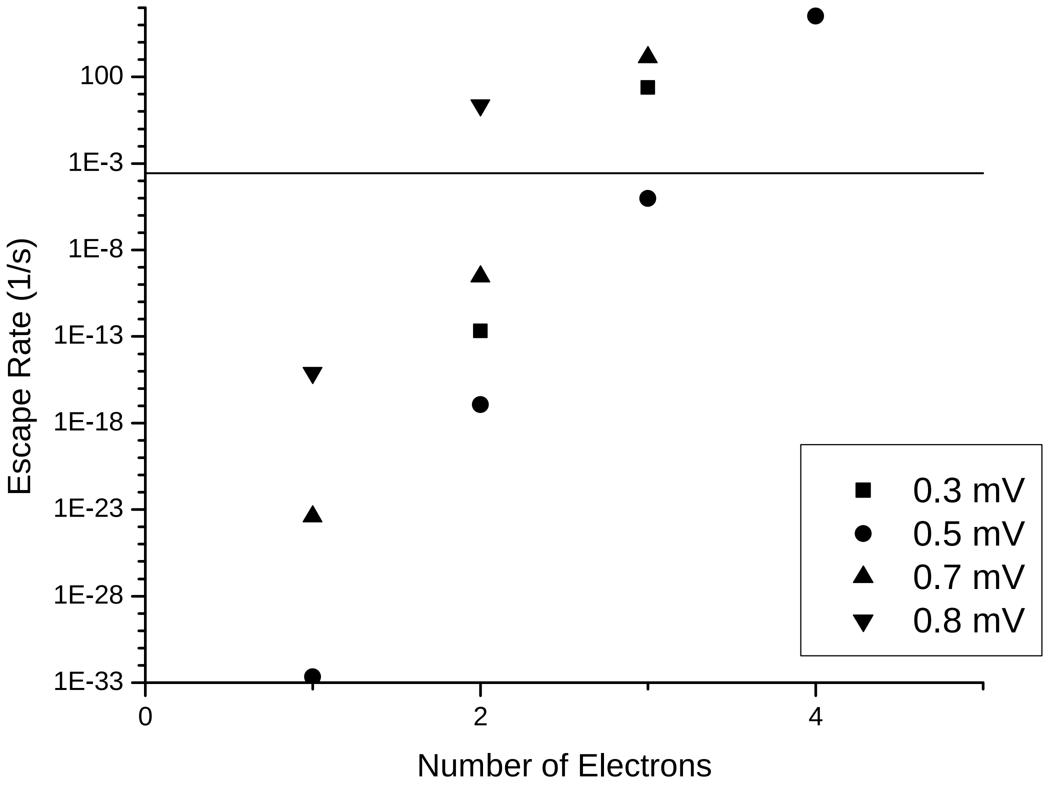

Figure 3.15: Sample escape rates for electrons confined on the pool. The pressing voltage is set to -3 V, and the temperature of the electrons is taken to be 650 mK. The different symbols represent different values of V_g. The line across the graph is drawn at 1 hour stability time—the time required to cool the system from 650 mK, required to deposit electrons on the pool, to 300 mK, required to perform bolometric measurements.

Chapter 4

Experimental Apparatus

4.1 Introduction

This chapter describes the experimental equipment used and prepared for this project.

4.2 Cryostat

Two different experimental factors require mK temperatures for this work: 1. our detectors have a superconducting transition of ~300 mK, and 2. the decoherence time of our qubit design goes as T^{-3}.[15] Including the additional requirement of continuous refrigeration to make long term experiments possible, the best cooling system available for this particular experiment is a dilution refrigerator. We used a laboratory built and designed cryostat centered around an Oxford Instruments 200s dilution unit. The three cooling stages used in this cryostat are all quite standard. First, the entire cryostat is immersed in liquid helium inside a super-insulated dewar, cooling the cryostat to 4.2 K. The final two cooling stages are isolated from the helium bath by a vacuum can, which is pumped to a pressure $\leq 10^-5$ mm Hg. Next, a small volume of liquid helium is evaporated by continuous pumping. As the vapor pressure above the liquid helium goes down, the ^{4}He pot cools down to approximately 1.2 K. This reservoir is continuously refilled from the bath via a high impedance capillary.

Finally, the ^{3}He/^{4}He dilution effect is used to cool the system to anywhere between 50 mK and 1.2 K, depending on at what temperature the current experiments are being conducted at. The ^{3}He/^{4}He mixture for the dilution refrigerator is precooled via a pair of coiled heat exchangers, one mounted in the liquid He bath and one on the ^{4}He pot. In order to improve the isolation of the dilution unit, heat shields are mounted both at the still and between the continuous heat exchangers and the discreet heat exchangers. At 100 mK, the system is capable of dissipating 200 μW. The sample cell is thermally shorted to the mixing chamber by a length of 15 AWG copper wire. The cryostat used for these experiments is diagrammed in Figure 4.1.

4.2.1 Vibration Isolation

The cryostat is fixed to an aluminum plate that is separated from a welded steel frame by layers of neoprene and rubber to dampen the influence of ground vibrations from the cryostat. Each pumping line has a section of flexible bellow in the line to prevent the mechanical vibrations of the pumps used to run the dilution refrigerator and the ^{4}He pot from affecting cryostat operations as well.

4.2.2 Wiring

The wiring between room temperature and 4.2 K used to monitor and control all components of the system is 38 AWG copper wire with Teflon insulation down to the vacuum can. From room temperature down to 4 K, the electrical conductivity to thermal conductivity ratio of copper is the highest for easily available wire, and the helium boil off rate is kept small by using small gauge wire. Inside the vacuum can, a niobium/titanium alloy wire with a superconducting transition of 9.8 K is used because thermal isolation between different cooling stages becomes more important. (Superconducting metals become very poor thermal conductors in the superconducting state.) A short length of copper capillary is crimped on the end of the Nb/Ti wire to facilitate soldering, as Nb/Ti does not take lead/tin solder with any easily available flux.

Two types of leads were installed for controlling and monitoring experiments.

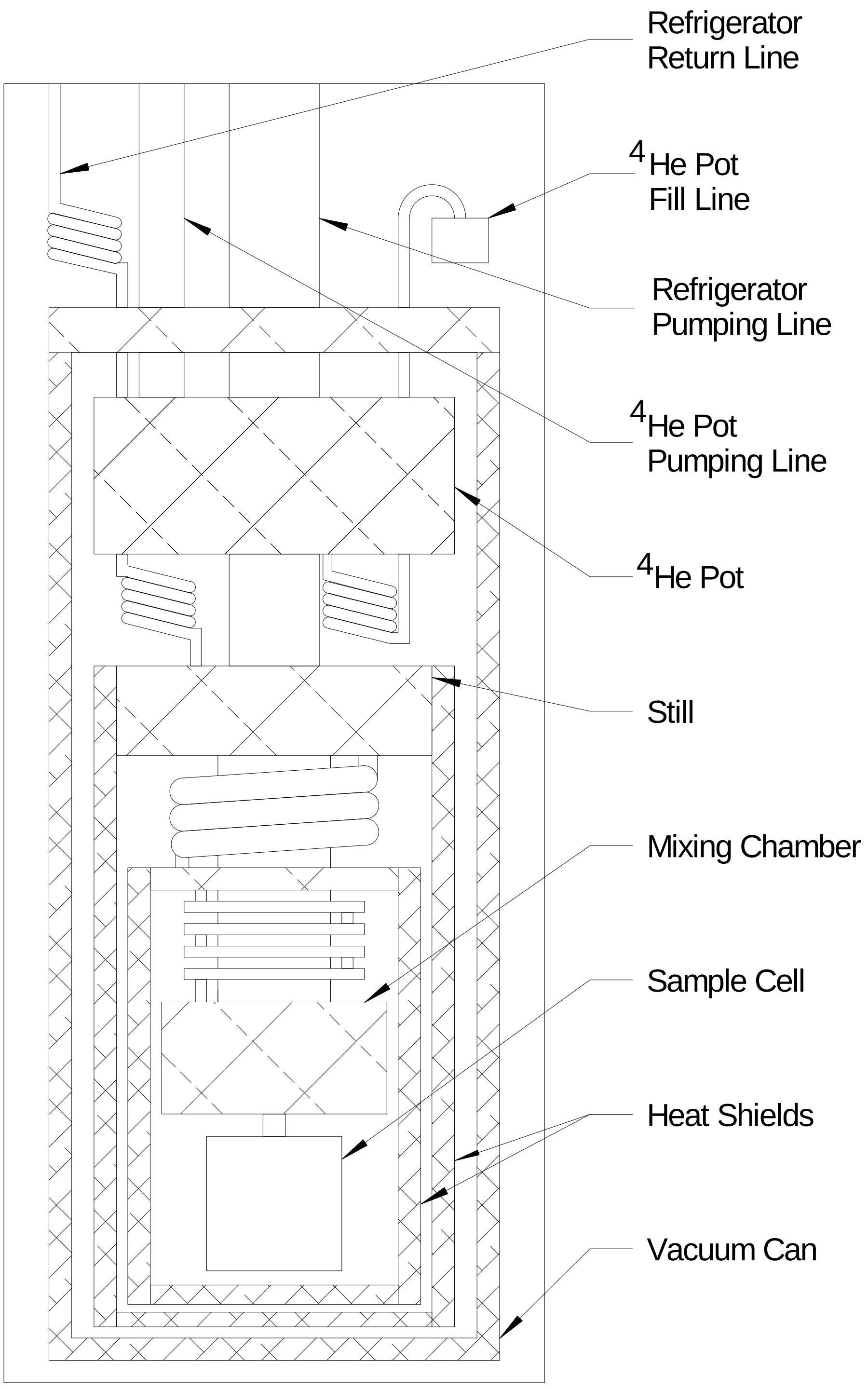

Figure 4.1: Schematic of the Cryostat. Inside the vacuum can the cooling stages are a ^{4}He pot and an Oxford Instruments 200s dilution unit. Heat shields are mounted on the still and between the continuous heat exchanger and the discrete heat exchangers.

Twisted pairs were made and installed from room temperature down to the vacuum can, where $50\,\Omega$ termination was installed for impedance matching for electronics at room temperature. The twisted pairs between room temperature and 4.2 K were made from 38 AWG copper wire with Teflon insulation. Inside the vacuum can, the twisted pairs continue, but the wire used is again the superconducting niobium/titanium wire. These leads terminate at a wiring socket attached to the mixing chamber. The second type of experimental leads are coaxial. These cables are stainless steel inner and outer conductor cables with Teflon insulation purchased from Lakeshore Cryogenics. The resistance of the cable (from dewar head to sample chamber) is $\sim 75\,\Omega$. These cables are not terminated at the vacuum can, since the cable resistance is already much higher than the termination resistance would be.

4.2.3 Liquid He level detection, Thermometry, and Temperature Control

The temperature of the liquid helium bath is monitored by a diode thermometer mounted at the bottom of the dewar. This allows the presence of liquid helium (or nitrogen, during cooldown procedures) to be detected. A standard helium level indicator is used to insure that liquid helium levels stay above the inlet to the ^{4}He pot.

In order to diagnose the operation of the cooling stages, carbon resistance thermometers are mounted at various points inside the vacuum can: the ^{4}He pot, the still, the coldplate, between sets of heat exchangers, and on the mixing chamber. The carbon resistors are set up as 2 wire probes feeding into a lab-built Wheatstone bridge, where the resistance is measured by balancing the bridge using a precision decade resistance box and a Princeton Applied Research model 5209 lock-in amplifier. A calibrated germanium resistor is mounted directly on the sample cell in order to monitor the temperature of the experiment, and is wired via a four terminal network back to the Wheatstone bridge used for the carbon resistors.

The heaters in this cryostat are made by wrapping a short length of mangnin wire around copper forms, and have a typical resistance of $250\,\Omega$. There are heaters

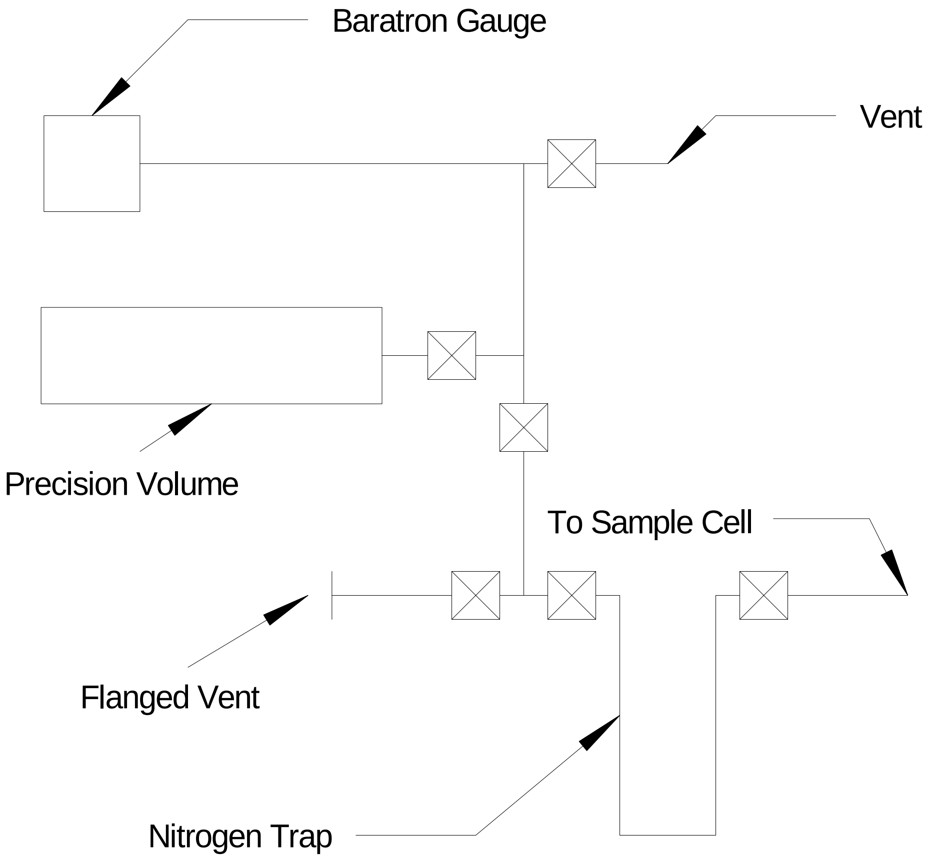

Figure 4.2: Sample cell filling system. The volume used is 2.000 l ± 5 ml. The valves used are bellow valves. The pressure gauge is a baratron pressure gauge.

mounted on the sample chamber, the mixing chamber, and the still. The temperature is controlled with a lab designed and built PID feedback controller, using the output of the lockin used for temperature measurement as the control signal for a negative feedback loop used to control the current passing through the heater mounted on the sample cell. Attempts were made to use the detector transition directly as the source of the feedback signal, but proved to be unstable in the necessary temperature range.

4.2.4 Sample Cell Filling

In order to accurately gauge the amount of liquid helium added to the sample cell, a precision 2.000 l volume was installed such that the sample cell fill capillary could be opened to it by a set of bellow valves. A baratron pressure gauge was used to measure the pressure in the precision volume. Incremental amounts of gas from this volume were added to the sample cell by the manipulation of the valves. In order to figure out the amount of gas moved into the sample cell, the pressure in the precision volume was measured before and after some of the gas was moved to the sample cell. Helium is pulled into the cell by the cryopump effect. The sample cell filling system is diagrammed in Figure 4.2.

4.3 Microwaves

In order to cause Rabi oscillations in our qubits we need a source of 140 GHz, phase locked microwaves. The microwave source used is a mechanically tuned Gunn oscillator operating at 140 GHz, with a typical power output of 13 dBm. The phase lock loop is controlled by an XL Microwave model 800A Gunn phase lock module, which is slaved to a 10 MHz oven stabilized crystal time base. This module requires an intermediate frequency of 50 MHz, which must be extracted via mixing an intermediate frequency with the Gunn oscillator output. A 10 dB coupler is used to split the 140 GHz between the main waveguide line into the cryostat and the harmonic mixer. The other signal fed into the harmonic mixer is a 15.55 GHz signal produced by a CTI DRS-1409 synthesizer, also slaved to the 10 MHz timebase used by the Gunn phase lock module. The 50 MHz signal is generated as the beat frequency between the 9th harmonic of the 15.55 GHz signal (139.95 GHz), and the 140 GHz from the Gunn oscillator. A diplexer is used to separate the 50 MHz signal from the signal returning from the mixer, and this 50 MHz signal is then amplified and fed into the phase control module. The microwave phase lock system is diagrammed in Figure 4.3. The limiting factor in this phase control scheme is the oven stabilized crystal oscillator, which has a phase stability of around 1 part in 10^{10}.

To insure phase coherence from one operation to the next, a PIN diode is placed between the microwave system output and the cryostat so the Gunn oscillator can be left running during computer operations. The PIN diode allows an 80 dB attenuation to be turned on or off, either allowing microwaves into the system or

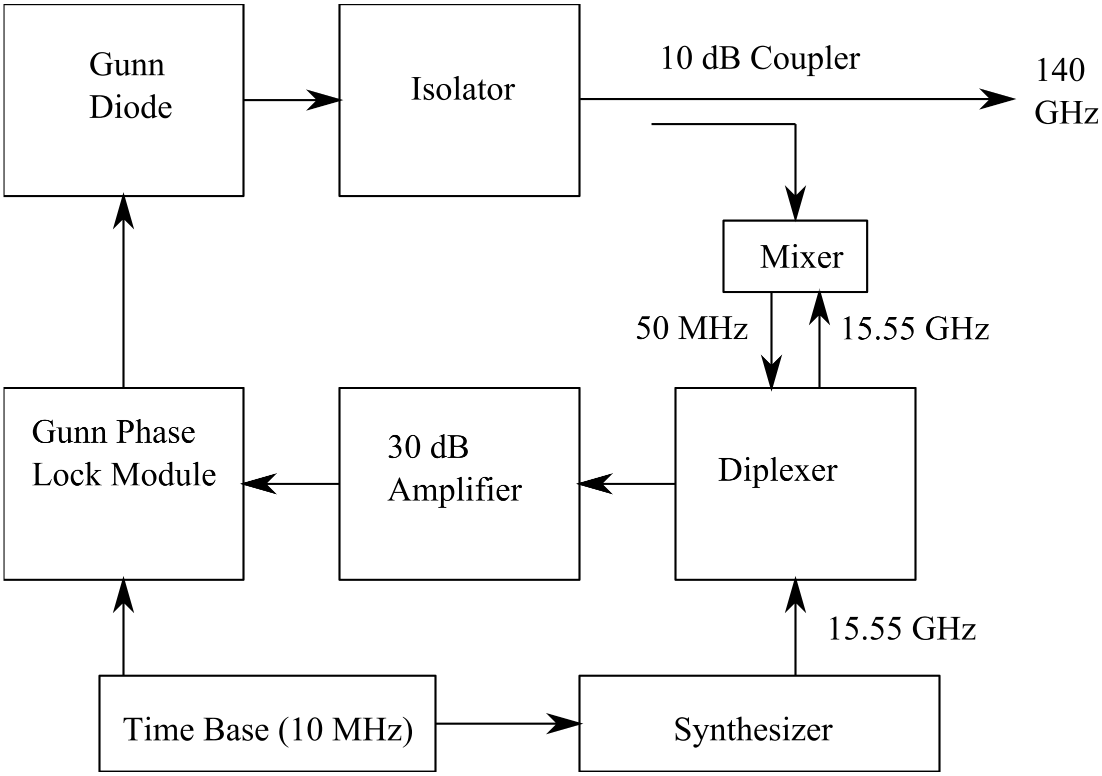

Figure 4.3: Microwave system phase lock look setup. The Gunn diode is a mechanically tuned Gunn oscillator operating at 140 GHz. The phase lock control module is an XL Microwave Model 800A Gunn phase lock module. The time base is a 10 MHz oven stabilized oscillator. The synthesiser is a computer controlled CTI DRS-1409 operating at 15.55 GHz.

suppressing them depending on the diode's state. For computer operations lasting upward of a millisecond, two such PIN diodes would be required.

The waveguide used to transmit the microwaves from the Gunn oscillator to the sample chamber is WR-8 (2 mm by 1 mm internal dimension) waveguide, made of either coined silver, in places we don't care about thermal conductivity, or stainless steel, in places we do. 140 GHz is transmitted in the TE_{10} mode for this particular waveguide size. The assembled waveguide consists of 27 inches of coin silver and 41 inches of stainless steel, with an additional 2 right angle bends made of coin silver. The estimated attenuation of the entire waveguide setup is about 60 dB, mainly due to losses in the stainless steel sections of waveguide. Attempts to measure the microwave power passing through the entire waveguide setup indicated the throughput was less than 1 μW, the lowest power our microwave detector can measure. The expected Rabi frequency of our qubits due to microwaves at -47 dBm is about 2.0 MHz.

4.4 Microwave Sample Cell

A sample cell appropriate for use with the microwave system has been designed and constructed. (See Figure 4.4.) The main body of the cell is constructed out of OFHC copper. A coin silver waveguide goes through the middle of the cell, and has slots precision ground in it to accept a detector and an electron confining electrode. The waveguide has also had GE varnish applied as an insulating layer to prevent the microfabricated devices from shorting to sample cell ground. The detector and electron confining electrode are mounted on stycast 2850 blocks, which are pushed by springs so that the microfabricated devices sit flush with the interior of the waveguide. A tungsten filament electron source is installed in the sample cell above the detector, and there is space in the top of the cell for a PS diode. Indium o-rings are used to seal the sample cells copper to copper flanges. .005 in thick mylar seals are used for the waveguide couplings. Wire feed-throughs are made by threading 38 AWG formvar-insulated copper wire through holes drilled in the sample cell, which are then filled with stycast 2850.

In addition, a new technique for making large wire density feed-throughs ($\sim$

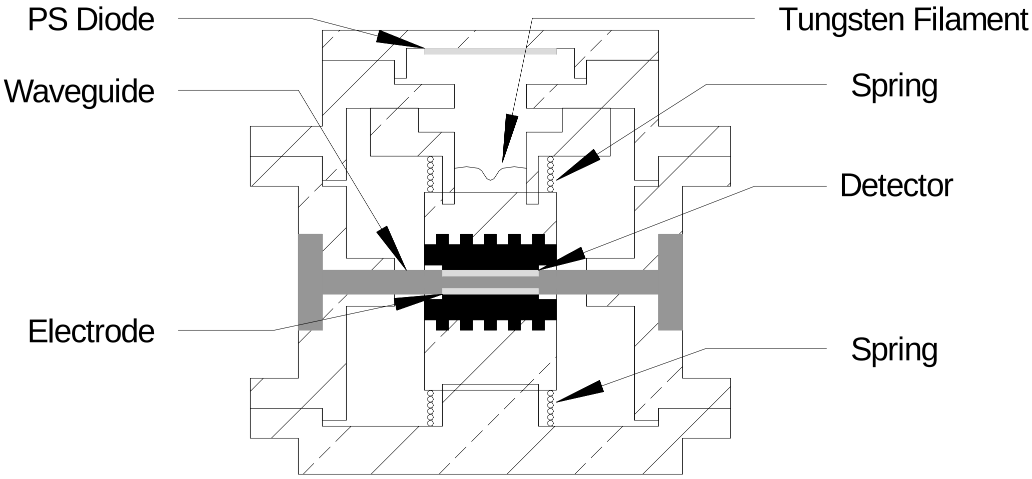

Figure 4.4: Microwave sample cell cross section.

$20\,\mathrm{cm}^{-2}$) was developed. First, a bundle of copper capillaries is soldered together inside a length of 0.25 in OD brass tubing, which is in turn soldered into the sample cell. Next, individual wires are threaded through the copper capillaries. Finally, stycast 2850 is pulled into the capillaries around the wires using house vacuum, and is cured in an oven at 60 °C for an hour. The only drawback to this technique is that the surface area of the feed-through is difficult to estimate, making it difficult to know what the saturated film thickness of superfluid helium will be inside the cell for a given amount of helium put in.

Chapter 5

Experiments

5.1 Introduction

This chapter details the experiments performed using the microfabricated elements detailed in Chapter 3, including early detector testing and electron capture experiments.

5.2 Detector testing

In order to test the detectors, a PS diode was aimed such that the emitted electrons would strike the detector. The number of electrons coming off the diode was interpolated from the data taken for reference [44]. The geometry used for testing detector revisions 1 and 2 is shown in Figure 5.1.

5.2.1 Detector sensitivity, Revision 1

The first revision detector tests were performed using an aluminum detector at 1.2 K. The diode bias was set to 80 V, which yielded an expected flux of 1 to 2 electrons per 400 μm^2 (the area of the ground plane opening in the first revision detector design), and a detector bias of 2 V. The diode was fired with a frequency of $\sim 1\,\text{Hz}$, and a pulse width of 4 ms.

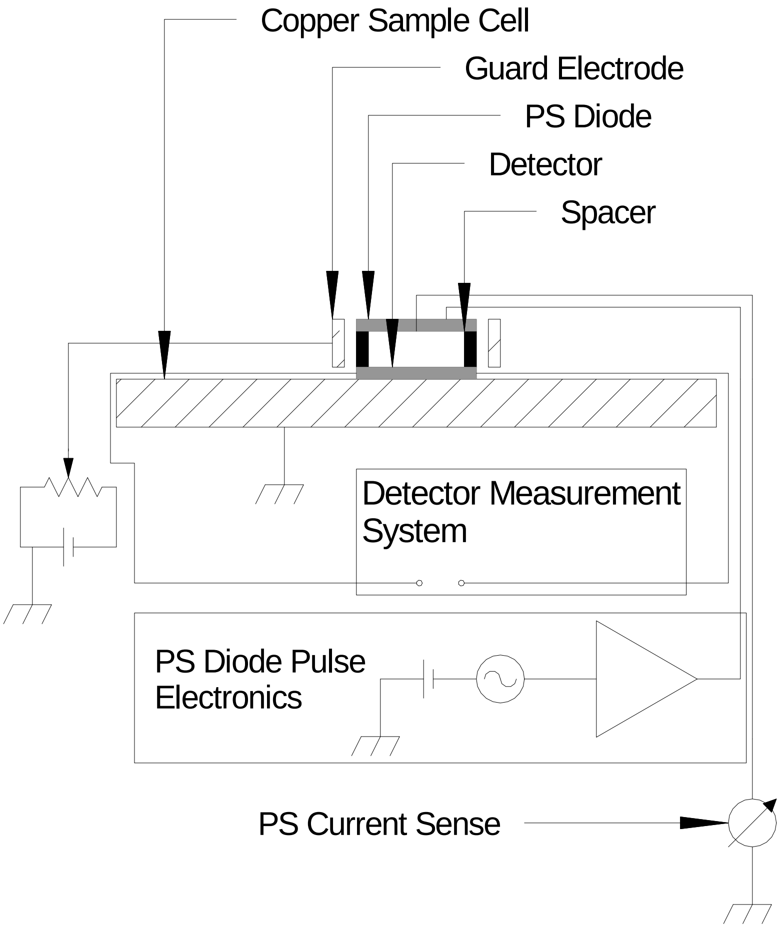

Figure 5.1: Detector test sample cell configuration. The detector is placed directly facing a PS diode. A guard ring electrode is used to focus the output of the PS diode. The electron flux is controlled by the diode bias voltage.[44]

The results of these experiments are shown in Figure 5.2. Detection events occurred roughly once every three pulses. The change of resistance for each event was identical; however, the amount of time the resistance stayed higher changed. The width parameter was obtained by calculating the integral underneath the pulse shape. It is difficult to state, based on this data, if we are seeing more than one electron per event, one electron per event, or if the width of the pulse is based on the number of electrons per event and their distribution of impacts around the wire.

5.2.2 Detector Sensitivity, Revision 2

The second revision detectors had a much larger surface area per detector than the first revision ones: $10\,\mu\text{m}^2$ for the first revision, and $\sim 1.7 \times 10^4\,\mu\text{m}^2$ for the second revision. As a result, we were able to reduce the diode bias voltage to 15-28 V, and work with a more well defined number of electrons per detector than when working with the first revision detectors. In addition, the longer meander pattern had a much higher resistivity in the normal state, allowing a larger change of resistance from the superconducting state to the normal state. For these experiments, a small capacitor was placed in line after the amplification stage so that we see the AC resistance changes – the DC portion of the resistance decays due to the RC network ($RC \simeq 150\,\text{ms}$). Noise is removed by using a Bessel filter. Sample of data before and after the filtering is shown in Figure 5.3. For 15-20 V diode bias, we estimate a flux of 1-2 electrons per detector as the incoming electron flux. Using this diode bias, the output signal showed a single spike which decayed in the manner expected for the majority of pulses as the detector drifts through its transition temperature. The results for this set of experiments is shown in Figure 5.3. Additionally, we performed experiments at 28 V diode bias, for which the estimated flux of electrons is 4 per detector. Data for these experiments is shown in Figure 5.4. Again, the detector was allowed to drift through its transition temperature. While the detector was in its sensitive region, there was a 100% detection rate, but the nature of the detection was different than for the 15-20 V pulses: instead of simple decay signatures, the signal underwent another jump and increased slowly back to 0 V, as expected for a

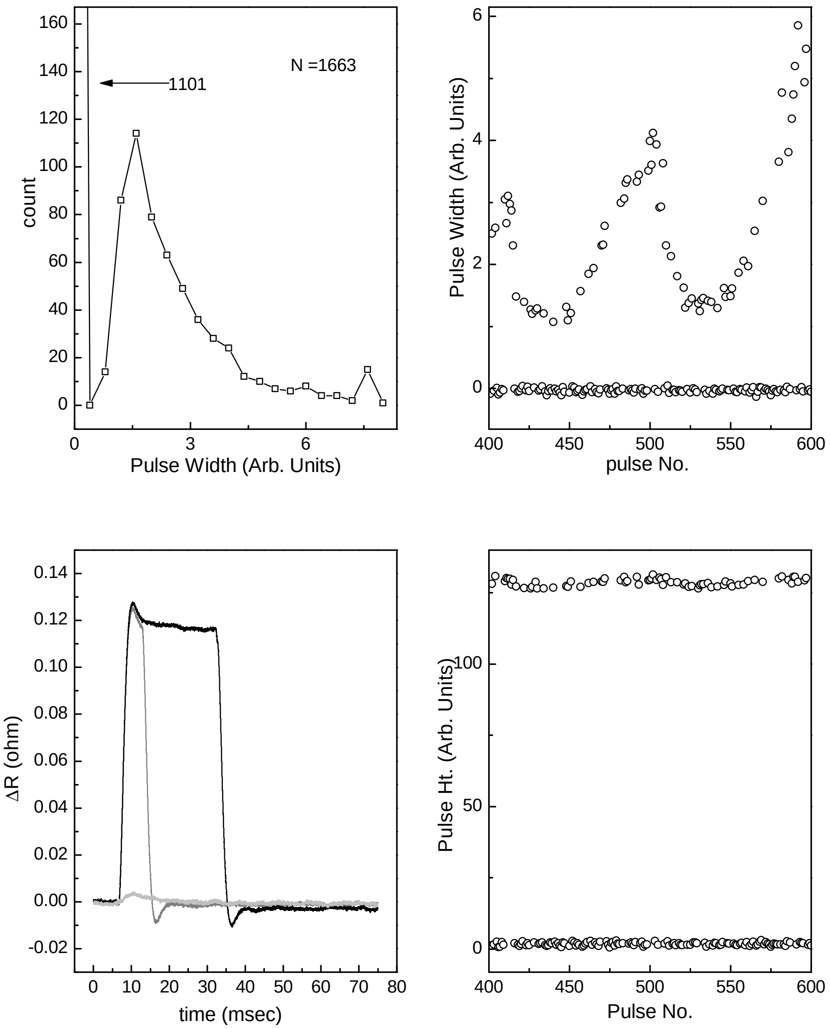

Figure 5.2: Data from tests of the first revision aluminum detectors. The lower left graph shows sample resistance measurements. The pulse height of detection events is roughly constant, as shown in the lower right graph. The width of a detection events (shown in the upper right) varies widely, probably related to temperature fluctuations in the sample cell. A tabulation of these widths is shown in the upper left. Nondetection events are listed as having 0 width.

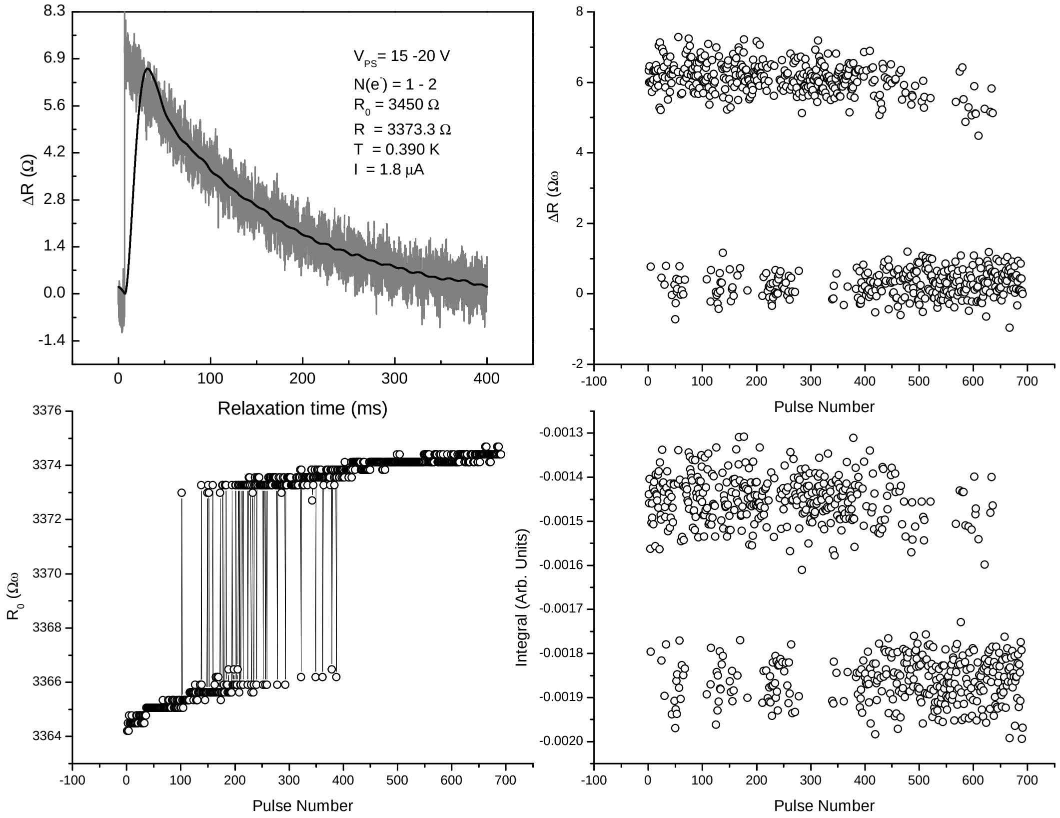

Figure 5.3: Data from tests of second revision titanium detectors. The upper left hand graph shows raw data in grey and running average data in black. The upper-right hand graph shows change in resistance versus pulse number. The lower left hand graph shows the base resistance measurement for each pulse. The lower right hand graph shows the integral of the detector reaction to each pulse as a function of pulse number.

square signal sampled through capacitve coupling. The other oddity observed was the detection of two events where the change in resistance was twice as large as for the other events. The width was not measured for these data points.

5.2.3 Shooting Electrons Through a Small Aperture

There was some concern that the effect we were seeing on our detectors was partially due to large-scale heating due to ballistic impact of electrons over the entire detector wafer. The easy way to insure that only a small number of electrons hit the

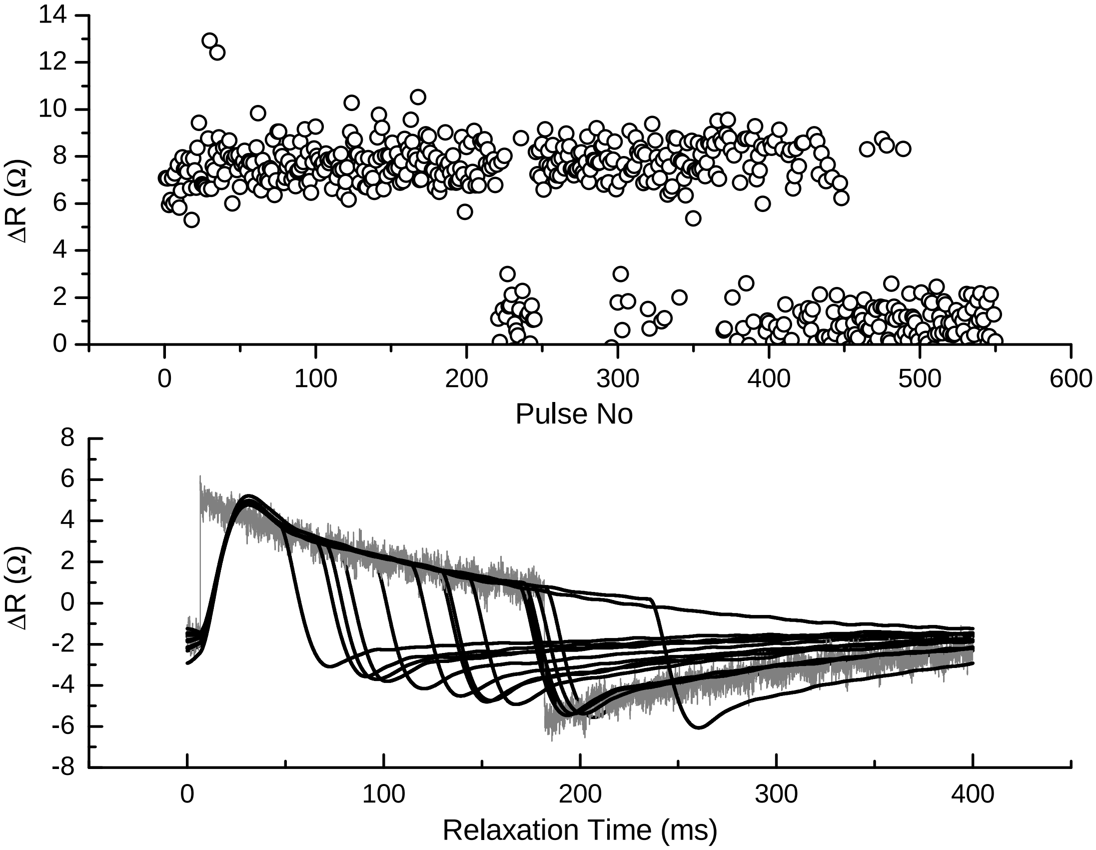

Figure 5.4: Data from additional tests of titanium detectors. The lower graph shows a sample of detection signals. An unfiltered signal is shown in gray, and a series of filtered signals is shown in black. The shape of the curves suggests that these signals last a significantly longer time than the signals shown in Figure 5.3. The upper graph shows the peak resistance change per pulse.

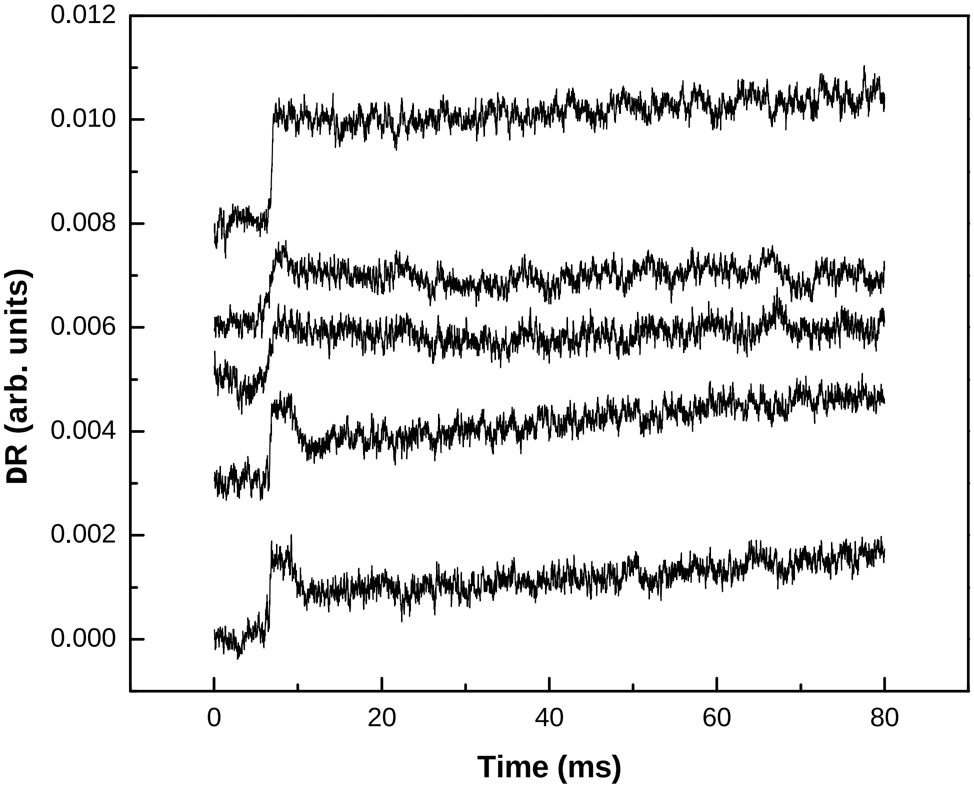

Figure 5.5: Sample electron detections for small incident densities of electrons. The number of electrons hitting the wafer is decreased by introducing a small diameter aperture. Nondetection events are flat lines, and are not shown.

detector wafer, and even then only close to the detector wire, is to mount a small aperture directly between the detector and the PS diode. To that end, an aperture with a diameter of 50 μm was installed between the PS diode and the detector. The amplitude of the signal on the detectors decreased, but was still measurable. Once helium was introduced to the cell, electron detection was completely suppressed. Sample detection events are shown in Figure 5.5.

5.2.4 Discussion

It is difficult to state with any certainty what the incident flux of energy on the detectors was for these experiments; speaking in terms of electron flux is imprecise at best, and our calculations of electron flux depend upon the assumption that the emitted electrons from the PS diode all move perpendicular to the diode for the entire duration of their flight. Looking at Figures 5.3 and 5.4, the data separates roughly into two bands of detection events, one centered around 1-2 Ω, and one at a somewhat higher resistance: $6 \pm 1\,\Omega$ for a diode bias of 15-20 V, and $7.5 \pm 1.5\,\Omega$ for a diode bias of 28 V. Additionally, there were 2 events at $\sim$13 Ω during the 28 V bias tests, which is roughly two times the previously measured events, which could indicate measuring two electron impacts at the same time, rather than one. For these tests, no effect was seen from putting a positive bias on the detector, possibly due to the fact that the large incident flux effectively trapped electrons on their initial trajectories close to the center of the emitter path. Also, the detector sensitivity is an extremely sharp function of temperature: the germanium thermometer on the sample chamber indicated that all of these experiments were preformed at 390 mK. It is clear that some kind of temperature regulation on the detector transition is necessary, but that it will need to be more complicated than a simple PID scheme.

The only concrete result from the aperture experiments is that the presence of a helium film either plugs a 50 μm hole completely, or the PS diode is effectively unusable within our helium environment. PS diode experiments using an electrometer[44] indicate that a much higher voltage is necessary when helium is present in the cell, but that electrons are still emitted. The likely explanation of no detection events after helium was added to the cell is that capillary forces filled the 50 μm hole with helium.

5.3 Electron Mobility Experiments

The easiest experimental way to demonstrate surface state electrons on liquid helium is to perform the mobility experiment first done by W.T. Sommer and D.J.

Tanner,[65] which is diagrammed in Figure 5.6. In essence, we treat the electrons as a 2D conduction channel, and measure the resistance and capacitance as a function of electron density and temperature by measuring the attenuation and phase shift of an applied sine wave using a lock in amplifier. If the geometry is sufficiently simple, then the mobility can be calculated. In our case, we are using this technique as a probe to see if there are electrons on the surface. If we see a significant change in the phase and a decrease in the attenuation of the sample cell, then we have electrons on the surface. Changes in these signals indicate changes in the electron density – larger attenuation indicates a lower density of electrons.

5.3.1 Procedure

The procedure used in both of these experiments is roughly the same: put some liquid in the sample cell, put voltages on the various electrodes to make the electron pool stable on the surface of the helium for a density high enough to measure a change in the cell impedance, try to deposit electrons, and then perform electron ejection tests. Both sample cells had PS diodes installed as a primary electron source and a tungsten filament installed as a backup electron source. In both experiments, we encountered problems with the PS diode, and subsequently used the tungsten filaments in the glow discharge mode.

First, the surface area and volume up to desired liquid level of the sample cell were calculated to provide an estimate for the amount of helium required to fill the cell sufficiently to perform the electron capture. Once this helium was in the cell, we applied a 700-1200 V pulse at a temperature greater than 650 mK to the electron source in an attempt to get a glow discharge to deposit electrons.[1] If the lock-in amplifier did not show any change, then the settings on the ring plate or the pressing field were changed, and the process continued until electrons were either captured or we exhausted the sample space. If the voltage parameter space was exhausted, we added more helium to the system, and then repeated the voltage parameter space

---

[1] Glow discharges require a small pressure of gas to occur. In this system, voltage pulses at a lower temperature either did nothing, or deposited electrons while simultaneously raising the temperature to ∼700 mK.

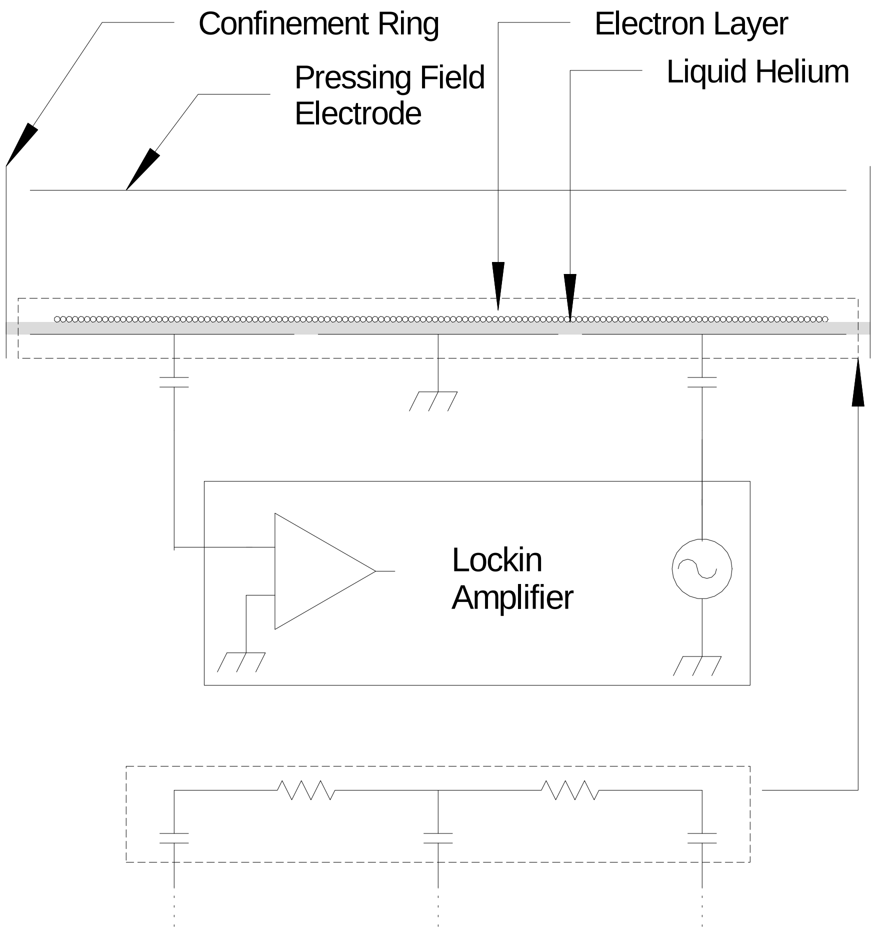

Figure 5.6: Sommer and Tanner mobility measurement for electrons on helium. The signal from a lock-in amplifier is fed into the plate on the right, and the signal is read out through the plate on the left. The middle plate is grounded. An equivalent circuit diagram for the electron layer is presented below the sample sketch.[65]

sweep. Once electrons were captured successfully, the total amount of helium added to the cell was noted, and the minimum voltage for the electron source was determined by turning down the voltage for the source until electron capture was not occurring. In addition, the minimum pressing voltage was determined by turning down the pressing voltage until the electrons escaped.

Once the mobility measurement showed the presence of electrons, we attempted to do electron ejection and detection experiments. First, the pressing field is reduced as much as possible while still maintaining electrons on the film. Then, an appropriate accelerating potential is put on the detector. Finally, a voltage pulse is applied to the appropriate electrode — the ∼1 mm diameter circular electrode in the large scale mobility sample cell, or the post electrodes in the sample cell using the post nanostructure.

5.3.2 Large Scale Mobility Experiments

The first mobility experiment performed used large surface area plates to provide for a more sensitive measurement of electron presence, as we were unsure how sensitive the system would be. In addition, the large helium surface was capable of holding a large number of electrons for performing multiple ejection tests on large(∼10000) electrons per heat-up/cooldown cycle. The number of electrons ejected per pulse is estimated by taking the maximal density of electrons on a helium surface and assuming that all electrons above the electrode are ejected from the surface toward the detector.

Experimental Sample System

The sample system is diagrammed in Figure 5.7. The mobility capacitor plates are 1/2 in by 1/2 in each, and are made by evaporating gold onto a glass slide using a shadow mask made out of 38 AWG copper wire. In addition, a 1 mm hole was drilled through the middle of the mobility capacitor plate underneath the detector. A gold-plated copper post is stycast into this hole before the evaporation is done. This electrode is used to eject electrons from the film toward the detectors. The ring

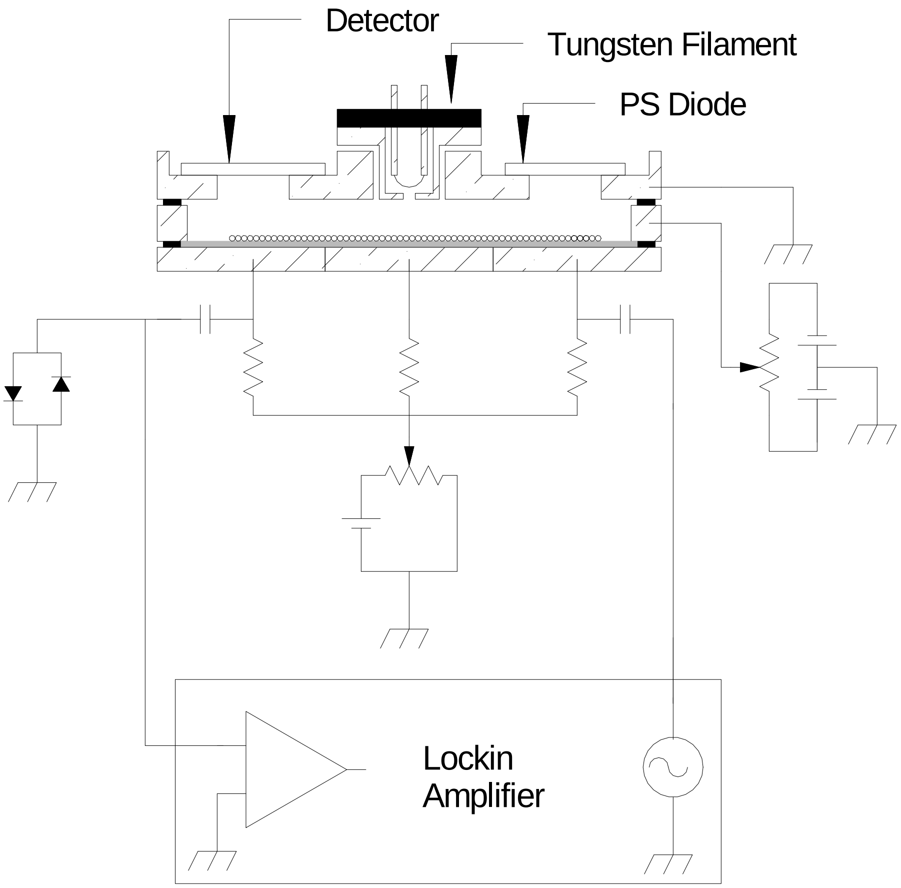

Figure 5.7: Large scale mobility experimental setup.

plate is made out of gold-plated brass, and is separated from the glass slide by four stycast spacers, mounted in the corners of the electrode. and machined parallel to the ring plate. The top plate is made out of gold-plated copper, and is thermally anchored to the sample cell. The top plate is separated from the ring-plate by stycast spacers. The detector used in this experiment is a second revision Ti detector.

Because the top plate requires thermal anchoring, the pressing field must be applied by putting a voltage on the lower electrode, and the voltage applied on the ring plate must also be adjusted appropriately.

The lockin amplifier used for these experiments is an SRS SR830 DSP Lockin Amplifier. The electron ejection signals are generated by an HP 33120A Arbitrary Waveform Generator.

Confining potentials

In the case of the large scale mobility experiment, the ability to capture electrons is weakly dependant upon the applied potentials: so long as the pressing field is not large enough to push electrons into the helium, and the guard ring electrode is sufficiently negative to confine the electron charge in the xy plane, the electrons will stay on the helium surface inside the guard ring.

Once electron capture was achieved, the electrons were stable for long time periods (< 6 hours), and the mobility signal did not decay without perturbation. The electron pool was extremely sensitive to mechanical vibration: tapping the cryostat or even large-scale ground vibrations caused the mobility signal to completely decay. Simply walking around the lab had no effect.

Data

Figure 5.8 shows the lockin signal as a function of applied pulses. The first pulse is the deposition of electrons using the thoriated tungsten filament. The successive pulses are -8 V for 50 ms applied to the circular electrode beneath the detector. Repeated attempts to put electrons on the helium surface using the same parameters yielded similar lockin signals to within the noise of the lockin measurement.

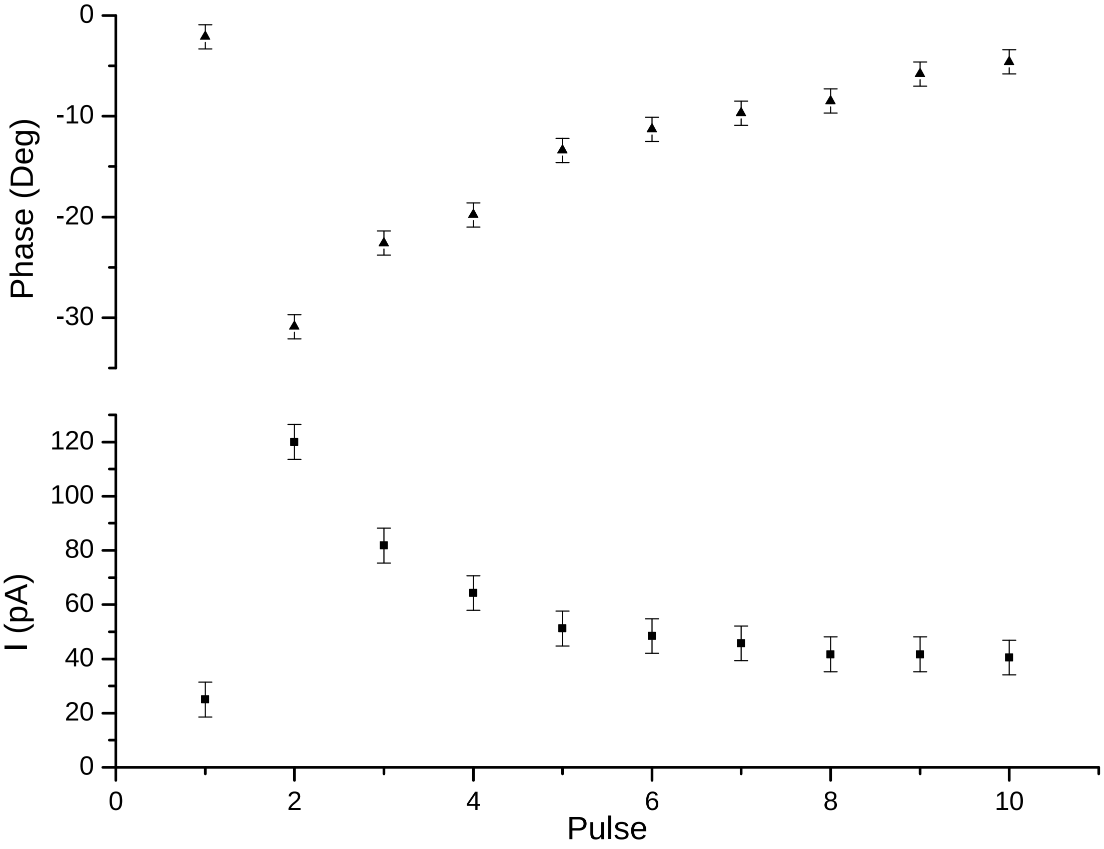

Figure 5.8: Large scale mobility experiment mobility measurement. The attenuation of the sample cell was measured by measuring the AC current passed by a set voltage on the lockin. The first data point shows an empty sample cell. The second data point shows a sample cell after electrons are deposited. Each subsequent point is after the circular ejection electrode is pulsed to -8 V for 50 ms. The decrease in current and phase indicate electrons are leaving the surface.

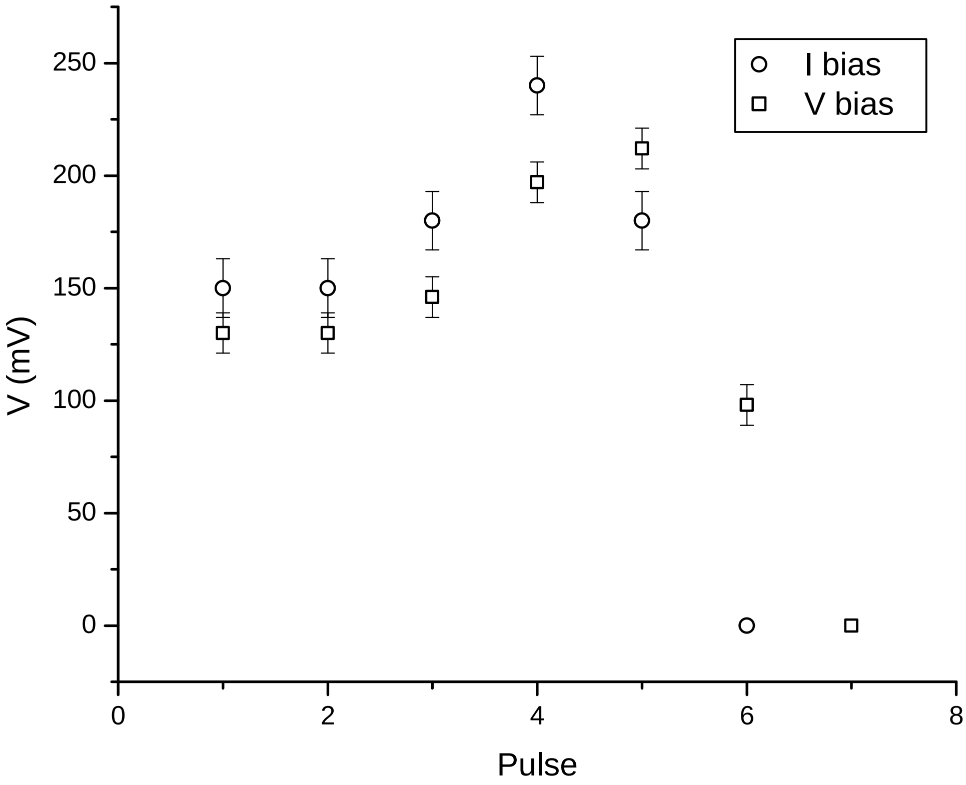

Figure 5.9: Large scale mobility experiment detector data. The open circles are data taken with a 1.0 μA current bias flowing through the detector. The open squares are data taken in the voltage bias mode.

We also tested both the current biasing and the voltage biasing schemes for detector readout. The current bias used for the current biasing experiments was 1.0 μA, and the typical signal lifetime was 85-100 μsec. The voltage used for the voltage biasing scheme was 1.25 V, and the typical signal lifetime was on the order of 5 μs. Both methods showed similar sensitivities, but the overall smaller background signature of the voltage biasing scheme resulted in a slightly larger signal to noise ratio. The measured change of detector state as a function of pulse number is shown in Figure 5.9.

5.3.3 Electron Mobility Experiments using Post Microstructure

Buoyed by our success with the large-scale mobility experiment, we implemented the system again, this time using the post nanostructure chip. The mobility capacitor plates were implemented using the ground plane and the two interdigitated capacitors intended for use as helium level detectors. The expected ejection of electrons using the shorted post structure as the ejection electrode is ∼50. At these densities, the detector voltage bias is more important for attracting electrons toward the detector, as the electron paths will diverge more with smaller incident numbers.

Experimental Sample System

The sample system for this experiment is designed around the post nanostructure, and is diagrammed in Figure 5.10. A massively over-plated post nanostructure chip (mushroom-capped) is mounted on a copper plate using two finger clamps. The post leads are then wire bonded to a set of gold plated copper leads on a circuit board that surrounds the post chip. This copper plate is then screwed into the sample cell. Next, the ring electrode is also screwed into the sample cell. There is a 0.005 in gap between the bottom of the guard ring plate assembly and the posts wafer. The inner diameter of the guard ring is 0.312 in (∼7.92 mm). The next layer is a gold plated brass electrode used both to apply the pressing field and to act as a ground plane for the detector. A layer of mylar tape is used to insulate this electrode from the guard ring assembly. Next is a partially fabricated Ti/Au proximity effect detector with $T_c = 90\,\mathrm{mK}$. This is separated from the brass electrode by a fiberglass spacer .015 in thick. Above that sit the electron sources: a thoriated tungsten filament and a PS diode. Leads are connected to the ground plane and the interdigitated capacitor plates using silver paint.

The lockin amplifier used for these experiments is an SRS SR830 DSP Lockin Amplifier. The electron ejection signals are generated by an HP 33120A Arbitrary Waveform Generator.

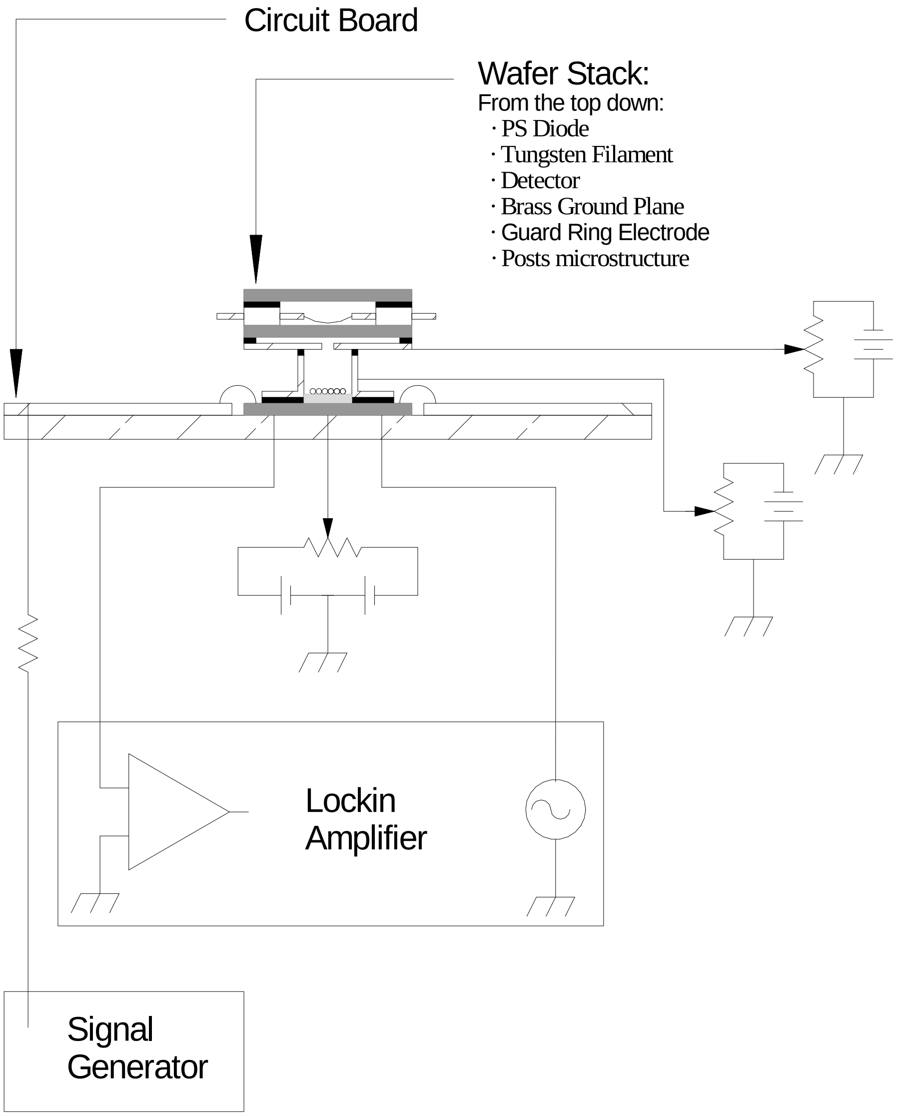

Figure 5.10: Mobility Experiment Using Post Microstructure.

Confinement Potentials

Due to the smaller confinement geometry for this experiment, a vast parameter space of electrode potentials had to be explored: separate voltages for the ring plate and the pressing field had to be tested. For this geometry, the captured pool size and density was more strongly dependant upon the different applied voltages inside the cell.

Data

Sample mobility data is shown in Figure 5.11. The change of phase in this cell is not as dramatic as in the large scale mobility experiment, and is not presented.

Examples of both detection pulses and no detection pulses are given in Figure 5.12. These detection events were observed during the same electron pool for the mobility data presented in Figure 5.11, and were taken using the current biasing electronics. The time series data shows that the detectors current bias (1.0 μA), was large enough to cause the detector to latch, requiring the current bias to be turned off for the detector to return to the superconducting state. The pulse applied to the post electrodes was from +1 V to -3 V for 1 ms. Subsequent experiments were performed with larger pulse voltages applied to the posts, but no signal was ever detected from these experiments. Upon opening our sample cell, we noted that the posts we were pulsing were evaporated in the process of performing this series of experiments. The destruction of the post wafer is shown in Figure 5.13.

There are two main reasons for the partial success of this experiment. First, the sample geometry dictated that any potential put on the detector itself had a minimal impact on the incoming electrons because the detector was too far away from the pressing field electrode for any voltage applied to the detector to influence the potentials inside the sample area, as shown by the computation in Figure 5.14. This in part caused the second problem: in an attempt to increase the signal amplitude at the detector, we applied larger and larger pulses to the posts themselves, causing a large portion of the post chip to evaporate (Figure 5.13).

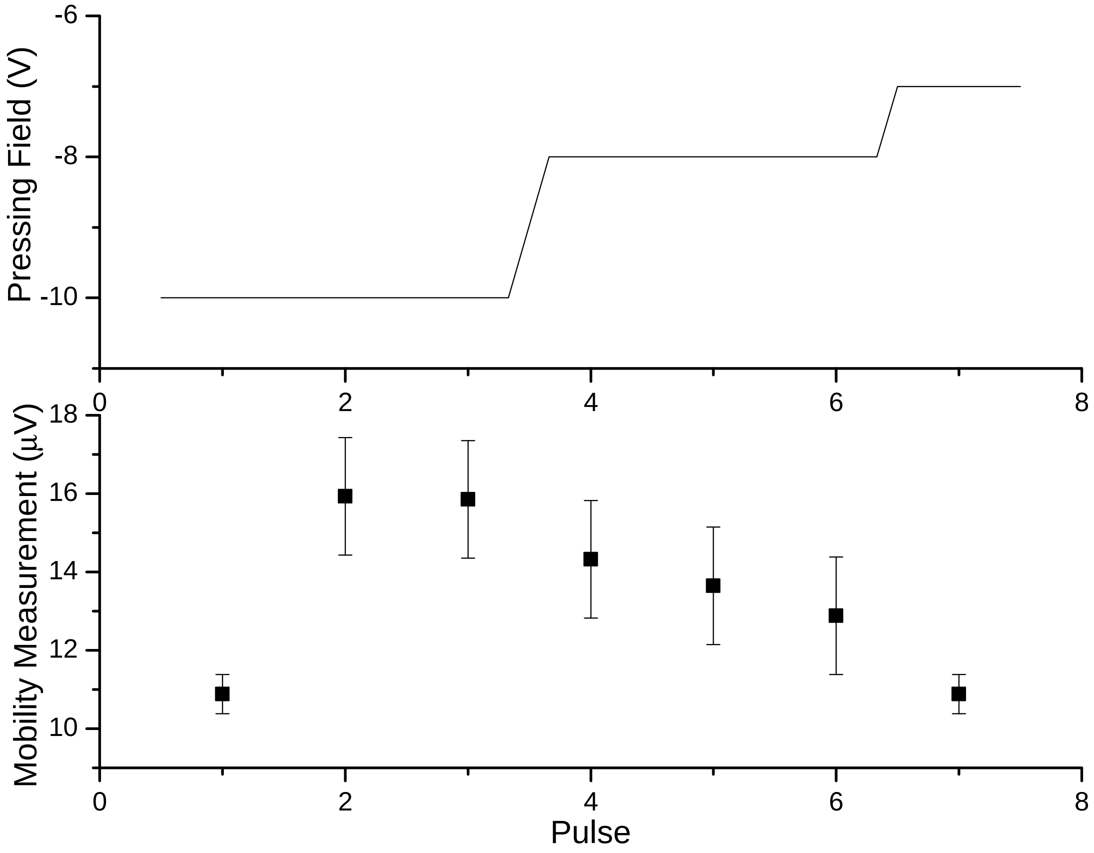

Figure 5.11: Posts mobility experiment mobility measurement. The top graph shows the applied pressing field. The bottom graph shows the mobility measurement as a function of pulse number. Between pulses 3 and 4, the pressing field was turned down to -8 V from -10 V. Subsequent pulses show electrons leaving the surface.

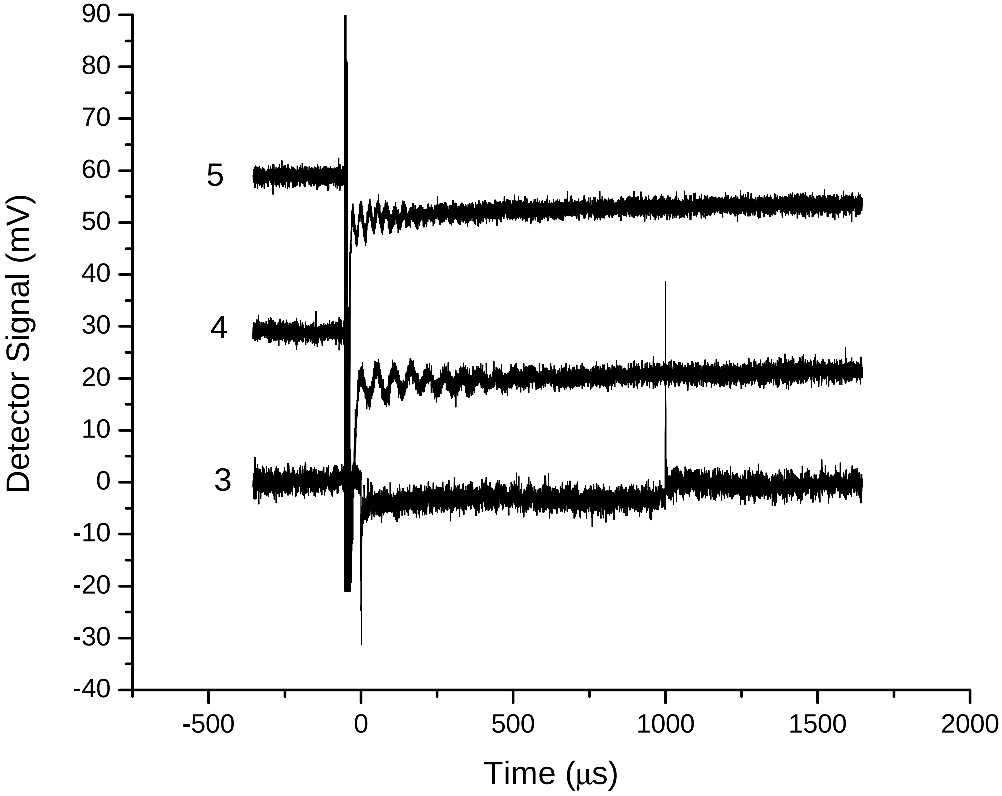

Figure 5.12: Detector signals using the post nanostructure as the ejection electrode. The signals are labeled with their "pulse number", corresponding to the pulses shown in Figure 5.11.

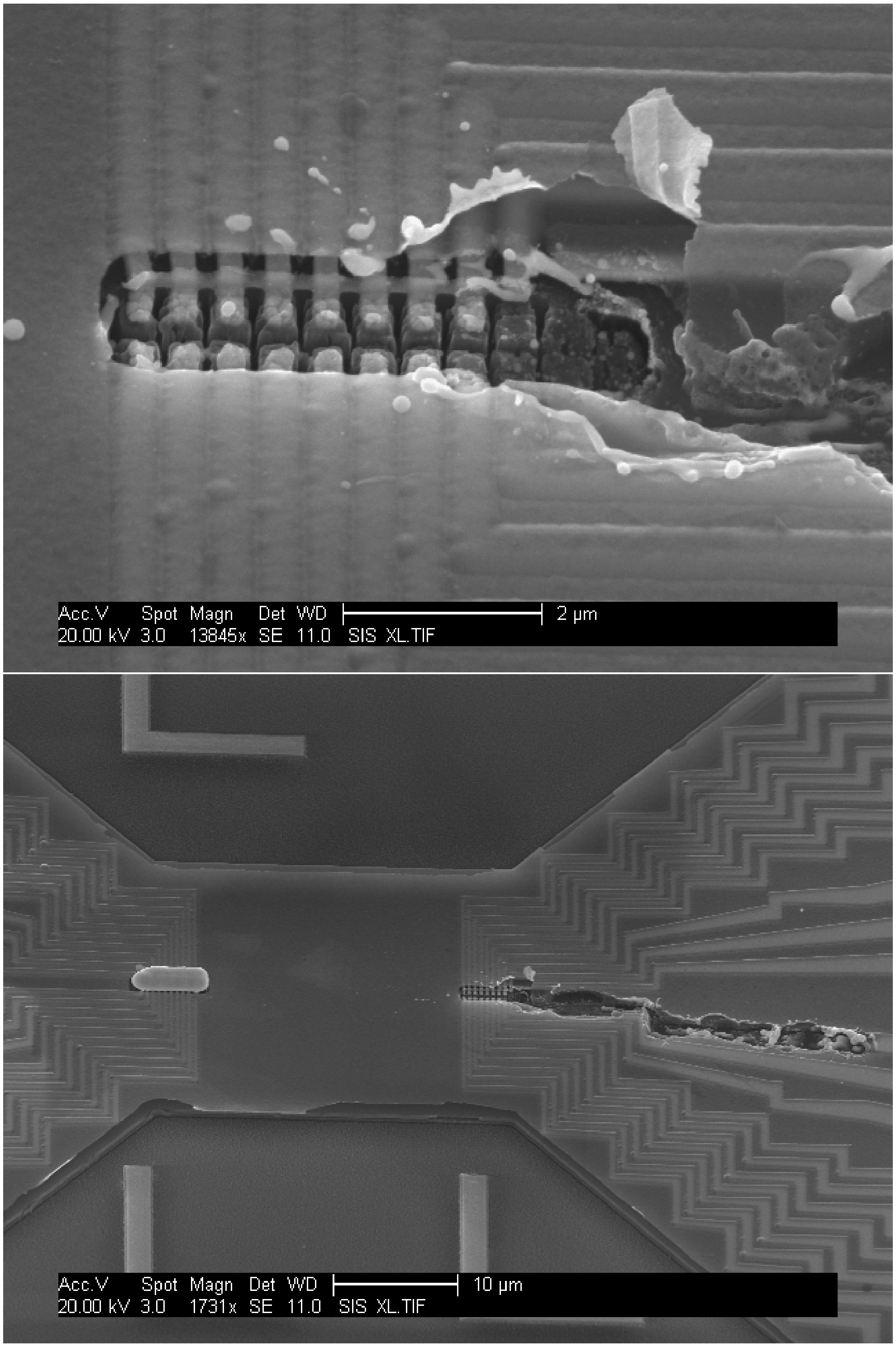

Figure 5.13: Evaporated Post Nanostructure.

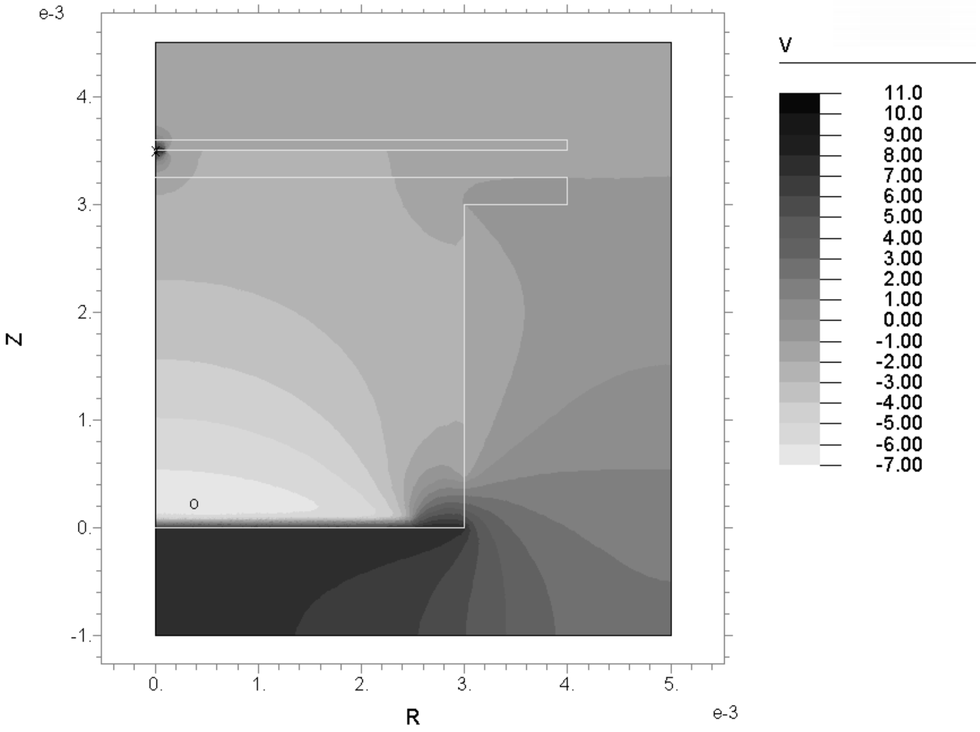

Figure 5.14: Electric Potentials in the sample cell as a function of position, height. Any potential put on the detector is effectively masked by the improvised ground plane used. For this calculation, the detector potential is set at +10 V, the pressing field is set at -2 V, the guard ring is set at -2 V, and the ground plane is set to +8 V. The hole in the pressing field electrode is 2 mm in diameter, and the spacing between the detector and the pressing field electrode is 100 μm. The electron pool is assumed to have a potential of around -7 V. The electric potential is calculated using finite element methods.[52]

5.3.4 Discussion

It is clear from the mobility data that not only were we successful in binding electrons to our liquid helium surfaces, but it was possible to eject small numbers of electrons per pulse on the ejection electrodes, and that once the electron density became too small the electrode pulses tended to push electrons around in the plane rather than ejecting them from the surfaces. Stronger in-plane confinement will be required for single electron capture and release experiments.

From the large-scale mobility experiment, it is clear that voltage biasing our detector is a more effective detection mechanism, and that our detectors are more than capable of sensing $\sim$10000 electron bursts. Unfortunately, the destruction of the post wafer used for this experiment made it difficult to gather sufficient data to state one way or the other if our detection scheme works for $\sim$50 electron bursts. Even if the post wafer survived the experiment, it would still be difficult to tell due to less than ideal electrode geometry.

Chapter 6

Future Experiments

6.1 Introduction

This chapter contains suggested redesigns of the microfabricated elements to allow for more both more diagnostic testing and for further confinement of the electrons in the xy plane.

6.2 Detector Revisions

There are two possible revisions for detection of electrons: redesign and implement the bolometric detectors, or switch to a single electron transistor (SET) based detection scheme.

6.2.1 Bolometric Detector Design Revision

The initial experiments on the detector suffer from a simple lack of knowledge of how much energy is being transfered to our bolometers. We can estimate the incoming electron flux from either a PS diode or off of an electrode, but the total impact energy is not known. In addition, the current bolometer design does not go superconducting at all, probably due to alloying problems in the thick Ti/Au layers.

In order to test detector responsiveness, we propose depositing Cr/Au microwires to be used as heaters $5\,\mu$m away on both sides of the meander pattern detector. These heaters can be used to introduce a controlled amount of heat at a known distance from the detector.

To fix the superconductivity problem, we propose using titanium with no gold capping layer. The immediate native oxide thickness on titanium is 2 nm, growing to 25 nm, over the course of 4 years.[17] In addition, using either negative photomasks or developing a resist bilayer process for depositing the detector meander pattern will allow for a thicker layer of superconductor to be used without fear of shorting. There is a distinct possibility that depositing PECVD $\mathrm{SiN_x}$ will introduce a $\mathrm{TiN_x}$ layer onto the detector as well, but this should be etched off in the subsequent RIE steps.

We also propose changing the overall geometry of the chip: the ground plane is rather large, and since the expected failure rate either due to crystal defects in the wafer or due to pinhole defects in the $\mathrm{SiN_x}$ is proportional to the die area, shrinking the die size will decrease the rate of failure. In addition, a smaller die size will allow more detectors to be fabricated per wafer. By increasing the number of dies per wafer and decreasing the failure rate per die, we should increase the device yield from its current level of ∼25% (about 4-5 devices per wafer).

Ultrasonic griding of the through-hole also presents a small problem: the initial impact of the grinding tip on the wafer leaves a jagged hole. These holes can be drilled by laser machining, either before or after the detectors are fabricated.

A sketch of this design can be seen in Figure 6.1.

6.2.2 Single Electron Transistors

Another possible direction to move with electron detection is to fabricate an SET under a post on the ground plane and use it to detect the presence of electrons by using post electrodes like a conveyor belt to move electrons over to the SET. This is the scheme being used by Lea's group at Royal Holloway.[43] The large problem with SETs is that they are prone to telegraph noise,[30] which requires the devices to be warmed up substantially and subsequently re-cooled once it sets in. Despite all of that, SETs have been fabricated and demonstrated to work,[43] and are a possible direction for electron detection to take in these experiments. The methods used by

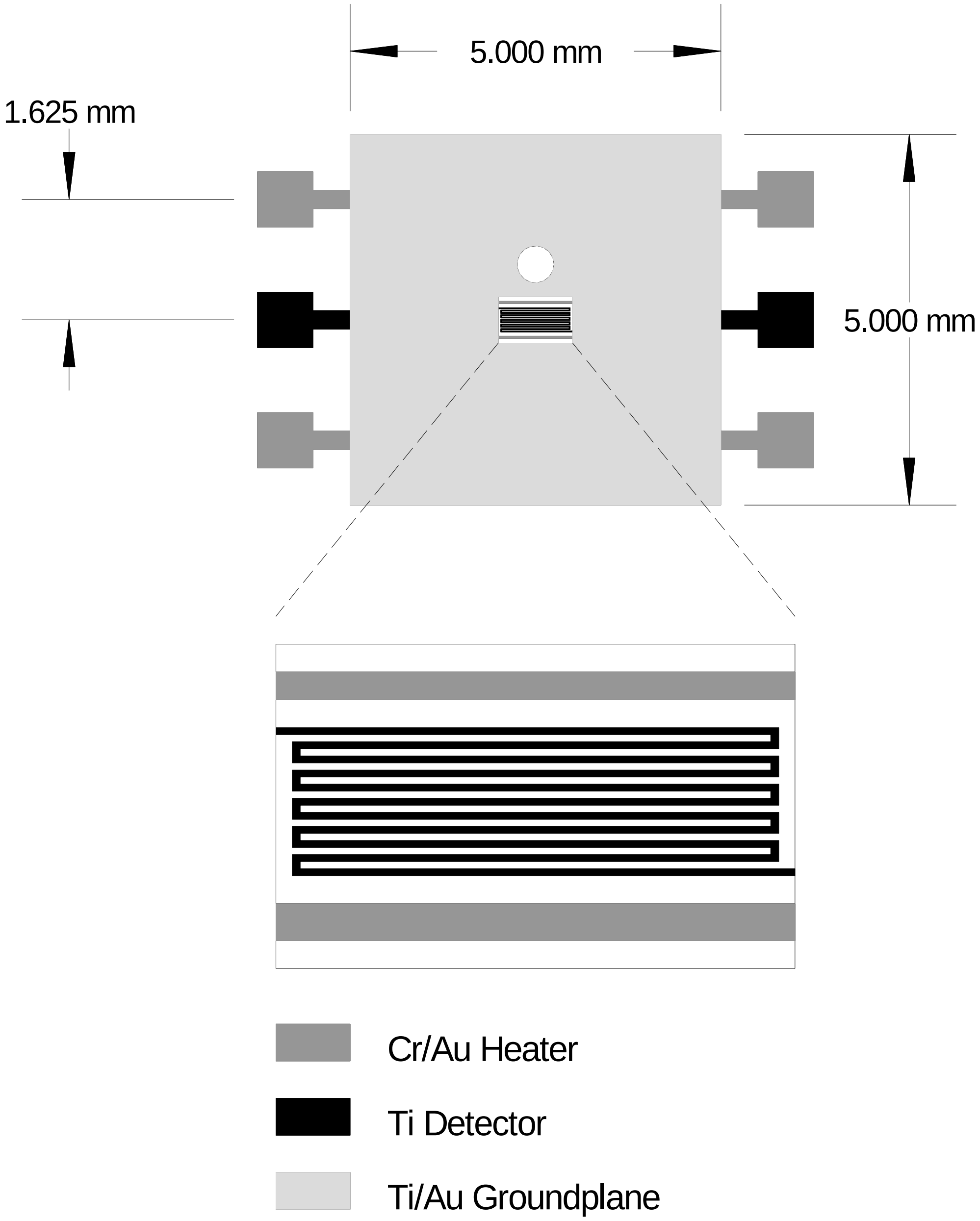

Figure 6.1: Proposed redesign of the bolometric detectors. The bolometer wire is made out of titanium. There are two heater wires 5 μm away from the bolometer made out of Cr/Au. The ground plane is separated from the lower electrodes by a layer of $\mathrm{SiN_x}$. The ground plane is made out of Ti/Au.

Lea's group are also applicable to our geometry, and the sensitivity could even be increased by fabricating a gold post on top of the gate.

6.3 Electrode Revisions

We propose a two-step electrode revision process, starting with the helium pool geometry for initial single qubit testing, following up with a new post geometry once single qubit operations are well understood.

6.3.1 Helium pool geometry with electron mobility experiment

One of the problems with the helium pool wafer as currently designed is there is no independent test available to see if there are electrons on the helium surface; it must be taken as a matter of faith. We propose introducing a mobility-type experiment onto the chip. This will also allow extra electrons to be stored over the mobility plates while experiments are performed in the helium pool. This arrangement also requires three layers of electrodes to manufacture as opposed to the current two layers. Figure 6.2 shows the proposed helium pool design.

6.3.2 Face-Centered Post Array

From calculations of the in-plane confinement potentials, it is clear that the simple post geometry does not provide enough in-plane confinement for actual computational purposes: the harmonic oscillator states are too closely spaced and the range of motion for those levels would quickly result in neighboring post wave functions overlapping, allowing the electrons to behave much as if they were in a conduction band. We propose using a face-centered post array to overcome this problem, as illustrated in Figure 6.3. This would allow us to tune the in-plane Hamiltonian independently of the perpendicular Hamiltonian, allowing us to choose the shape of the harmonic oscillator potential, and even prevent the overlap of the wave functions of electrons bound to the posts. Sample calculations for the in-plane confining electric

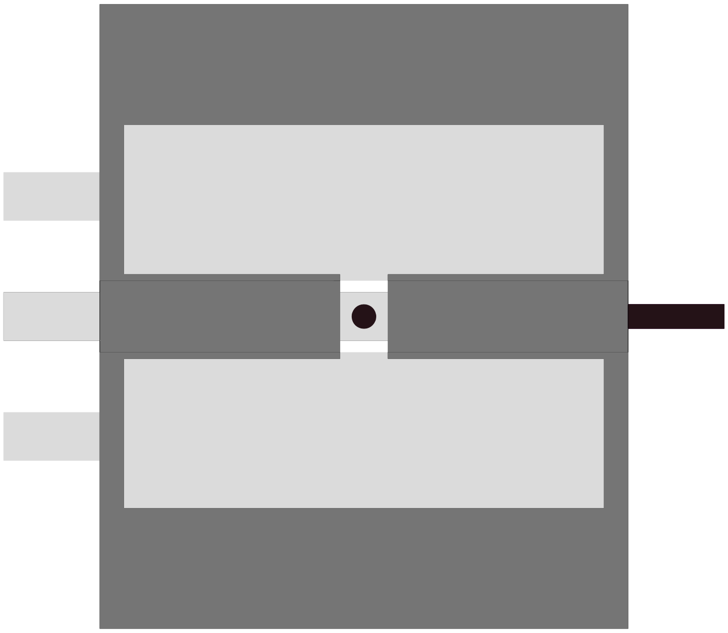

Figure 6.2: Helium Pool Electrode with Mobility Experiment. The electrode used for electron ejection is shown in black. The mobility plates are shown in light gray. The ground plane is shown in dark gray. A layer of insulation is required between each layer of electrodes. This sketch shows the basic idea, and is not to scale.

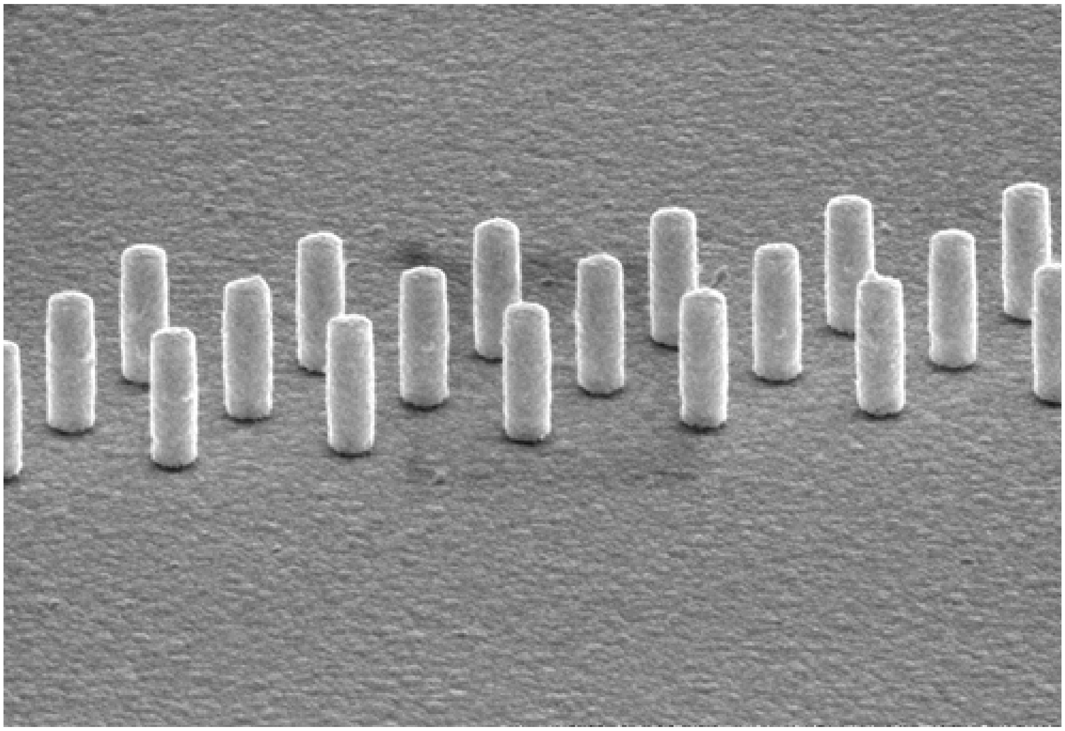

Figure 6.3: Face-Centered Post Array. These posts were fabricated by performing the post fabrication process on a gold-coated wafer. The fabrication parameters are the same as those for the rectangular array of posts. The distance between the posts on the corners of the face-centered array is 1 μm. The inter-qubit spacing for this arrangement is 1 μm as well, resulting in a SWAP frequency that is lower by a factor of 8 than for posts at 500 nm separation.

field are shown in Figure 6.4. In addition, a mobility experiment can be built onto the wafer in much the same way as shown for the helium pool geometry, except that instead of the central array housing the simple helium pool geometry, it would house a face-centered array of posts.

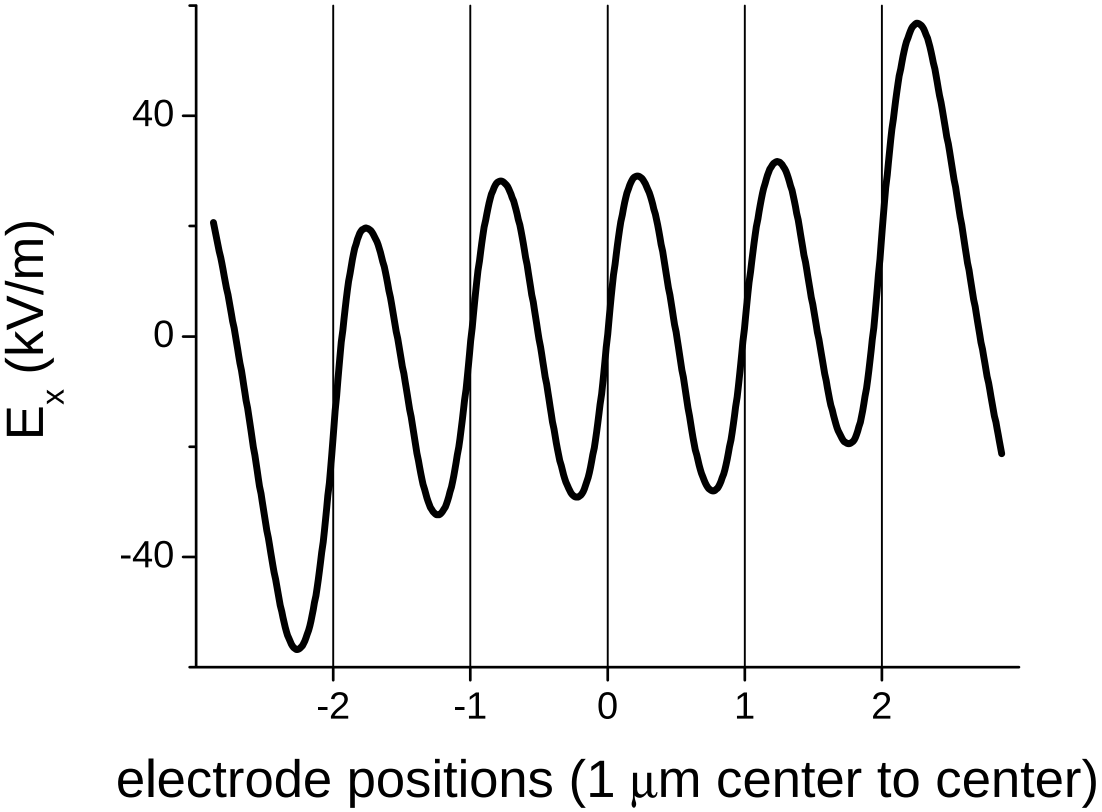

Figure 6.4: Horizontal Electric Field for Face-Centered Post Structure. For this computation, the center posts are set to 6.0 mV, and the corner posts are set to -15.0 mV. For this set of field parameters, $\omega_{\parallel}/2\pi \simeq 30\,\text{GHz}$.

Appendix A

Wave Functions for H_z^0

The full Schrödinger equation for (1.3) can be written as:

$$-\frac{\hbar^2}{2m_e}\partial_z^2\Psi_n^{(0)} - \frac{\Lambda}{4\pi\epsilon_0}\frac{1}{z}\Psi_n^{(0)} = E_n^{(0)}\Psi_n^{(0)} \tag{A.1}$$

We can simplify this by defining the Bohr radius by equation (1.7), and ε_n as

$$\varepsilon_n = \frac{2m_e E_n^{(0)}}{\hbar^2} \tag{A.2}$$

Under this transformation, our equation becomes

$$\partial_z^2\Psi_n^{(0)} + \frac{2}{a_0}\frac{1}{z}\Psi_n^{(0)} = \varepsilon_n\Psi_n^{(0)} \tag{A.3}$$

Let us notice that for this potential, the wave functions need to equal zero at both $z = 0$ and $z = \infty$. This is easily accomplished by using a model function that is the product of a polynomial and an exponential: $\Psi_n^{(0)} = \phi_n(z)e^{-z/\eta_n}$. Plugging this equation into (A.3), we get this differential equation for ϕ_n:

$$\partial_z^2\phi_n - \frac{2}{\eta_n}\partial_z\phi_n + \frac{2}{a_0}\frac{1}{z}\phi_n + \left(\frac{1}{\eta_n^2} + \varepsilon_n\right)\phi_n = 0 \tag{A.4}$$

We can represent ϕ_n as a generalized polynomial, $\phi_n(z) = \sum_{i=1}^{n} A_i^{(n)} z^i$, and plugging this into (A.4), we get:

$$i(i+1)A_{i+1}^{(n)}z^{i-1} - \frac{2}{\eta_n}iA_i^{(n)}z^{i-1} + \frac{2}{a_0}A_i^{(n)}z^{i-1} + \left(\frac{1}{\eta_n^2} + \varepsilon_n\right)A_i^{(n)}z^i = 0 \tag{A.5}$$

Since this relation needs to be true for all exponents of z, we can simplify this relation by noting that

$$\varepsilon_n = -\frac{1}{\eta_n^2}$$

Given that, we get a recursion relation for the $A_i^{(n)}$s:

$$A_{i+1}^{(n)} = -\frac{2}{i(i+1)}\left(\frac{1}{a_0} - \frac{i}{\eta_n}\right)A_i^{(n)}$$

Also note that $A_{n+1}^{(n)} = 0$, which forces $\eta_n = na_0$, and changes our recursion relation to:

$$A_{i+1}^{(n)} = \frac{-2}{i(i+1)}\frac{n-i}{na_0}A_i^{(n)} \tag{A.6}$$

Given this recursive relation for the $A_i^{(n)}$s, we can find an equation for them, with only $A_1^{(n)}$ left as a normalization factor:

$$A_i^{(n)} = \left(\frac{-2}{a_0}\right)^{(i-1)}\binom{n}{i}\frac{1}{n^i(i-1)!}A_1^{(n)} \tag{A.7}$$

The normalization condition for ψ_n is $\langle n \mid n\rangle = 1$. Or, expanded out,

$$1 = A_1^{(n)^2}\sum_{i,j=1}^{n}\left(\frac{-1}{n}\right)^{i+j}\left(\frac{2}{a_0}\right)^{i+j-2}\binom{n}{i}\binom{n}{j}\frac{\int_0^\infty dz\; z^{i+j}e^{-2z/a_0}}{(i-1)!(j-1)!} \tag{A.8}$$

which can be simplified to

$$\left(\frac{1}{A_1^{(n)}}\right)^2 = \frac{na_0^3}{8}\sum_{i,j=0}^{n} ij\,(-1)^{i+j}\binom{n}{i}\binom{n}{j}(i,j)!, \tag{A.9}$$

where $(i,j)!$ is a multinomial coefficient. Let us consider only the partial sums over i:

$$\Sigma_j = j\binom{n}{j}(-1)^j\sum_{i=0}^{n} i(-1)^i\binom{n}{i}(i,j)! \tag{A.10}$$

We can rewrite the multinomial coefficients as a product like so:

$$(i,j)! = \prod_{k=1}^{j}\frac{i+k}{k} = \frac{1}{j!}\prod_{k=1}^{j}(i+k),$$

and note that the multinomial coefficients are a polynomial in i of order j. To see the effects of this order on the sum, let us consider the effect of only the highest order term in a polynomial on the sum, like so:

$$\begin{aligned}
& \sum_{i=0}^{n} i^{j+1}(-1)^i \binom{n}{i} \\
= \quad & \sum_{i=0}^{n} i^{j+1}(-1)^i \frac{n}{i} \binom{n-1}{i-1} \\
= \quad & -n \sum_{i=0}^{n-1} (i+1)^j (-1)^i \binom{n-1}{i}
\end{aligned}$$

Again, consider only the highest order term for now:

$$\begin{aligned}
= \quad & -n \sum_{i=0}^{n-1} i^j (-1)^i \binom{n-1}{i} \\
= \quad & -n(n-1) \sum_{i=0}^{n-2} i^{j-1} (-1)^i \binom{n-2}{i}
\end{aligned}$$

Here, we can see a pattern which will eventually leave us with an alternating sum over binomial coefficients if $j+1 < n$, and such an alternating sum is 0. So $\Sigma_j = 0$ for $j < n-1$, and we only need to consider terms in our polynomial expansions that will have an order of n at the very least. Taking only the sum from Σ_{n-1}, and keeping only the leading order term, we find

$$\begin{aligned}
& \sum_{i=0}^{n} i^n (-1)^i \binom{n}{i} \\
= \quad & -n \sum_{i=0}^{n-1} i^{n-1} (-1)^i \binom{n-1}{i} \\
= \quad & n(n-1) \sum_{i=1}^{n-2} i^{n-2} (-1)^i \binom{n-2}{i} \\
\vdots \quad & \vdots \\
= \quad & (-1)^n n!.
\end{aligned}$$

For Σ_n, we need to keep the two leading order terms from each sum:

$$\begin{aligned}
&\sum_{i=0}^{n}(-1)^i\left(i^{n+1}+\frac{n(n+1)}{2}i^n\right)\binom{n}{i} \\
=&\quad (-1)^n\frac{n(n+1)!}{2}-n\sum_{i=0}^{n-1}(-1)^i\left(i^n+ni^{n-1}\right)\binom{n-1}{i} \\
\vdots&\quad \vdots \\
=&\quad (-1)^n\frac{n(n+1)!}{2}+(-1)^n n!\sum_{i=0}^{n} n-i \\
=&\quad (-1)^n n(n+1)!.
\end{aligned}$$

The two interesting partial sums can then be written as

$$\Sigma_{n-1} = -n^2(n-1) \tag{A.11}$$

$$\Sigma_n = n^2(n+1) \tag{A.12}$$

The sum in equation (A.9) then reduces to

$$\sum_{j=0}^{n}\Sigma_j=\Sigma_{n-1}+\Sigma_n=2n^2, \tag{A.13}$$

and we can thus simplify equation (A.9) to

$$A_1^{(n)}=2(na_0)^{-3/2},$$

and we can write our generalized wave functions as:

$$|\Psi_n^{(0)}\rangle=\frac{2}{n\sqrt{na_0}}e^{-z/na_0}\sum_{i=1}^{n}\left[\frac{(-2)^{i-1}}{n^i(i-1)!}\binom{n}{i}\left(\frac{z}{a_0}\right)^i\right] \tag{A.14}$$

Appendix B

Microfabrication Procedures

B.1 Wafer Cleaning for 100 mm wafer

1. Place wafer in an ultrasonic bath in acetone for two minutes.
2. Rinse wafer using isopropanol (IPA).
3. Place wafer in an ultrasonic bath in IPA for two minutes.
4. Rinse wafer using deionized (DI) water.
5. Place wafer in an ultrasonic bath in DI water for two minutes.
6. Rinse wafer using DI water.
7. Blow the remaining water off the surface using dry N_2 gas.
8. Bake on a hot plate set at 150 °C for 5 minutes.

B.2 Wafer Cleaning for processed dies

1. Place die in an ultrasonic bath in acetone for two minutes.
2. Rinse die using isopropanol.
3. Place die in an ultrasonic bath in IPA for two minutes.

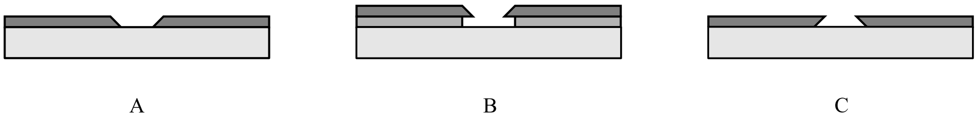

Figure B.1: Typical photoresist profiles. A. Positive photo resist. B. Bilayer photo resist. C. Negative photoresist. Profiles are exaggerated. Typical deviations from right angles are $5° - 10°$.

4. Rinse die using IPA.

5. Blow the remaining IPA off the surface using either canned air or dry N_2 gas.

B.3 Photoresist processes

There are a lot of different types of photoresist for a lot of different purposes. The primary distinction between photoresist is if they are positive, where the part exposed to ultraviolet (UV) light is developed by the developer, or if they are negative, where the part not exposed to the UV is developed. For applications where an insulating layer needs to cover the metalization, then either a negative resist or a bilayer resist should be used. Positive resists are faster and easier to develop, but the wall profiles can be problematic, as they can lead to having metal fringes left behind after developing.

For sputtering applications, bilayer photoresists lead to the cleanest liftoff, but require the most processing. For e-beam or thermal evaporators, a negative resist is the easiest way to prevent the metal fringing problem, although, it can also be controlled using thin positive resists and thin metalization layers. The different resist profiles can be seen in figure B.1.

Table B.1: Sample photolithography processes.

Parameter	Positive Resist	Bilayer Resist	Negative Resist
PMGI	None	SF 11	None
Spin Speed	—	4 krpm	—
Spin Time	—	60 sec	—
Bake Temperature	—	180 °C	—
Bake Time	—	300 sec	—
Imaging Resist	S 1805	S 1805	AZ 5214e
Spin Speed	5 krpm	5 krpm	3 krpm
Bake Temperature	102 °C	102 °C	110 °C
Bake Time	60 sec	60 sec	60 sec
Exposure Time	6 sec	6 sec	10 sec
Crosslink Bake Temperature	—	—	118 °C
Crosslink Bake Time	—	—	60 sec
Flood Exposure	NO	NO	YES
Developer	321	321	AZ 400k
Concentration (with water)	1:1	1:1	1:2
Development Time	30 sec	120 sec	60 sec

B.3.1 Standard positive photoresist layer

A typical example is given in table B.1.

1. Spin on HMDS, as an adhesion layer, at 4k RPM for 60 seconds. Let stand for 30 seconds.

2. Spin on the chosen photoresist. Relevant parameters are the spin speed (which determines the thickness), and spin time (which determines the uniformity of the layer).

3. Bake the wafer appropriately for the chosen photoresist. Relevant parameters are the bake temperature and time, which both determine the amount of solvent left in the layer. This affects both the exposure time and the development time.

4. Expose using either a contact mask aligner or stepper depending on tools available. For the work done at UCSB, a stepper was used for all photolithography. At UCSD, contact mask aligners were used for all photolithography. Relevant parameter is the exposure time.

5. Develop using the developer appropriate for the photoresist used. Relevant parameters are type of developer used, developer concentration and development time.

6. Use a plasma etcher with an O_2 descum process to remove the HMDS adhesion layer.

B.3.2 Standard bilayer positive photoresist layer

A typical example is given in table B.1.

1. Spin on PMGI. Relevant parameters are spin time and speed, and specific type of PMGI. Again the spin speed and specific resist determine the thickness of this layer. Also, note that PMGI will leave fingers unless steps are taken to keep them from forming: i.e., a swab soaked with acetone is held at the edge of the wafer during spinning.

2. Bake on a hot plate. Relevant parameters are bake time and temperature. These two parameters determine the rate of resist undercut of the bilayer.

3. Spin on and bake the imaging resist as described above in the Standard Positive Photoresist section.

4. Expose using either a contact mask aligner or stepper depending upon tools available. Relevant parameter is exposure time.

5. Develop using the developer appropriate for the imaging resist used. Most photoresist developers are bases (low Ph), and will also develop the PMGI. A hotter PMGI bake will require longer to develop, and will undercut less.

B.3.3 Standard negative photoresist layer

A typical example is given in table B.1.

1. Spin on HMDS as an adhesion layer, at 4k RPM for 60 seconds. Let stand for 30 seconds.

2. Spin on resist. Again, spin speed and time are relevant parameters.
3. Bake on a hot plate. Relevant parameters are bake time and temperature.
4. Expose using either a contact mask aligner or a stepper depending upon tools available. Relevant parameter is exposure time.
5. Re-bake the wafer at a higher temperature. This re-bake will cross-link the polymer in the exposed areas, making them insensitive to further UV exposure. Relevant parameters are bake temperature and time.
6. Flood expose the wafer to UV for a long time (~ 2 min.)
7. Develop in the appropriate developer. Developer concentration and development time are the relevant parameters.
8. Use a plasma etcher descum process to remove the HMDS.

B.3.4 Liftoff

For most photoresists, lifting off the photoresist after metalization is accomplished by placing the wafer into an ultrasonic bath in acetone. There is a resist-specific solvent for PMGI called PG Remover; however, acetone still works (it is just a lot slower). Liftoff time is influenced by the thickness of the metalization layer, and the bake temperature of the resist.

B.4 Electron Beam Lithography

In many ways, ebeam lithography is similar to photolithography, except the resist is exposed by an ebeam writer rather than a mask aligner, the pattern is formed by directing the ebeam path rather than a photomask, and the developers used are organic rather than basic.

---

[1] The dosage for the PMMA is very misleading given the apparent resist thickness. The resist thickness reported is the thickness across the entire wafer. At the point where the lithography is being done, the PMMA is thicker, as there is a void in a thick layer of $\mathrm{SiN_x}$ there. See **X**.

Table B.2: Typical e-beam resist processes. The listed dosage is only a starting point; it will vary due to pattern density, etc.

Parameter	ZEP 520A	950 PMMA A7
Spin Speed	4 krpm	2.0 krpm
Spin Time	120 s	120 s
Resist Thickness	0.35 μm	0.8 μm
Pre-bake Temperature	180 °C	180 °C
Pre-bake Time	300 s	90 s
Exposure Energy	30 keV	50 keV
Dosage (typical)	35 μC/cm^2	1200 μC/cm^2 [1]
Post-bake Temperature	120 °C	100 °C
Post-bake Time	120 s	90 s
Developer	MIBK	1:3::MIBK::IPA
Develope Time	60 s	300 s

B.4.1 Typcial resist process

Two separate recipies are given in table (B.2); the first is a typical recipe for ZEP 520A, and the second is the recipe used for the post microstructure in PMMA. In both cases, a 120 ålayer of gold is thermally evaporated onto the resist before e-beam writing is done, to insure there is no charge buildup in the polymer. This gold must be removed via a gold etch solution before developing is done.

1. Spin on resist. Spin speed and time are the relevant parameters.

2. Pre-bake on a hot plate. Relevant parameters are bake time and temperature.

3. (Optional) Deposit a thin (10 nm) layer of Au to help prevent surface charging. Direct application of the e-beam will still punch through the surface, and image the resist beneath.

4. Expose the resist using an e-beam writer. The relevant parameters are the geometry to be exposed, and the dosage required due to that geometry. A lot of experimentation is needed to get the dosage correct, as it depends on many factors, including pattern density, sharpness of angles to be exposed, etc.

5. Post-bake the wafer. This sharpens the edges of the developed pattern.

6. Develop the resist in an appropriate developer. Small features require a more dilute developer and longer times.

B.4.2 Liftoff

Liftoff is typically done using acetone in an ultrasonic bath. In the case of the post microstructure, we were afraid the power of the ultrasonic bath would break off the posts; the resist was removed in this case by soaking in acetone, typically for more than 12 hours. This was followed with a soak in IPA and

B.5 RIE

For plasma etchers using reactive ion etching (RIE), the recipie used will inevitably be complicated for most tasks – different gasses are added for different reasons. In general, Cl-containing gasses are used to etch metals, Fl-containing gasses are used to etch dielectrics. Oxygen is often added to most plasma recipes to mediate the process. Oxygen is also used on its own for descum recipes – i.e. to remove small ammounts of photoresist from developed patterns.

The relevant parameters for these recipes is the flow rate for each component gas, the total pressure of the plasma, the applied RF power, and the time the recipe runs for. Some plasma etchers also have an ICP power supply. We did not use this capability when it was present. Also, note that recipes depend heavily upon the particular plasma etcher and the chamber condition. It goes without saying that the recipe needs to be fine-tuned for each application.

B.5.1 Typical descum process

An oxygen descum process is typically used to remove the HDMS from the surface of a wafer, or any residual photoresist left after development. We are mostly not concerned about etch rates in this recipe, except that we want to insure we don’t etch through the patterned resist. The recipe used at UCSD in the Oxford Plasmalab P100 RIE/ICP Plasma Etcher is given in table B.3.

Table B.3: RIE recipes used in the Oxford Plasmalab P100 RIE/ICP Plasma Etcher

recipe	Gases (sccm)		Pressure (mT)	Power (W)	Time	Total Etch
	O_2	CF_4				
O_2 descum	50	0	75	200	30 s	n/a
SiN_x	1	40	50	100	12 min	8500 Å

B.5.2 Typical etch for SiN_x

This is a typical recipe for etching SiN_x. By raising the amount of oxygen in the plasma, it etches faster, but also undercuts metal groundplanes more. Etch rate can also be increased by changing both the pressure and the applied power. For these etches, however, a slower etch is desirable – it allows for better control of the final nitride film thickness. The recipe used at UCSD in the Oxford Plasmalab P100 RIE/ICP Plasma Etcher is given in table B.3.

B.6 PECVD

Plasma enhanced chemical vapor deposition (PECVD) is one of the standard methods for depositing dielectric layers. A reactive combination of gasses is heated in the reactor along with the sample for deposition. In this process, the stoichiometric balance of the gases is important, as is the temperature of the reaction. In addition, the applied RF power generates a plasma, which enhances the reaction rate and increases the growth rate of the dielectric on the substrate.

At UCSD, the PECVD used is an Oxford Instruments Plasmalab PECVD. This particular PECVD is equipped with both a high frequency (HF) and a low frequency (LF) power supply. By alternating between the two supplies, the strain of the grown film can be controlled.

For PECVD recipies, the relevent parameters are the flow rate of each constituent gas, the total reactor pressure, the reactor temperature, the applied RF power, and the time of the reaction. At UCSD, the parameters also include the applied LF power, and the ratio of the RF / LF pulse sequences.

B.6.1 SiO_2

When depositing standard SiN_x, it is necessary to first deposit a thin layer of SiO_2 as an intermediate layer to help deal with the high strain exerted by stoichiometric SiN_x deposited directly on Si. A sample recipe is presented in Table B.4.

B.6.2 Standard SiN_x

Stoiciometric silicon nitride has the chemical formula Si_3N_4, but is difficult to grow on a silicon substrate because the large difference in the lattice constants yields an extremely high strain film that will buckle and deform. As a result, the film grown is usually an amorphous SiN_x, where the ammount of silicon in the film is increased. Unfortunately, if this silicon content is increased too much, the film becomes semiconducting, and at room temperatuer ceases to be an effective insulator as a thin film. The high strain film also leads to a large number of pinholes, and makes the film subject to strain-related fracture defects at sharp edges in lithography. As a result, if one wants to use SiN_x as an insulator, one needs to first deposit a seed layer directly on the silicon before putting down a metal layer.

The recipe for SiN_x listed in Table B.4 is intended for use after a layer of SiO_2 has been deposited as an adhesion layer, and offers a highly strained film on a silicon substrate.

B.6.3 Strain Free SiN_x

There are a variety of methods for depositing a strain free SiN_x layer on a silicon substrate.[51] The method used by the Oxford Instruments Plasmalab PECVD is a modulated RF technique. A high frequency (HF) power supply is used for a specefied period, followed by a low frequency (LF) supply. The net effect is an increase in silicon inclusions, and a less strained film. A ratio of times of 13s : 7s :: HF : LF is sufficient to grow an essentially strain free SiN_x.

Table B.4: PECVD Recipes. HF/LF recipe is for the Oxford Instruments Plasmalab PECVD at UCSD.

Parameter	SiN_x	Strain Free SiN_x	SiO_x
Gases			
5%:95%::SiH_4:N_2	400 sccm	400 sccm	170 sccm
N_2	600 sccm	600 sccm	—
NH_3	20 sccm	20 sccm	—
N_2O	—	—	710 sccm
Pressure	650 mTorr	650 mTorr	1000 mTorr
RF Power(13.56 MHz) (HF)	20 W	20 W	20 W
RF Power (225 kHz) (LF)	—	20 W	—
Time HF::LF	—	13 s :: 7 s	—
Temperature	320 °C	320 °C	320 °C
Deposition Rate	>10 nm/min	>10 nm/min	>50 nm/min

B.7 Electroplating

The electroplating was undertaken at UCSD using a lab built electroplating setup, consisting mainly of a power supply and a stirring hotplate. The electroplating bath used was a gold sulfate solution. Electroplating was done at 67 °C, with a current of 25 mA concurrently on both a die and a witness piece. The time for plating was the control variable. At 2 minutes, 30 seconds, mushrooms were visible, indicating overplating. At 2 minutes, no such mushrooms were evident.

B.8 Dicing

Dicing was performed at UCSD in the Physics Department Sample Prep room using a DoAll saw with a hydraulic table drive and a lab-made vacuum chuck leveled on the table. The blades used were 0.001 in. diamond blades made by Dynatek. This process was performed dry, which, while hard on the blade, protects the wafer from a flowing particulated slurry.

Toward the end of this work, a Disco 3220 Automatic Dicing Saw became available. All subsequent dicing was done using this saw. This saw uses a water-based coolant, so a protective layer of photoresist was put on all wafers that went through this process.

B.9 Drilling holes by ultrasonic grinding

Ultrasonic grinding was performed at UCSD using a Raytheon ultrasonic impact grinder with a custom made grinding tip. A slurry of DI water and Norbide abrasive is necessary for this process.

1. Install and balance the ultrasonic grinding tip.
2. Set the applied vertical force of the tip to 4 oz.
3. Glue the die to a glass slide using crystalbond.
4. Clamp the glass wafer to the XY stage installed in the ultrasonic grinder.
5. Using the XY stage, align the ultrasonic grinding tip to the desired hole location.
6. Lower the tip to find the location of contact. Back off 0.050 in.
7. Turn on the ultrasonic grinder. Allow to warm up for 5 minutes.
8. Slowly turn up the power to approximately 50% .
9. Adjust the tuning of the ultrasonic grinder. Use the tuning eye if it is working; however, adequate tuning can be accomplished by touch. The grinder must be tuned to near resonance.
10. Apply the slurry.
11. Grind the hole to the desired depth.
12. Back out the tip. Rinse the die using DI water.
13. Reheat the glass slide to remove the die.
14. Disolve the remaining crystalbond by soaking in acetone for a few hours.
15. Clean the die by ultrasound in the standard fashion.

Bibliography

[1] D.V. Averin. Quantum Computing and Quantum Measurement with Mesoscopic Josephson Junctions. *Fortchritte der Physik*, 9-11:1055, 2000.

[2] C.H. Bennett. Logical Reversibility of Computation. *IBM Journal of Research and Development*, 17:525, 1973.

[3] N.E. Booth and D.J. Goldie. Superconducting Particle Detectors. *Supercounducting Science and Technology*, 9:493, 1996.

[4] L. Brillouin. *Science and Information Theory.* Dover, second edition, 2004.

[5] G. Burkard, H.-A. Engel, and D. Loss. Spintronics and Quantum Dots for Quantum Computing and Quantum Communication. *Fortchritte der Physik*, 9-11:965, 2000.

[6] G. Chardin. Dark Matter Direct Detection. In C. Enss, editor, *Cryogenic Particle Detection.* Springer, 2005.

[7] A.M. Childs, I.L. Chuang, and D.W. Leung. Realization of Quantum Process Tomography in NMR. *Physical Review A*, 64:012314, 2001.

[8] A. Church. A Note on the Entscheidungsproblem. *Journal of Symbolic Logic*, 1:40–41, 1936.

[9] A. Church. An Unsolvable Problem of Elementary Number Theory. *American Journal of Mathematics*, 58:345–363, 1936.

[10] D. Coppersmith. An Approximate Fourier Transform Useful in Quantum Factoring. *IBM Research Report RC 19642*, 1994.

[11] D. Deutsche. Quantum theory, the Church-Turing Principle and the Universal Quantum Computer. *Proceedings of the Royal Society of London A*, 400(97), 1985.

[12] D. Deutsche and R. Jozsa. Rapid Solution of Problems by Quantum Computation. *Proceedings of the Royal Society of London A*, 439:553, 1992.

[13] D.P. DiVincenzo. Two-Bit Gates are Universal for Quantum Computing. *Physical Review A*, 51:1015, 1995.

[14] D.P. DiVincenzo. The Physical Implementation of Quantum Computation. *Fortschritte der Physik*, 48:771, 2000.

[15] M.I. Dykman, P.M. Platzman, and P. Seddigrad. Qubits with Electrons on Helium. *Physical Review B*, 63:155402, 2003.

[16] M.I. Dykman, L.F. Santos, M. Shapiro, and F.M. Izrailev. Many-Particle Localization by Constructed Disorder and Quantum Computing. In *NUCLEI AND MESOSCOPIC PHYSICS: Workshop on Nuclei and Mesoscopic Physics: WNMP 2004*, volume 777, page 148. AIP, 2005.

[17] J. Emsley. *Nature's building blocks: an a-z guide to the elements*. Oxford University Press, 2001.

[18] R.P. Feynman. Simulating Physics with Computers. *International Journal of Theoretical Physics*, 21:467, 1982.

[19] D. Fredkin. Lecture notes for quantum optics. (unpublished), 2003.

[20] E. Fredkin and T. Toffoli. Conservative Logic. *International Journal of Theoretical Physics*, 21:219, 1982.

[21] P. Glasson, V. Dotsenko, P. Fozooni, M.J. Lea, W. Bailey, G. Papagreorgiou, S.E. Andresen, and A. Kristensen. Observation of Dynamical Ordering in a Confined Wigner Crystal. *Physical Review Letters*, 87:176802, 2001.

[22] L.K. Grover. Quantum Mechanics Helps in Searching for a Needle in a Haystack. *Physical Review Letters*, 79:326, 1997.

[23] S. Guide, M. Riebe, G.P.T. Lancaster, C. Becher, J. Eschner, H. Haeffner, F. Schmidt-Kaler, I.L. Chuang, and R. Blatt. Implementation of the Deutsch-Jozsa Algorithm on an Ion-Trap Quantum Computer. *Nature*, 421:48, 2003.

[24] D. Hilbert. Mathematische Probleme. *Göttinger Nachrichter*, page 253, 1900.

[25] J.T. Gill III. Computational Complexity of Probabilistic Turing Machines. In *Proceedings of the sixth annual ACM symposium on Theory of computing*, page 91. ACM, 1974.

[26] A. Imamogluc. Quantum Computation Using Quantum Dot Spins and Microcavities. *Fortchritte der Physik*, 9-11:987, 2000.

[27] J.D. Jackson. *Classical Electrodynamics*. Wiley, third edition, 1999.

[28] J. Justesen and T. Hoholdt. *A Course in Error-Correcting Codes.* European Mathematical Society, 2004.

[29] B.E. Kane. Silicon-Based Quantum Computation. *Fortchritte der Physik*, 9-11:1023, 2000.

[30] M.J. Kelly. *Low-Dimensional Semiconductors: Materials, Physics, Technology, Devices.* Oxford University Press, 1995.

[31] D.G. Coryand R. Laflamme, E. Knill, L. Viola, T.F. Havel, N. Bouland, G. Boutis, E. Fortunato, S. Lloyd, R. Martinez, C. Negrevergne, M. Pravia, Y. Sharf, G. Teklemariam, Y.S. Weinstein, and W.H. Zurek. NMR Based Quantum Information Processing: Achievenemnts and Prospects. *Fortchritte der Physik*, 9-11:875, 2000.

[32] R. Landauer. Irreversibility and Heat Generation in the Computing Process. *IBM Journal*, 5:183, 1961.

[33] A.T. Lee, P.L. Richards, S.W. Nam, B. Cabrera, and K.D. Irwin. A Superconducting Bolometer with Strong Electrothermal Feedback. *Applied Physics Letters*, 69:1801, 1996.

[34] D. Leibfried, B. DeMarco, V. Meyer, D. Lucas, M. Barrett, J. Britton, W.M. Itano, B. Jelenkovic, C. Langer, T. Rosenband, and D.J. Wineland. Experimental Demonstration of a Robust, High-Fidelity Geometric Two Ion-Qubit Phase Gate. *Nature*, 422:412, 2003.

[35] M. Li and P. Vitanyi. Theory of Thermodynamics of Computation. In *PhysComp '92., Workshop on Physics and Computation*, page 42. IEEE, 1992.

[36] S.-K. Lin. Diversity and entropy. *Entropy*, 1:1, 1999.

[37] A.E. Lita, D. Rosenberg, S. Nam, A.J. Miller, D. Balzar, L.M. Kaatz, and R.E. Schwall. Tuning of Tungsten Thin Film Superconducting Transition Temperature for Fabrication of Photon Number Resolving Detectors. *IEEE Transactions on Applied Superconductivity*, 15:3528, 2005.

[38] Y. Makhlin, G. Schon, and A. Shnirman. Josephson-Junction Qubits. *Fortchritte der Physik*, 9-11:1043, 2000.

[39] Y.P. Monarkha and V.B. Shikin. Low-Dimensional Electronics Systems on a Liquid Helium Surface. *Soviet Journal of Low Temperature Physics*, 8:279, 1982.

[40] M.A. Nielsen. Universal Quantum Computation Using Only Projective Measurement, Quantum Memory, and Preperation of the $|0\rangle$ State. quant-ph/0108020, 2001.

[41] M.A. Nielsen and I.L. Chuang. *Quantum Computation and Quantum Information.* Cambridge, 2000.

[42] D.K.L. Oi, S.J. Devitt, and L.C.L. Hollenberg. Scalable Error Correction in Distributed Ion Trap Computers. *Physical Review A*, 74:052313, 2006.

[43] G. Papageorgiou, P. Glasson, K. Harrabi, V. Antonov, E. Colin, P. Fozooni, P.G. Frayne, M.J. Lea, D.G. Rees, and Y. Mukharsky. Counting Individual Trapped Electrons on Liquid Helium. *Applied Physics Letters*, 86:153106, 2005.

[44] S. Pilla, B. Naberhuis, and J. Goodkind. A Porous Silicon Diode as a Source of Low-Energy Free Electrons at milli-Kelvin Temperatures. *Journal of Applied Physics*, 98:024508, 2005.

[45] S. Pilla, X.C. Zhang, B. Naberhuis, A. Syschenko, and J.M. Goodkind. High Aspect Ratio Microcolumns to Manipulate Single Electrons on a Liquid Helium Surface for Quantum Logic Bits. *IEEE Transactions on Nanotechnology*, 5:568, 2006.

[46] M. Plank. On the Law of Distrinbution of Energy in the Normal Spectra. *Annalen der Physik*, 4:553, 1901.

[47] P.M. Platzman and M.I. Dykman. Quantum Computing with Electrons Floating on Liquid Helium. *Science*, 284:1967, 1999.

[48] P.F. Poyatos, J.I. Cirac, and P. Zoller. Schemes of Quantum Computations with Trapped Ions. *Fortchritte der Physik*, 9-11:785, 2000.

[49] R. Raussendorf and H.J. Briegel. Quantum Computing via Measurements Only. quant-ph/0010033, 2002.

[50] L.E. Reichl. *A Modern Cource in Statistical Physics.* Wiley, second edition, 1998.

[51] F.L. Riley. Silicon Nitride and Related Materials. *Journal of the American Ceramic Society*, 83:245, 2000.

[52] M.N.O. Sadiku. *Numerical Methods in Electromagnetics.* CRC Press, third edition, 2001.

[53] M. Saitoh. Warm Electrons on the Liquid ^{4}He Surface. *Journal of the Physical Society of Japan*, 42:201, 1977.

[54] G.F. Saville. *Electron Tunneling from Bound States on the Surface of Liquid Helium.* PhD thesis, University of California, San Diego, 1993.

[55] N. Sawides and B. Window. Electrical Transport, Optical Properties, and Structure of TiN Films Synthesized by Low-Energy Ion Assisted Deposition. *Journal of Applied Physics*, 64:225, 1988.

[56] C.E. Shannon. A Symbolic Analysis of Relay and Switching Circuits. Master's thesis, Massachusets Institute of Technology, 1937.

[57] C.E. Shannon. A Mathematical Theory of Communication. *The Bell System Technical Journal*, 27:379, 1948.

[58] C.E. Shannon. A Mathematical Theory of Communication (Concluded). *The Bell System Technical Journl*, 27:623, 1948.

[59] C.A. Shiffman, J.F. Cochran, M. Garber, and G.W. Pearsall. Specific Heat Measurements and Proximity Effects in Tin-Lead Eutectic Alloys. *Reviews of Modern Physics*, 36:127, 1964.

[60] V.B. Shikin and Yu.P. Monarkha. On the Interaction of Surface Electrons in Liquid Helium with Oscillations of the Vapor-Liquid Interface. *Journal of Low Temperature Physics*, 16:193, 1974.

[61] K. Shirahama, S. Ito, H. Suto, and K. Kono. Surface Study of Liquid ^{3}He Using Surface State Electrons. *Journal of Low Temperature Physics*, 101:439, 1995.

[62] P.W. Shor. Algorithms for Quantum Computation: Discrete Logarithms and Factoring. In *Proceedings, 35th Annual Symposium on Foundations of Computer Science*. IEEE, 1994.

[63] P.W. Shor. Polynomial-Time Algorithms for Prime Factorization and Discrete Logariths on a Quantum Computer. *SIAM Journal of Computation*, 26:1997, 1997.

[64] M. Sipser. The History and Status of the P versus NP Question. In *Proceedings of the twenty-fourth annual ACM symposium on Theory of computing*. ACM, 1992.

[65] W.T. Sommer and D.J. Tanner. Mobility of Electrons on the Surface of Liquid ^{4}He. *Physical Review Letters*, 27:1345, 1971.

[66] T.P. Spiller. Superconducting Circuits for Quantum Computing. *Fortchritte der Physik*, 9-11:1075, 2000.

[67] T. Toffoli. Bicontinuous Extensions of Invertible Combinatorial Functions. *Mathematical Systems Theory*, 14:13, 1981.

[68] A.M. Turing. On Computable Numbers, with an Application to the Entscheidungsproblem. *Proceedings of the London Mathematical Society*, 42:230–265, 1936.

[69] L.M.K. Vandersypen, M. Steffen, G. Breyta, C.S. Yannoni, M.H. Sherwood, and I.L. Chuang. Experimental Realization of Shor's Quantum Factoring Algorithm Using Nuclear Magnetic Resonance. *Nature*, 414:883, 2001.

[70] A. Vergis, K. Steiglitz, and B. Dickinson. The Complexity of Analog Computation. *Mathematics & Computation in Simulation*, 28:91, 1986.

[71] J. von Neumann. First Draft of a Report on the EDVAC. Technical report, Moore School of Electrical Engineering, University of Pennsylvania, 1945.

[72] D.J. Wineland, D. Leibfried, M.D. Barrett, A. Ben-Kish, J.C. Bergquist, R.B. Blakestad, J.J. Bollinger, J. Britton, J. Chiaverini, B. Demarco, D. Hume, W.M. Itano, M. Jensen, J.D. Jost, E. Knill, J. Koelemeij, C. Langer, W. Oskay, R. Ozeri, R. Reichle, T. Rosenband, T. Schaetz, P.O. Schmidt, and S. Seidelin. Quantum Control, Quantum Information Processing and Quantum-Limited Metrology with Trapped Ions. quant-ph/0508025, 2005.